GALACTIC SATELLITE GALAXIES

QUAN GUO

GALACTIC SATELLITE GALAXIES

Quan Guo

A Thesis presented for the degree of
Doctor of Philosophy

Insitute for Computational Cosmology
Department of Physics
University of Durham
England

Feb and 2013

Galactic Satellite Galaxies

Quan Guo

Submitted for the degree of Doctor of Philosophy

Feb 2013

Abstract

In this thesis, we investigate the luminosity functions (LFs) and projected number density profiles of galactic satellites around isolated primaries of differing luminosity.

To this end, we develop a new method to select isolated galactic satellite systems using the Sloan Digital Sky Survey (SDSS) spectroscopic and photometric galaxy samples. For specific luminosity primaries, we are able to stack as many as $\sim 50,000$ galaxy systems to obtain robust statisitcal results. Based on these samples, we derive accurate satellite luminosity functions extending almost 8 magnitudes fainter than their primaries and accurate projected number densities profiles of satellites down to 4 magnitudes fainter than their primaries. Then, we determine how the satellite luminosity functions and projected number density profiles vary with both the properties of their satellites and their primaries. In addition, we find that the normalized profiles can be well fitted by the NFW profiles in most cases. The dependence of the NFW concentration parameters on the luminosity of the satellites and their primaries are explored. Inspired by the similar independent study, we also explore the dependence of estimates of satellite luminosity functions on two different background subtraction methods.

We then measure these quantities for model satellites placed into the Millennium and Millennium II dark matter simulations by the GALFORM semi-analytic galaxy formation model for different bins of primary galaxy magnitude. We compare our model predictions to the data that we previously measured. The generally successful comparison of the GALFORM model with the SDSS data performed here provides a non-trivial validation of the assumptions and framework of this kind of modelling.

GALACTIC SATELLITE GALAXIES

Quan Guo

A Thesis presented for the degree of
Doctor of Philosophy

Insitute for Computational Cosmology
Department of Physics
University of Durham
England

Feb and 2013

CONTENTS

LIST OF FIGURES

LIST OF TABLES

DECLARATION

The work described in this thesis was undertaken between 2009 and 2013 while the author was a research student under the supervision of Dr. Vincent Eke, Professor Shaun Cole and Professor Carlos Frenk at the Institute for Computational Cosmology, the Department of Physics, Durham University, England. No part of this thesis has been submitted elsewhere for any other degree or qualification and it is all my own work unless referenced to the contrary in the text.

Chapter 2 of this thesis has been published in the form of a paper,

- Guo Q., Cole S., Eke V., Frenk C., *"The satellite luminosity functions of galaxies in Sloan Digital Sky Survey"*, 2011, MNRAS, 417, 370

Chapter 3 of this thesis has been published in the form of a paper,

- Guo Q., Cole S., Eke V., Frenk C., *"The satellite projected number density profiles galaxies in Sloan Digital Sky Survey"*, 2012, MNRAS, 427, 428

Chapter 5 has been submitted for publication in the form of a paper,

- Guo Q., Cole S., Eke V., Frenk C., Helly J., *"Spatial and luminosity distributions of galactic satellites"*, submitted to MNRAS, Manuscript ID: MN-12-3187-MJ

ACKNOWLEDGEMENTS

This thesis is dedicated firstly to my supervisors, Vincent Eke, Shaun Cole, and Carlos Frenk, without whose help, support and continuous patience answering my endless stream of my questions, none of this would have been possible. I should also like to thank them for their consistent help with improving my English writing skills. I would also like to give my thanks to John Helly who spend a lot of efforts preparing the GALFORM catalogues for me. Without his help, Chapter 5 of this thesis could not have been completed.

There is not enough space and time to record how I enjoyed PhD life in Durham, a small and beautiful town. The people in ICC are so kind. And I'm so lucky that I stayed in one of the best office rooms during my PhD life. The people who shared the office room are so nice. The printer is so close to my desk which instantly made my life easier. The work on this thesis has been supported by a fellowship from the European Com- missions Framework Programme 7, through the Marie Curie Initial Training Network CosmoComp (PITN-GA- 2009-238356). And many thanks go to Carlton Baugh who leads the project.

Finally, I will think my family, their supports are always the source of my strength.

Dedicated to

My family

1 INTRODUCTION

In my hometown, the porters who work at the university are philosophers because they ask every person passing through the campus gate three questions which are always the same "Who are you", "Where are you from" and "Where will you go". These questions are also the ultimate questions about the universe that astronomers have been trying to answer for thousands of years and now, amazingly, can be quantitatively answered by combining our knowledge of fundamental physics with our understanding of the early universe. Moreover, the models which are used to describe our answers can be tested against observations.

With the help of Einstein's general relativity theory, we for the first time are able to produce a compelling and testable model of the universe. The success of the current standard cosmological model is supported by the three important observational facts:

- the expansion of the universe;
- the abundances of light elements, which are consistent with the predictions of the model;
- the cosmic microwave background.

This model has been tested and shown to be in good agreement with observations of large scale structure. This thesis focuses on observations of the universe at galactic scales and testing the model at these scales.

The structure of this chapter is as follows. In Section 1.1, we present a short overview of the current standard cosmological model. In Section 1.2, we briefly introduce the semi-analytical galaxy formation models within the framework of standard cosmological models and galactic satellite galaxies. Galactic satellite galaxies in this thesis are defined as the satellite galaxies around isolated galactic primariy galaxies. In Section 1.3, we review the current state of studies of galactic satellite galaxies. Finally, Section 1.4, provides a summary of the topics and results presented in the thesis. In this chapter, we use units in which

$$\hbar = c = k_B = 1. \tag{1.0.1}$$

1.1 The Standard Cosmological Model

The universe consists of space-time and energy (or matter). A proper theory about the universe should, in principle, be able to track the evolution of space and energy with time. With a few assumptions, the modern cosmological models built on general relativity is now able to fulfill the above basic requirement for cosmological models.

1.1.1 Dynamics of the model universe

The current standard cosmological model is based on the following three assumptions:

- *At large scales, the universe is homogeneous and isotropic*. Because of symmetry, the **Robertson-Walker metric**, which has 4 degrees of freedom, is enough to characterize the geometry of the space-time. The motivation of this assumption is originally from the "Copernican principle" which suggests that human beings do not occupy a special place in the Universe. However, the physical explanation for this assumption can be provided by the theory of inflation (Guth, 1981; Linde, 1982; Albrecht & Steinhardt, 1982), which suggests the universe may have gone though a stage of exponential expansion at early times. The rapid expansion can result in the

homogeneity at large scales of the current universe.

- The expansion of the universe is governed by the properties of components within it. With assumptions that *the components of the universe are perfect isotropic fluids*, We can track the evolution of components at large scales.

- *at large scales, the expansion of the universe is determined by all components within the universe, which can be described by the* ***Einstein equation****.*

Based on the above three assumptions, a model (**Friedmann-Robertson-Walker-Lemaître (FRWL) Model** or **FLRW Model**, see Nussbaumer & Bieri, 2011) of our universe can be set up. The dynamics of this model universe can be determined with the so-called **Freidmann-Lemaître** (Freidmann, 1922) equations:

$$\begin{aligned} H(t)^2 &= \frac{8\pi G}{3}\rho_{\text{tot}}(t) - \frac{k}{a(t)^2}; \\ \dot{H}(t) &= -4\pi G\left(\rho_{\text{tot}}(t) + p_{\text{tot}}(t)\right) + \frac{k}{a(t)^2}; \\ \dot{\rho}(t)_{\text{tot}} &+ 3H(\rho_{\text{tot}}(t) + p_{\text{tot}}(t)) = 0. \end{aligned} \tag{1.1.2}$$

Here $H(t) = \dot{a}(t)/a(t)$ is **Hubble parameter**. ρ_{tot} and p_{tot} are the total density and pressure of components within the universe respectively.

Once a cosmological model has been adopted by specifying cosmological parameters, we can define what we mean by "distance".

- **Luminosity Distance**

  We define the distance to an object of intrinsic luminosity L as the quantity D such that the observed flux from the source is $f = L/(4\pi D^2)$. We will use luminosity distance in calculating the intrinsic luminosity of galaxies later.

- **Angular Diameter Distance**

  We can define the angular diameter distance, $\mathcal{D}$, such that a source of intrinsic size d subtends an angle $\delta\theta = tan^{-1}(d/D) \simeq d/\mathcal{D}$ $(\mathcal{D} \ll d)$. The angular diameter distance can be related to the luminosity distance by:

$$\mathcal{D} = (1+z)^{-2} + D. \tag{1.1.3}$$

The angular diameter distance will be used in measuring the satellite systems in following chapters.

1.1.2 Cosmic inventory

Armed with the **FLRW** model describing the expansion of the universe, if we can determine the constituents of the universe and the parameters in Equations 1.1.2, we would be able to choose the model which is the closest to the observed universe. In the current standard cosmological model, there are mainly three components that have different equations of state in the universe. Therefore these three components evolve differently with time.

- **Radiation and Kinetic Energy**

  The energy can be in the form of relativistic particles such as photons and neutrinos. The equation of state for photons is $w = 1/3$, hence the energy density of photons is $\rho_\gamma \propto a^{-4}(t)$. The mean temperature of photons at the present day can be precisely measured by experiments (e.g. COBE satellite, Mather et al., 1999) measuring the Cosmic Microwave Background (CMB). Then the energy density of radiation can be precisely calculated.

- **Matter**

  The equation of state for matter is $w = 0$, and the energy density of photons is $\rho_{\rm m} \propto a^{-3}(t)$. However, there are two different kinds of matter in the universe. One is observable baryons because they can interact with human beings or their instruments. The other one is dark matter that has yet to be directly detected by humans, because it mainly interacts with baryons via gravity. The ways of determining the density of the baryons include: observing the baryons (e.g. hot gas) in galaxies, looking at the distant quasar spectra or the anisotropies in the CMB which depend on the density of baryons. The measurement of the density of dark matter is different from those of the baryons, due to the dark matter not interacting with light. One way to measure the density of dark matter is to measure the clustering of galaxies or clusters at large scales.

- **Dark Energy**

  The simplest equation of state for dark energy is $w = -1$. The energy density of dark energy is $\rho_\Lambda \propto a^0(t)$. Outside of this, we barely know anything about the dark energy and its properties, which makes the dark energy one of the biggest mysteries in astronomy. The existence of dark energy was pointed out by two sets of evidence: observations of the anisotropies in the CMB (Spergel et al., 2003) and the measured luminosity distance-redshift relation inferred from by observing super-novae (Riess et al., 1998; Perlmutter et al., 1999).

The total energy density is the sum of the energy density of the three components,

$$\rho_{\rm tot} = \rho_{\rm m} + \rho_\gamma + \rho_\Lambda. \tag{1.1.4}$$

In order to study and compare different cosmological models, it becomes convenient to rescale the aforementioned energy densities of the different components to be dimensionless density parameters $\Omega_i(t)$, where

$$\Omega_i(t) = \rho_i(t)/\rho_{\rm crit}(t) \quad \rho_{\rm crit} = \frac{3H^2(t)}{8\pi G}, \qquad i \in \{{\rm m}, \gamma, \Lambda\}. \tag{1.1.5}$$

After introducing the curvature density, $\Omega_K(t)$, with the definition

$$1 - \sum_i \Omega_i(t) = -\frac{K}{H^2(t)a^2(t)} \equiv \Omega_K(t), \tag{1.1.6}$$

the **Freidmann-Lemaître** equations 1.1.2 can be written in a very compact form

$$\Omega_{\rm m}(t) + \Omega_\gamma(t) + \Omega_\Lambda(t) + \Omega_K(t) = 1, \tag{1.1.7}$$

or

$$H(t) = H_0\sqrt{\sum_i \Omega_i a(t)^{-3(1+w_i)} + \Omega_K a^{-2}(t)}, \tag{1.1.8}$$

where H_0 and Ω_i are the values of $H(t)$ and $\Omega_i(t)$ at the present day respectively. Once the parameters H_0, Ω_i and Ω_K are determined, the evolution of the model universe can be predicted by the above equations. The theoretical framework for studying the universe has been built. In this theoretical framework, we are able to confront our theoretical prediction with the observations.

1.1.3 ΛCDM model

With the growing amount of observational data in astronomy, particularly precise measurements of the CMB and the large volume of galaxy surveys, we are able to determine the constituents of the universe and the present day values of the aforementioned parameters of the cosmological model (e.g. H_0, Ω_i) with impressive accuracy. The measurements of these parameters led to the currently favoured **concordance model**, which shows that the present universe is almost flat, $\Omega_k = 0$ (e.g. Hinshaw et al., 2012), and consists of about one third of "cold dark matter" (CDM) whilst the other two thirds dark energy, which is barely understood. This model is also called the **ΛCDM Model** named after the two main components in this model universe.

In this section, we introduced the theoretical framework that provides an outline of the history of the universe, which is fundamental for the discussion of galaxy formation in later chapters. Further details of this subject can be found in Peebles (1993); Peacock (1999); Coles & Lucchin (2002); Dodelson & Efstathiou (2004). However, for the evolution of the universe at early times, the model needs to be enhanced by incorporating the theory of inflation. The enhanced model can better describe the evolution of the early universe and also solve several other problems, for example the flatness problem and horizon problem. Further details can be found in textbooks, e.g. Linde (2005).

1.2 Satellite Galaxies

1.2.1 Dark matter haloes

The previous section discussed the evolution of the universe as a whole with the assumption that the universe is uniform and isotropic at cosmological scales. If the universe is perfectly uniform and isotropic at any scale, then there would be no structure formation (including galaxies). The mechanism that drives structure formation is **gravitational instablility**, which amplifies small fluctuations in the density distribution. These small fluctuations can be introduced by inflation, in

which quantum fluctuations in the vacuum energy can produce density perturbations. In the early stages of the universe, these fluctuations are very small and can be treated as perturbations around the smooth background. Therefore we keep only terms of first order and drop all other quadratic terms for simplicity. We call this "linear theory" and the regime where this approach is valid is the "linear regime". The perturbations to photons remain small at all cosmological epochs, because the perturbations have been frozen since decoupling. Therefore the evolution of anisotropies in the photon distribution can be analytically calculated with great accuracy. The observations of the CMB agree very well with the theoretical results estimated from linear theory (Page et al., 2003).

When the universe is matter dominated, the evolution of the matter density perturbations is most likely responsible for the structure in the universe. The perturbations in the matter density can be described by the dimensionless density contrast: $\delta(\vec{r}) = \rho_{\rm m}(\vec{r})/\bar{\rho}_{\rm m} - 1$. In practice, we use Fourier transformed density contrast $\delta(k)$, which makes the calculation simpler. When $\delta \ll 1$ at all scales at early times, linear theory works well. Due to gravitational instability, δ grows with time. When δ reaches the point $\delta \simeq 1$, the linear approximation starts to fail and nonlinear effects start to be important in the evolution of δ. The nonlinear evolution of the density field is very complicated and cannot be described analytically. The best way to study the nonlinear evolution is by using large numerical simulations. However, there are some analytical models that can approximately describe several special cases of nonlinear evolution.

For example, the spherical collapse model (Gunn & Gott, 1972) describes the evolution of a spherical, homogeneous perturbation that is embedded in a homogeneous background universe. This model shows that the high density regime collapses and decouples from the background, which then forms a virialized object called a dark matter halo. The model also predicts the halo is about $\Delta_{\rm vir} \simeq 178$ denser than the background, if $\Omega_{\rm m} = 1$. Then we can define the virial mass of the halo as

$$M_{\rm vir} = (4\pi/3)\bar{\rho}_{\rm m}\Delta_{\rm vir}r_{\rm vir}^3, \tag{1.2.9}$$

where $r_{\rm vir}$ is the virial radius (defined as the radius of the halo in which the

energy distribution satisfies the virial theorem) of the halo.

1.2.2 Galaxy formation

Dark matter haloes are believed to be the cradles of galaxy formation (White & Rees, 1978). When dark matter collapses to form dark matter haloes, because the dark matter particles are collisionless, dark matter haloes relax to a quasi-equilibrium state. However for the baryonic matter in the dark matter haloes, the collapse creates strong shocks that raise the entropy of the material. If the baryonic matter cannot cool, it remains as hot gas and then no galaxies can form. As an essential ingredient of galaxy formation, the cooling depends on the gas temperature and density and there are a variety of cooling processes that can affect hot gas, which mainly include bremsstrahlung emission for hot gas where $T \gtrsim 10^7$ K, excitation and de-excitation mechanisms for the hot gas where 10^4 K $< T < 10^6$ K. As the hot gas cools and flows inwards, self-gravity will eventually dominate over the gravity of the dark matter. The collapse of gas under its own gravity may eventually form stars, assembling a visible galaxy. The basic idea of galaxy formation is not complicated, however many details of the processes involved in galaxy formation are still unclear. By comparing galaxy formation models with the observations, we hope to understand the complicated physics involved in galaxy formation.

Since galaxy formation is complicated, numerical simulations again are powerful tools to study it. Both gasdynamic simulations (e.g. Monaghan, 1992; Couchman et al., 1995) and semi-analytical models (e.g. White & Frenk, 1991; Kauffmann et al., 1993; Cole et al., 1994) require large numerical simulations. In the Chapter 5, we will compare one semi-analytical model, GALFORM, with the observations. Thus afterwards our brief introduction will focus on the semi-analytical models (see e.g. Baugh, 2006, for a more detailed review of semi-analytical models). Semi-analytical models need three basic pieces of information about dark matter haloes:

- **The abundance of dark matter haloes**.

- **The assembly of dark matter haloes**. In the ΛCDM cosmological model, dark mater haloes grow hierarchically. Small haloes can merge into larger haloes and survive there as subhaloes, the galaxies in these subhaloes may become satellite galaxies of the main haloes.

- **The structure of dark matter haloes**. The internal structure of dark matter haloes is important for determining the rate of gas cooling and the size and dynamics of galaxies.

As well as the information from dark matter haloes, the semi-analytical galaxy formation models need more complicated elements,"gastrophysics". The physics behind these processes are, in general, poorly understood. The semi-analytical models introduce parameters to account for this. The values of these parameters are set by comparing the outputs of models with observations. The basic ingredients include:

- **gas cooling**. Gas cooling is a key process of galaxy formation, which provides the raw material for the star formation. (e.g. White & Frenk, 1991).

- **star formation**. The physics of star formation is complicated and still unclear. Due to this, semi-analytical models adopt only a simple estimate of the global rate of star formation in model galaxies, for example

$$\dot{M}_* \propto \frac{M_{\rm cold}}{\tau}, \tag{1.2.10}$$

  where $M_{\rm cold}$ is the amount of cold gas available and τ is a characteristic timescale. The actual star formation laws in current galaxy formation models (e.g. GALFORM) are more sophisticated than this (Lagos et al., 2011).

- **feedback processes**. From observations, the early modellers have already realised that the efficiency of galaxy formation could be a function of halo mass. There are several mechanisms that can modulate the efficiency. The most common of these mechanisms is regulating star formation for low-mass galaxies by a supernova driven wind (Larson, 1974), which suppress

the formation of faint galaxies. While another mechanism, AGN feedback, (e.g. Granato et al., 2004; Monaco & Fontanot, 2005) suppresses gas cooling in haloes and is able to reduce the efficiency of galaxy formation in massive haloes.

- **chemical evolution**. The formation of stars changes the metal content of the interstellar medium (ISM) of a galaxy. It affects the rate of gas cooling, the evolution of subsequent generations of stars and the dust optical depth of a galaxy.

- **galaxy mergers**. Dark matter haloes are assumed to grow through mergers and accretion. White & Rees (1978) argued that galaxies can survive the merger of their parent haloes. Therefore, it is possible that a dark matter halo contains a massive central galaxy surrounded by smaller so-called *satellite galaxies*. These satellite galaxies were formerly central galaxies in the progenitors of the current halo which existed in the earlier stages. As the satellites orbit the central galaxy, they gradually lose energy due to dynamical friction. Eventually the satellite galaxies merge into the central galaxy.

1.2.3 Statistical properties of galaxies

To compare the model galaxies with real galaxies, in this thesis, we mainly focus on two statistical quantities of the galaxy population.

Luminosity function

Luminosity is arguably thought of as one of the most fundamental properties of galaxies. Therefore, an important statistic of the galaxy distribution is the luminosity function, $\phi(L)dL$. It describes the number density of galaxies with luminosities in the range $L \pm dL/2$. In general, the galaxy luminosity function is commonly fitted by a Schechter function (Schechter, 1976) of the form

$$\Phi(L)dL = \Phi^* \left(\frac{L}{L^*}\right)^{\alpha} \exp\left(-\frac{L}{L^*}\right) \frac{dL}{L^*}. \tag{1.2.11}$$

Here L^* is a characteristic luminosity, α is the faint-end slope, and Φ^* is an overall normalization. The luminosity function of galaxies depends on not only waveband, but the properties of galaxies such as morphological type, colour and environment. One of the basic challenges for galaxy formation models is to reproduce the same shape of the luminosity functions as we observe.

Projected radial density profile

The luminosity function reflects the distribution of galaxies over luminosity, whilst the second statistic of the galaxy population that we will consider, the projected radial density profile which describes the distribution of galaxies over the space. For dark matter haloes, Navarro et al. (1996, 1997) found the radial density profiles follow a universal form

$$\rho(r) = \frac{\delta_c \rho_c}{(r/r_s)(1 + r/r_s)^2}, \tag{1.2.12}$$

where ρ_c is the critical density, δ_c is the characteristic overdensity of the halo and r_s is a characteristic scale length. It is remarkable that the spatial distribution of dark matter substructures, which could host satellites galaxies, also follows this universal form independent of the mass of the substructures (Diemand et al., 2004; Springel et al., 2008a; Ludlow et al., 2009). Since the satellite galaxies are closely related to the substructures, the study of the radial distribution of satellite galaxies will help us to understand galaxy formation.

1.3 Studies of Galactic Satellite Galaxies

The ΛCDM model predicts that structure forms in a hierarchical manner. Large spiral galaxies like the Milky Way (MW) and M31 form within extended dark matter halos from the merging and accretion of smaller subhalos. Smaller structures falling into bigger haloes can survive there as substructures and host observed satellite galaxies. The spatial distribution and intrinsic properties (e.g., luminosity function) of satellites are thus intimately bound up with halo merger histories, which are themselves closely related to the underlying cosmology. On

the other hand, the physical processes driving galaxy evolution have strong effects on satellites.

In this thesis, we focus on the isolated galaxies and their satellites mainly for two reasons. One is that we want to know whether the Milky Way, our home, is typical comparing with other similar galaxies either in the real universe or our galaxy models. Second is that the isolated systems are less possibly affected by their environment, such as galaxy-galaxy tidal forces. Therefore, they are most suitable to compared statistically with model predictions.

A strong prediction of the theory, borne out by high resolution N-body simulations, is that a very large number of such dark matter substructures should survive in galactic halos (Klypin et al., 1999; Moore et al., 1999; Diemand et al., 2007; Springel et al., 2008b). Empirical tests of this prediction have so far been restricted to a single system, the Local Group, the only one for which an estimate of the satellite luminosity function (LF) is readily available. Indeed, Klypin et al. (1999) and Moore et al. (1999) noted that the observed number of satellites around the MW and M31 is much smaller than the number of predicted substructures, giving rise to the so-called "missing satellites problem" of the ΛCDM model.

The galactic satellites are usually faint and dwarf galaxies, which are difficult to observe. Thus in the past decade or so, fainter satellites around the MW and M31 have been discovered in the SDSS (e.g. Belokurov et al., 2008, 2010; Grebel, 2000; Irwin et al., 2007; Liu et al., 2008; Martin et al., 2006, 2008; Simon & Geha, 2007; van den Bergh, 2000; Watkins et al., 2009; Zucker et al., 2004, 2006, 2007), but the number is still orders of magnitude smaller than the predicted number of surviving cold dark matter subhalos. A number of solutions to this problem have been proposed. Some invoke a different kind of dark matter, warm dark matter, in which case the number of surviving substructures is dramatically reduced by a cutoff in the primordial power spectrum (Moore et al., 2000; Spergel & Steinhardt, 2000; Yoshida et al., 2000; Bode et al., 2001; Craig & Davis, 2001; Lovell et al., 2012). Others retain cold dark matter and appeal to galaxy formation processes, such as photoionization and supernova feedback, to inhibit star

formation in small subhalos thus rendering most of them invisible. This idea, first mentioned nearly 20 years ago by Kauffmann et al. (1993), was worked out in detail a decade later using analytical arguments and semi-analytical models (Bullock et al., 2000; Benson et al., 2002; Somerville, 2002).

The discovery of new Local Group satellites in the SDSS has stimulated further observational and, particularly, theoretical work. Koposov et al. (2008) and Tollerud et al. (2008) extended the estimate of the satellite LF of the MW and M31 to faint magnitudes, accounting for the survey magnitude limit and modelling the radial density profile of the satellite distribution. This extension to faint magnitudes agrees remarkably well with the ΛCDM model predictions of Benson et al. (2002), a result that has been confirmed in recent work using related semi-analytic modelling techniques (Koposov et al., 2009a; Muñoz et al., 2009a; Busha et al., 2010a; Cooper et al., 2010a; Macciò et al., 2010; Li et al., 2010; Font et al., 2011a). Full N-body/gasdynamic simulations have also been carried out to investigate the physics of satellite galaxies (Libeskind et al. (2007a); Okamoto & Frenk (2009a); Okamoto et al. (2010); Wadepuhl & Springel (2011)) although currently these simulations only resolve the brightest examples. In spite of this broad agreement, interesting discrepancies exist. For example, the original model of Benson et al. (2002), as well as the more recent model by Guo et al. (2011), rarely produce satellites as bright as the LMC and SMC (Boylan-Kolchin et al., 2010).

In the cold dark matter (CDM) cosmological model, the density profiles of dark matter haloes follow a universal form (Navarro et al., 1996, 1997, hereafter NFW profiles) with an inner cusp, $\rho(r) \propto r^{-1}$, and an outer slope of $\rho(r) \propto r^{-3}$. The transition scale, r_s, is normally specified through the concentration, $c = r_{200}/r_s$, where r_{200} is defined as the radius enclosing a mean interior density 200 times the critical density. Besides the overall mass profile, it is remarkable that the spatial distribution of dark matter substructures, which could host satellites galaxies, also follows this universal form independent of the mass of the substructures (Diemand et al., 2004; Springel et al., 2008a; Ludlow et al., 2009). Statistically robust number density profiles of observed satellites will cer-

tainly help us understand how satellite galaxies populate the substructures. In addition, a reliable density profile is required to extrapolate the incomplete observational data of satellites around the MW and M31 to compare with models (e.g. Koposov et al., 2008; Tollerud et al., 2008).

The recognition of the importance of satellite galaxies has resulted in many studies. Early studies were limited by the relatively small satellite samples available at the time (Holmberg, 1969; Lake & Tremaine, 1980; Vader & Sandage, 1991; Lorrimer et al., 1994; Zaritsky et al., 1993, 1997a). Limited by the volume of sample, most of studies focused on fitting the slope of the density profile of satellite galaxies around isolated primaries. With the advent of large galaxy redshift surveys such as the 2dF Galaxy Redshift Survey (2dFGRS; Colless et al., 2001) and the SDSS (York et al., 2000), it is now possible to construct external galaxy samples spanning a much larger volume. Studies with significantly improved statistics have been carried out using these new surveys. For example, Sales & Lambas (2004) studied the spatial distribution of satellites around primaries using the 2dFGRS. The dependence of the profiles on the colour and morphology of primaries has begun to be explored (e.g. Sales & Lambas, 2005; Chen et al., 2006). Yang et al. (2006) studied how spectroscopically identified satellite galaxies were distributed in SDSS groups relative to the orientation of the central galaxy. Klypin & Prada (2009) studied the projected number density profiles and velocity dispersion around isolated red primaries using the SDSS redshift sample. More et al. (2009) used an iterative method, tested on mock galaxy catalogues, to find satellite systems around central galaxies with a range of luminosities in the SDSS. The distribution of velocities of the satellites was used to infer mass-to-light ratios as a function of central galaxy luminosity. Closely related to this are studies of the radial distributions of satellite galaxies in clusters, groups (Li et al., 2007; Wang et al., 2011) and on smaller scales (Watson et al., 2012). Further work has focused on the distribution of satellites around intermediate redshift galaxies (Nierenberg et al., 2011), elliptical primaries (Smith et al., 2004) and isolated galaxies in the SDSS (Lares et al., 2011). Besides the studies that statistically estimate mean number density profiles, Kim et al. (2011) have

directly measured the number density profile of the nearby field galaxy M106.

Meanwhile, astronomers realise that confronting the theories or models only with the satellites of the Local Group is not statistically robust. We shall compare our models with statistically representative samples of galaxies and their satellites. However, analyzing satellites of external galaxies is not easy, because, firstly, current observations are usually not deep enough, averaging, only one or two satellites per primary, and secondly, the real positions of satellites relative to their primaries are uncertain due to the redshift space distortion. To circumvent the aforementioned problems, we (Guo et al., 2011, hereafter Paper I, See also Chapter 2) have developed a method of stacking the primaries and their satellites in order to obtain a fair and complete sample that can yield statistically robust results for certain classes of primary galaxies. This method has been successfully applied to the estimation of the satellite luminosity functions of isolated primary galaxies in the SDSS.

The observations of satellites with significantly improved accuracy also provide us with excellent opportunities to test our cosmological model and the galaxy formation models. Some studies have attempted to make model predictions using cosmological hydrodynamic simulations (e.g Libeskind et al., 2007b; Okamoto & Frenk, 2009b; Okamoto et al., 2010; Wadepuhl & Springel, 2011; Parry et al., 2012), these efforts are limited to very few primary galaxies because of the high computational cost. The best way to make a statistical sample of model galaxies is by combining large cosmological dark matter simulations, such as the Millennium Simulation (MS, Springel et al., 2005) or the MS-II (Boylan-Kolchin et al., 2009), with a method to include galaxies. This approach was adopted by van den Bosch et al. (2005), who used the conditional luminosity function technique that simultaneously optimizes the model match to the abundance and clustering of low luminosity galaxies in order to study the satellite projected number density profile. Chen et al. (2006) investigated the same statistic by assigning luminosities to dark matter structures so as to match the simulated cumulative circular velocity function to the SDSS cumulative galaxy LF. A similar subhalo abundance matching method was used by Busha et al.

(2011) to study the frequency of bright satellites around MW-like primaries.

Semi-analytic models provide a more physically motivated approach to including galaxies into dark matter simulations and have been shown to match a wide variety of observational data (e.g Kauffmann et al., 1993; Lacey et al., 1993; Cole et al., 1994; Kauffmann et al., 1999; Somerville & Primack, 1999; Cole et al., 2000; Benson et al., 2002; Baugh et al., 2005; Bower et al., 2006; Croton et al., 2006; Guo et al., 2011). A large number of studies have used this technique applied to simulations such as the MS-II, Aquarius (Springel et al., 2008a) and others to study various aspects of the galaxy population predicted in a ΛCDM model (e.g Muñoz et al., 2009b; Cooper et al., 2010b; Li et al., 2010; Macciò et al., 2010; Font et al., 2011b; Wang et al., 2012; Wang & White, 2012). In particular, the mock catalogues constructed by Guo et al. (2011) were tested against data from the SDSS in two studies. Sales et al. (2012) showed that the abundance of satellite galaxies as a function of primary stellar mass in the SDSS DR7 spectroscopic catalogue was in good agreement with this model. Considering fainter dwarf satellites, Wang & White (2012) studied the luminosity, colour distribution and stellar mass function using SDSS DR8 data, concluding that, apart from the model satellites becoming red too quickly when entering the halo of the primary galaxy, many of the observed trends were reproduced in the model. Comparing the properties of real galactic satellites with those of model galactic satellites can certainly help us to verify galaxy formation models at such small scales (e.g. Wang & White, 2012; Guo et al., 2013). The results of these comparisons show that the semi-analytical models achieve some non-trivial success. However, the models also have difficulties to reproduce the same fraction of "blue" satellites as in the observations.

In this thesis, we measured the luminosity functions and projected number density profiles of galactic satellite around isolated primaries of different luminosities by using the SDSS photometric and spectroscopic samples. We also measure these quantities for model satellites placed into the Millennium and Millennium II dark matter simulations by GALFORM. We compare our model predictions to SDSS data. We find that the radial distributions of model satel-

lites can be fitted by an NFW profile similar to those around comparable primary galaxies in the SDSS DR8, with only slight differences at low luminosities and small projected radii. However, when splitting the satellites by colour, the model and SDSS satellite systems no longer resemble one another, with many red model satellites, in contrast to the dominant blue fraction at similar luminosity in the SDSS. The few model blue satellites are also significantly less centrally concentrated in the halo of their stacked primary than their SDSS counterparts. We discuss how these discrepancies may reflect inadequacies in the treatment of the processes that determine the star formation histories of small galaxies in the model (e.g., hot gas stripping, chemical evolution and star formation history). It could help us improve the GALFORM model.

1.4 Thesis Overview

In this section, we provide a short overview of the contents of the following chapters.

Chapter 2: We develop a method that selects isolated primaries from the SDSS spectroscopic sample and search for potential satellites in the much deeper photometric sample. Then, we measure the luminosity function of satellites around these isolated primaries. We also study how the satellite luminosity function varies with the luminosity, colour and concentration of the primary.

Chapter 3: Based on the method we develop in Chapter 2, we measure the radial density profiles of satellites around isolated primaries, and find that the normalized profiles can be well fitted by projected NFW profiles. Moreover, we show how the radial distribution of satellites depends on the colour and luminosity of satellites and primaries. Finally, we also explore the angular distribution of satellites around the isolated primaries and find no statistically significant evidence that the angular distribution of satellites around the isolated primaries is anisotropic.

Chapter 4: In the methods which count satellites around isolated primaries, there are two different ways to estimate the number of background galaxies,

which, quite obviously, affect the estimation of satellite luminosity functions. We compare these two different ways of counting background galaxies, and explore the possible factors that account for the differences we find.

Chapter 5: We investigate the luminosity functions and radial number density profiles of galactic satellites around isolated primaries of different luminosity. To test the semi-analytical model, GALFORM, we measure these quantities for model galaxies created by the GALFORM model and compare the predictions of the model to the results measured from SDSS data in the previous chapters. We discuss the implications of the results for the GALFORM model.

2

SATELLITE LUMINOSITY FUNCTIONS FOR PRIMARIES IN SDSS

In this chapter, we study the luminosity function of satellite galaxies around isolated primaries using the Sloan Digital Sky Survey (SDSS) spectroscopic and photometric galaxy samples. We select isolated primaries from the spectroscopic sample and search for potential satellites in the much deeper photometric sample. For primaries of similar luminosity to the Milky Way and M31, we are able to stack as many as $\sim 20,000$ galaxy systems to obtain robust statistical results. We derive the satellite luminosity function extending almost 8 magnitudes fainter than the primary galaxy. We also determine how the satellite luminosity function varies with the luminosity, colour and concentration of the primary. We find that, in the mean, isolated primaries of comparable luminosity to the Milky Way and M31 contain about a factor of two fewer satellites brighter than $M_V = -14$ than the average of the Milky Way and M31.

2.1 Introduction

The large body of work on satellite galaxies reflects the importance of these objects as a critical test of the ΛCDM model on small scales. Yet, all conclusions to date regarding the validity or otherwise of the model rely on comparison with data for a few dozen satellites around just two galaxies, the MW and M31. There is no guarantee that these are typical and indeed there is good evidence that the satellites of the two galaxies have different structural properties (McConnachie &

Irwin, 2006; Collins et al., 2010). Clearly, robust and reliable tests of cosmological and galaxy formation models require comparison with statistically representative samples of galaxies and their satellites.

Analyzing the satellite systems of external galaxies is challenging because typically only one or two satellites are detected per primary galaxy (Holmberg, 1969; Lorrimer et al., 1994; Zaritsky et al., 1993, 1997a). In addition, the real space position of the satellite with respect to its primary is uncertain. To circumvent the first problem, these authors developed the method of stacking the primaries and their satellites in order to obtain a fair and complete sample which can yield statistically robust results for certain classes of primary galaxies. These early studies were limited by the relatively small samples available at the time. With the advent of large galaxy redshift surveys such as the 2dF Galaxy Redshift Survey (2dFGRS; Colless et al., 2001) and the Sloan Digital Sky Survey (SDSS; York et al., 2000), it is now possible to construct external galaxy samples covering a much larger volume. Studies with significantly improved statistics have been carried out using these new surveys (e.g. Sales & Lambas, 2004; Yang et al., 2006; Agustsson & Brainerd, 2010). However, due to limited sample volumes, these studies were only able to measure the number density or spatial distribution of satellite galaxies with relative large uncertainty.

In this work, we are interested in the satellite luminosity function of specific types of isolated primary galaxies and, for this, the new spectroscopic surveys are still not deep enough. For example, even within the largest galaxy redshift catalogue from SDSS DR7 (Abazajian et al., 2009), where there are about $\sim 660\,000$ galaxies with $m_r^{\rm lim} < 17.77$, only a relatively small number of isolated low redshift galaxy systems have enough detected satellites for our purposes (e.g. Hwang & Park, 2010). On the other hand, the photometric catalogue from SDSS DR7 contains $\sim 96\,000\,000$ galaxies with magnitudes in the u, g, r, i, z bands (roughly $m_r^{\rm lim} < 22$) and photometric redshifts. In this study, we used both the spectroscopic and photometric SDSS DR7 catalogues. To ensure completeness, we restrict the photometric sample in our main analysis to galaxies brighter than $m_r = 20.5$ (see Section 4). The resulting catalogues enable us to analyze a suf-

ficiently large statistical sample of galaxy systems. We construct our sample using methods similar to those developed by Lorrimer et al. (1994) but modified slightly to include photometric redshifts.

As this project was nearing completion, Liu et al. (2011) published an investigation using similar methods to quantify the frequency with which satellites as bright as the LMC and SMC occur around primaries similar to the MW. Shortly afterwards, Lares et al. (2011) also published a similar study, focused on primaries brighter than $M_r < -20.5$, investigating how the satellite LF and projected density profile depend on the primary luminosity and colour. Our work complements these studies by including a wider range of primary luminosities and exploring how the satellite LF depends on the properties of the primary. Also, we adopt stricter isolation criteria than those of Lares et al. (2011). We compare our results with those of these studies in the discussion in Section 2.5.

The remainder of this chapter is organised as follows. In Section 2.2, we describe the selection of primary galaxies and their satellites; in Section 2.3, we develop the method of estimating the satellite LF; in Section 2.4, we present our estimate of the satellite LF for different types of primary galaxy. We conclude, in Section 2.5, with a summary and discussion of our results.

2.2 Data and Sample Selection

We build two different catalogues for our study: a smaller one of galaxies with spectroscopic redshifts from which we select the primary galaxies (hereafter the spectroscopic catalogue) and a larger one of galaxies with photometric redshifts and magnitudes from which we select the neighbouring galaxies (hereafter the photometric catalogue). The spectroscopic catalogue is constructed from the SDSS DR7 spectroscopic subsample (north galactic cap) including all objects with high quality redshifts (zconf > 0.7 and specClass $= 2$) and a Petrosian magnitude $r \leq 17.77$. The photometric galaxy catalogue is from the SDSS DR7 photometric subsample (north galactic cap) and includes only objects that have photometric redshifts, none of the flags BRIGHT, SATURATED, or SATUR_CENTER

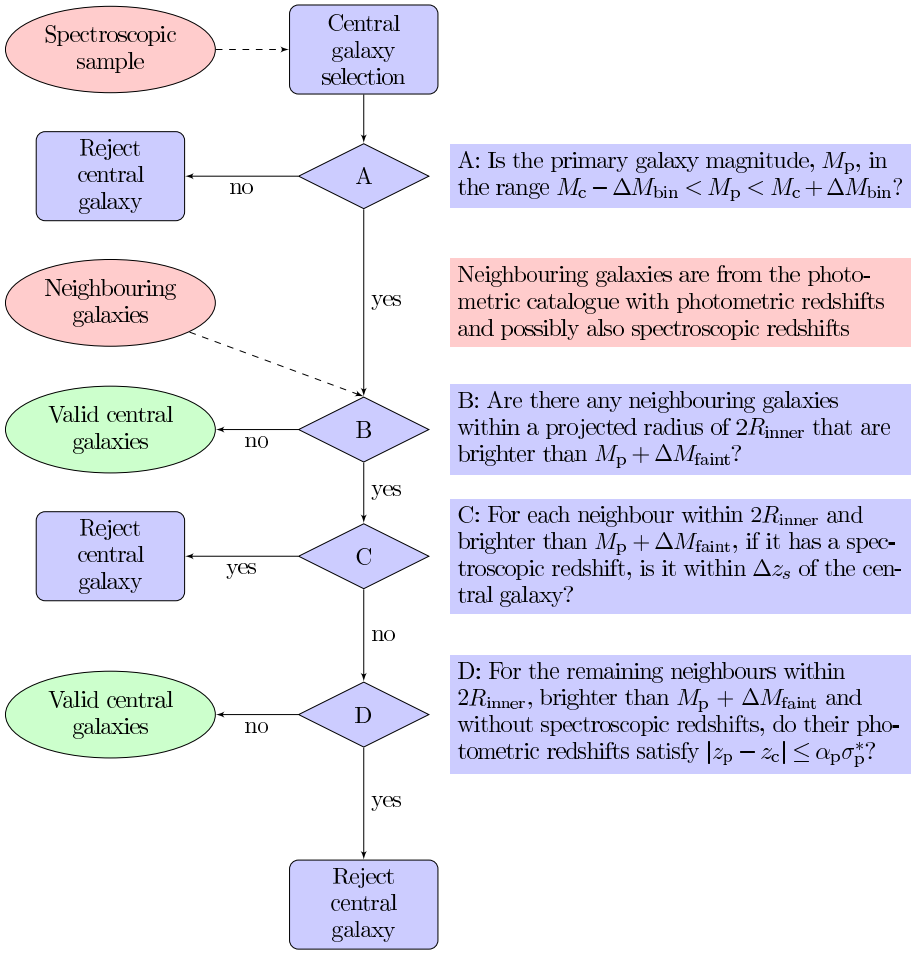

Figure 2.1: A flow chart detailing the selection criteria for isolated primary galaxies.

set and model magnitudes $r \leq 22.0$. We select only objects with corresponding entries in the SDSS database PhotoZ table, which naturally selects galaxies and excludes stars. As galaxies with $r \leq 17.77$ are included in both SDSS catalogues, a small fraction of the photometric catalogue galaxies also have spectroscopic redshifts. To avoid extinction by dust in the Galaxy, we use de-reddened model *ugriz* magnitudes and k-correct all galaxies to $z = 0$ with the IDL code of Blanton & Roweis (2007). In addition, we also include V-band magnitudes estimated from g and r-band magnitudes assuming $V = g - 0.55(g - r) - 0.03$ (Smith et al., 2002). This allows us directly to compare our results with observations of the MW.

For our statistical analysis, the sample of primary galaxies should be not

only homogeneous but also isolated. To this end, we adopt a series of selection criteria summarised in the flow chart shown in Fig. 2.1. First, from the spectroscopic sample, we select primary galaxy candidates of absolute magnitude, $M_{\rm p}$, in the range $M_{\rm C} - \Delta M_{\rm bin} < M_{\rm p} \leq M_{\rm C} + \Delta M_{\rm bin}$. We then reject from this list those candidates that have, or could have, bright neighbours whose own satellite system could overlap with that of the candidate. We achieve this by rejecting candidates that have a neighbouring galaxy within a projected distance of $2R_{\rm inner}$ that is brighter than $M_{\rm p} + \Delta M_{\rm faint}$, unless that neighbouring galaxy is at a substantially different redshift. For neighbours with spectroscopic redshifts, $z_{\rm s}$, the required redshift separation is $|z_{\rm p} - z_{\rm s}| > \Delta z_s$, while for those with only photometric redshifts, $z_{\rm phot}$, we require $|z_{\rm p} - z_{\rm phot}| > \alpha_{\rm p}\sigma_p^*$. Here $\sigma_{\rm p}^*$ is the photometric redshift error that we adopt (see Section 2.3) and $\alpha_{\rm p}$ is a tolerance, which we will vary. The isolation criteria guarantee that there are no luminous neighbouring galaxies that are projected within $2R_{\rm inner}$ of the primary, unless these luminous neighbours are sufficiently far away from the primary and appear here due to a chance projection. Using the photometric redshift information to identify and remove true background and foreground galaxies significantly increases the number of primary galaxies retained in our sample and reduces the background contamination.

After having filtered by these criteria, the remaining isolated galaxies comprise the primary galaxy catalogue. We briefly summarise the properties of this catalogue. The number of primary galaxies not only depends on their absolute magnitude, but also on the isolation parameters. The stricter the isolation criteria we take, the fewer primary galaxies we have. In the V-band, with a parameter set $\{M_{\rm c}, R_{\rm inner}, R_{\rm outer}, \Delta M_{\rm bin}, \Delta M_{\rm faint}, \Delta z_{\rm s}, \alpha_{\rm p}\}$={-21.0, 0.3 Mpc, 0.6 Mpc, 0.5, 0.5, 0.002, 2.5}[1], the number of candidates in the primary magnitude bin $M_{\rm c} = -21.0$ before isolation is 202 351, which, after applying the isolation criteria, is reduced to 21 346 or about 10% of the galaxies in this magnitude bin. The primary galaxy redshifts lie in the range $0.01 < z < 0.16$, with a median

[1]The parameter, $R_{\rm outer}$, is defined below, in Fig. 2.2

Table 2.1: Properties of the primary galaxy samples for the following default choices of values for the sample selection parameters, $\{M_c$, R_{inner}, R_{outer}, ΔM_{bin}, ΔM_{faint}, Δz_s, $\alpha_p\}$=$\{M_c$, 0.3 Mpc, 0.6 Mpc, 0.5, 0.5, 0.002, 2.5$\}$. Quantities listed for each bin of V-band absolute magnitude M_c are: the number of primary galaxy candidates (galaxies within the absolute magnitude bin), the number of primary galaxies that pass all the isolation criteria, their median redshift and redshift range.

M_c	primary candidates	primaries	median redshift	redshift range
-19.0	35893	88	0.043	$0.021 < z < 0.066$
-20.0	104907	2661	0.105	$0.020 < z < 0.068$
-21.0	202351	21346	0.098	$0.016 < z < 0.164$
-22.0	94287	51733	0.142	$0.022 < z < 0.391$
-23.0	51686	26982	0.203	$0.031 < z < 0.522$

redshift 0.098. For different primary magnitudes, M_c, the number of primary galaxies and their median redshifts are shown in Table 2.1. For each magnitude bin, the number of primary candidates is determined by the interplay between the accessible volume given the survey limit and the density of galaxies. The actual number of primaries is further affected by the isolation criteria which, for example, tend to reject nearby galaxies for which $2R_{inner}$ subtends a large angle.

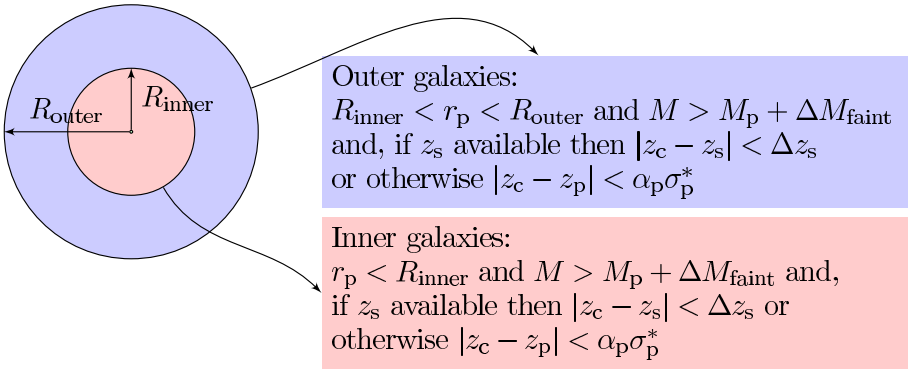

Figure 2.2: Schematic showing the selection of potential satellite galaxies within $R_{\rm inner}$ and of a reference sample within an annulus defined by $R_{\rm inner} < r < R_{\rm outer}$, used to subtract the residual contaminating background. For both samples we apply the stated redshift cuts to reduce background contamination. We also apply the stated absolute magnitude cut to both samples (assuming the neighbouring galaxies are at the same redshift as the primary) though this cut is redundant unless $R_{\rm outer} > 2R_{\rm inner}$ as otherwise the existence of such bright neighbouring galaxies would automatically lead to the exclusion of the primary galaxy.

The schematic in Fig. 2.2 indicates our selection procedure for potential satellites or "inner galaxies", and the corresponding selection of the "outer galaxies" used to define the background. We assume the satellites of the primary galaxy fall within a projected radius, $R_{\rm inner}$ (the red circle in Fig. 2.2). To reduce the background contamination, we apply the same cuts in redshift (spectroscopic and photometric) as were applied when selecting the primary galaxies, but as most of the galaxies within $R_{\rm inner}$ only have photometric redshifts with quite large measurement errors, we still cannot distinguish true satellites from projected background galaxies. However, the existence of satellites will make the number density of galaxies within $R_{\rm inner}$ slightly larger than that in the outer blue reference annulus in Fig. 2.2 ($R_{\rm inner} < r < R_{\rm outer}$). By counting the difference between the number density of galaxies within $R_{\rm inner}$ and in the reference annulus, we can estimate the number of true satellites.

An example of the objects we detect around a typical primary galaxy is shown in Fig. 2.3. This image, produced by the SDSS finding chart tool[2], illustrates the quality of the data and shows that candidate satellites are spatially well separated from the light distribution of the primary galaxy. The white circle (slightly stretched in this Aitoff projection) indicates $r = R_{\rm inner}$. Within this region we have marked all the galaxies in our catalogue with red circles and the subset brighter than $m_r = 20.5$, used in our main analysis, with yellow boxes. The remaining visible objects within $R_{\rm inner}$ are not in our catalogue. Manual inspection with the DR7 Navigate tool reveals them to be classified as stars.

2.3 Estimating the Satellite Luminosity Function

Once the primary galaxies are defined, their potential satellites are found from the photometric galaxy catalogue as depicted in Fig. 2.2. For the ith primary galaxy, the number of inner galaxies, $N_i^{\rm inner}(M)$, is found by counting all neighbouring galaxies within the inner area that satisfy the following conditions: at least $\Delta M_{\rm faint}$ fainter than the primary; if they have a spectroscopic redshift, $z_{\rm s}$, then it should satisfy $|z_{\rm c} - z_{\rm s}| < \Delta z_{\rm s}$; or if they only have a photometric redshift $z_{\rm p}$, then it should satisfy $|z_{\rm c} - z_{\rm p}| < \alpha_{\rm p}\sigma_{\rm p}^*$, where $\sigma_{\rm p}^*$ is the error in the photometric redshift as defined below. The number of outer galaxies, $N_i^{\rm outer}(M)$, is determined by applying the same conditions to galaxies in the outer area. As most satellites of the primary should be projected within $R_{\rm inner}$ of the primary, the number density of inner galaxies should typically exceed that of the outer galaxies. The excess can be taken as the projected satellite LF of the ith primary galaxy, and estimated by

$$N_i^{\rm sat}(M) = N_i^{\rm inner}(M) - \frac{A_i^{\rm inner}}{A_i^{\rm outer}} N_i^{\rm outer}(M), \tag{2.3.1}$$

where $A_i^{\rm inner}$ and $A_i^{\rm outer}$ are the areas of the inner and outer regions respectively (excluding sub-regions not within the sky coverage of the SDSS DR7, which we have identified using the mask described in Norberg et al. (2011)).

[2]http://cas.sdss.org/dr7/en/tools/chart/chart.asp

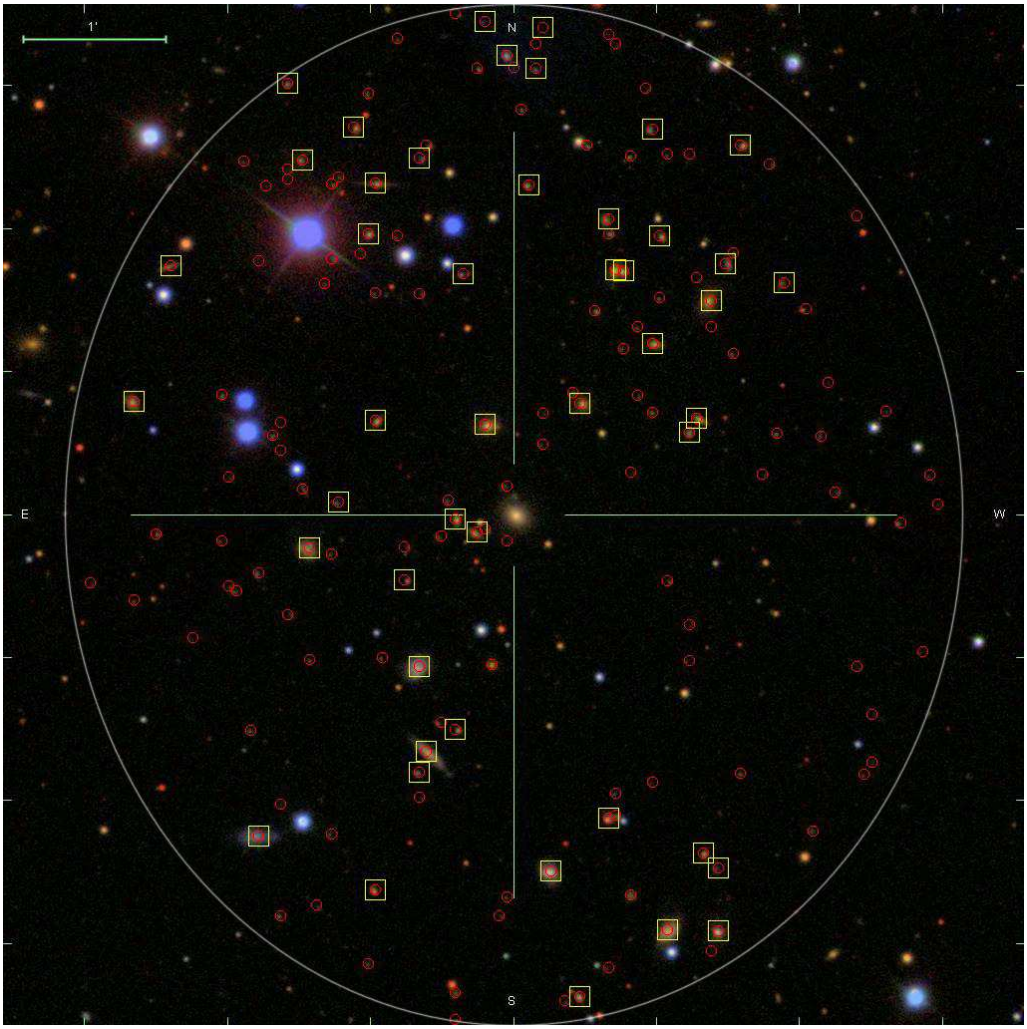

Figure 2.3: An example SDSS DR7 image centred on a primary galaxy of magnitude $m_r = 16.10$ at redshift $z = 0.074$. The white ellipse marks $r = R_{\rm inner} = 300$ kpc. All catalogued galaxies projected within $R_{\rm inner}$ of the primary are marked with red circles. Those brighter than our fiducial $m_r = 20.5$ magnitude limit are marked with yellow boxes. The remaining unmarked images within $R_{\rm inner}$ are presumed to be classified as stars, which we have verified in this case using the manual SDSS DR7 Navigate Tool.

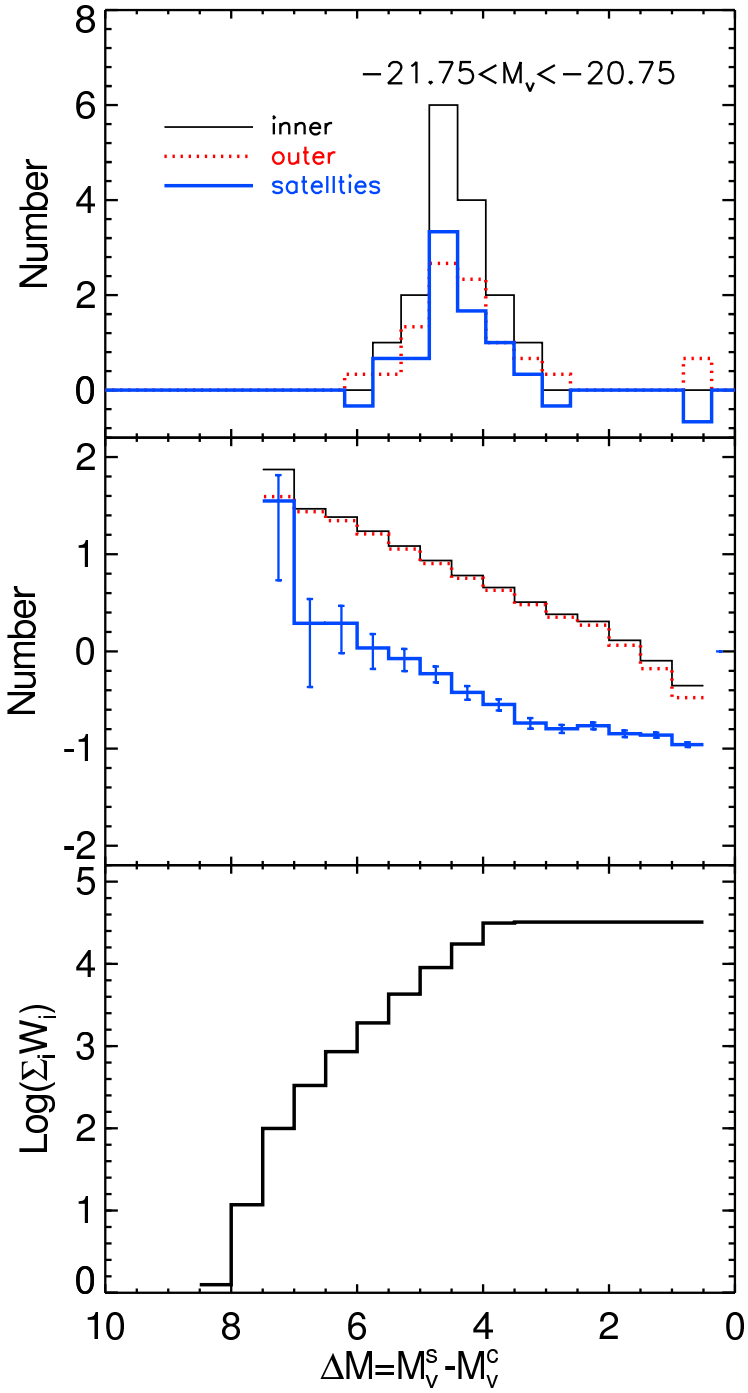

Figure 2.4: Estimation of the satellite luminosity function. The top panel shows the *V*-band LF for a single primary galaxy. The middle panel shows the mean satellite LF of all primary galaxies. The black (thin) and red (dotted) lines give the counts of inner and outer galaxies respectively and the blue (thick) lines the estimate of the satellite LF. (Continued on the following page.)

Figure 2.4: (continued) The number of primary galaxies contributing to the mean satellite LF in each bin is shown in the bottom panel. Here the selection parameters, $\{R_{\rm inner}, R_{\rm outer}, \Delta M_{\rm bin}, \Delta M_{\rm faint}, \Delta z_{\rm s}, \alpha_{\rm p}\}$, are set to the default values {-21.25, 0.3 Mpc, 0.6 Mpc, 0.5, 0.5, 0.002, 2.5}

Because of the survey apparent magnitude limit, we are able to probe less of the faint end of the satellite LF for primaries at higher redshift. To account for this and construct an unbiased estimate of the satellite LF averaged over all primary galaxies, we count the effective number of primaries contributing to each bin of the LF using the weighting function

$$W_{ij}(M_j) = \begin{cases} 1 & M_j < M_i^{\rm lim} + \Delta M_j \\ \frac{(M_i^{\rm lim} - \Delta M_j - M_j)}{2\Delta M_j} & M_i^{\rm lim} - \Delta M_j \leq M_j \leq M_i^{\rm lim} + \Delta M_j \\ 0 & M_j > M_i^{\rm lim} - \Delta M_j \end{cases}, \qquad (2.3.2)$$

where M_j is the central value of each magnitude bin, ΔM_j is the half width of the bin, $M_i^{\rm lim} = m^{\rm lim} - 5\log_{10}(D_i^L) - K(z_i)$, D_i^L is the luminosity distance of the ith galaxy and $m^{\rm lim}$ is the SDSS galaxy photometric sample magnitude limit and $K(z_i)$ is the k-correction of the primary galaxies at redshift z_i. For a given primary, the weighting function is unity for all magnitude bins in which satellites anywhere in the bin are bright enough to be included in the survey. It is zero if all satellites within the bin are too faint to be included in the survey and ramps between zero and one when only galaxies in a fraction of the bin width are accessible to the survey. We then define the effective number of primary galaxies, $N_j^{\rm prim}$, contributing to the jth bin of the LF as $N_j^{\rm prim} = \sum_i W_{ij}(M_j)$. With this definition, our unbiased estimator of the average satellite LF is given by

$$\widetilde{N}^{\rm sat}(M_j) = \frac{\sum_i N_i^{\rm sat}(M_j)}{N_j^{\rm prim}}. \qquad (2.3.3)$$

In practice, in our study we divide the satellite luminosities, M_j, into 20 bins ($j = 1, 2, \cdots, 20$). Furthermore, because each primary galaxy in the same bin has a slightly different magnitude relative to $M_{\rm c}$, we choose to show our results

in terms of the difference in the magnitude of the satellite and primary galaxy, $\Delta M = M_{\rm s} - M_{\rm p}$, which aligns the satellite LFs in the same bin.

The process of estimating the satellite LF for primaries in one bin of V-band absolute magnitude is illustrated in Fig. 2.4. The thin black histogram in the top panel shows the number of inner galaxies binned by V-band magnitude difference for one of the primaries. The dotted red histogram shows the corresponding number of outer galaxies scaled by the ratio of areas $A_i^{\rm inner}/A_i^{\rm outer}$. Their difference, which is an estimate of the satellite LF in that system, is shown by the thick blue histogram. The thin black and dotted red histograms in the middle panel show the number of inner and (scaled) outer galaxies per prmary where the number of primaries, $N_j^{\rm prim} = \sum_i W_{ij}(M_j)$, contributing at each ΔM is shown in the lower panel. The heavy blue histogram in the middle panel of Fig. 2.4 shows the estimated mean satellite LF for all primaries in the magnitude range $-21.75 < M_{\rm V} < -20.75$. The error bars on this mean satellite LF are estimated by bootstrap resampling of the set of primaries. At the faint end of the LF the error bars become quite large because of the small number of nearby primaries that are able to contribute. If the faintest bin only contains one primary then we show a Poisson, rather than the bootstrap error.

For a specific $M_{\rm c}$, the selection of primaries and counts of inner and outer galaxies are determined by the parameter set $\{R_{\rm inner}, R_{\rm outer}, \Delta M_{\rm bin}, \Delta M_{\rm faint}, \Delta z_{\rm s}, \alpha_{\rm p}\}$. It is important to choose appropriate values for these parameters. Here we discuss the physical motivation for our choice of parameter values and check that the resulting satellite luminosity function is robust to reasonable variations in these parameters. The various panels in Fig. 2.5 show the results of varying these parameters away from our default choice of $\{M_{\rm c}, R_{\rm inner}, R_{\rm outer}, \Delta M_{\rm bin}, \Delta M_{\rm faint}, \Delta z_{\rm s}, \alpha_{\rm p}\}$=$\{M_{\rm c}$, 0.3 Mpc, 0.6 Mpc, 0.5, 0.5, 0.002, 2.5$\}$.

The area within which we search for the satellite signal is determined by the parameter $R_{\rm inner}$. For too small a value of $R_{\rm inner}$, we would lose genuine satellites. Once $R_{\rm inner}$ is sufficiently large to enclose all the true satellites the resulting background-subtracted satellite LF should be independent of $R_{\rm inner}$. However, the statistical error in the estimate will increase due to increased background

contamination. The value of 0.3 Mpc is roughly the virial radius of the Milky Way, and so this seems a reasonable value to take for the $R_{\rm inner}$ of Milky Way-like primary galaxies. One could argue for scaling $R_{\rm inner}$ with the magnitude or type of the primary galaxy, but, for simplicity, we set $R_{\rm inner} = 0.3$ Mpc in this study except in our parameter tests. In Fig. 2.5a, we show that the effect of varying $R_{\rm inner}$ between 0.25 and 0.35 Mpc does not change the satellite LF for Milky Way-like primaries significantly. In following chapter, we will scale the $R_{\rm inner}$ with the different primary magnitudes, which is a more realistic treatment. A possible concern is that the SDSS data reduction pipeline occasionally misclassifies fragments of the spiral arms of bright galaxies as separate galaxies. We have checked that these contaminating objects do not make a significant contribution to our estimate of the satellite luminosity by excluding all galaxies within 1.5 times the Petrosian R_{90} radius of the primary galaxies. Comparison of the resulting satellite luminosity functions shows that they make no significant difference.

The next parameter, $R_{\rm outer}$, determines the outer reference annulus from which we estimate "background" counts. An appropriate value for $R_{\rm outer}$ will guarantee a suitably local estimate of the background. A local estimate of the background is preferable (see Chen et al., 2006) as galaxies are clustered and, in our case, the mean environment of a primary galaxy is also biased by the isolation criteria that we apply. Fig. 2.5b shows that, provided the outer area is sufficiently large to allow an accurate estimate of the background, the resulting satellite LF is robust to changes in $R_{\rm outer}$. We also tested the effect of estimating the background using a larger annulus that was disjoint from the inner region (from 0.5 Mpc to 0.7 Mpc) and again found no significant difference.

Besides the physically motivated parameters, we also test the parameters of the estimation method. For a specific central magnitude, $M_{\rm c}$, the bin half width, $\Delta M_{\rm bin}$, is a compromise between having a large enough sample of primary galaxies and not distorting the LF due to averaging over primaries of differing luminosities. Fig. 2.5c shows results for a few different $\Delta M_{\rm bin}$ values and indicates that, for our choice of binning, the satellite LF by the magnitude

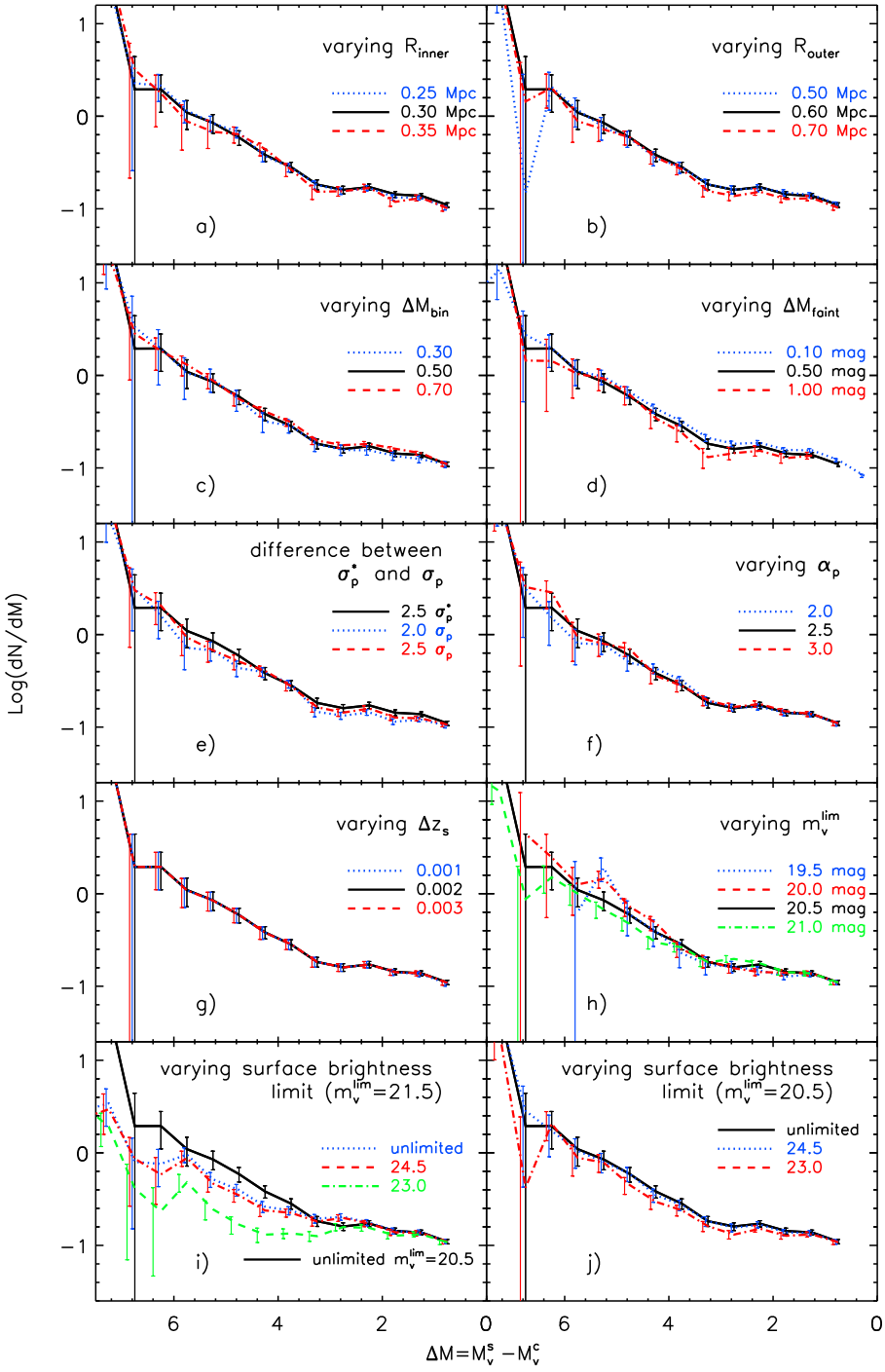

Figure 2.5: The effect on the estimated satellite LF of varying the parameters $\{R_{\rm inner}, R_{\rm outer}, \Delta M_{\rm bin}, \Delta M_{\rm faint}, \Delta z_{\rm s}, \alpha_{\rm p}\}$from their default values, $\{-21.25, 0.3$ Mpc$, 0.6$ Mpc$, 0.5, 0.5, 0.002, 2.5\}$, as indicated in the legends. In addition, panel e shows the effect of changing the assumed photometric redshift error from the original $\sigma_{\rm p}$ to our adopted $\sigma_{\rm p}^* = \max(\sigma_{\rm p}, 0.05)$. (Continued on the following page.)

Figure 2.5: (continued) Panels h,i and j show the effect of varying the apparent magnitude limit of the photometric catalogue and imposing an additional cut on surface brightness (see text for details). In this and in Figs. 6, 7 and 9, the error bars for different datasets have been slightly shifted for clarity.

difference, $\Delta M = M_{\rm s} - M_{\rm p}$, any biases are very small.

The next panel, Fig. 2.5d, shows the effect of varying the parameter $\Delta M_{\rm faint}$, which is important in selecting isolated primaries. The larger $\Delta M_{\rm faint}$, the smaller the number of primary galaxies that survive the isolation filter. Hence, the value of $\Delta M_{\rm faint}$ is a compromise between avoiding the introduction of primary galaxies within groups and gathering sufficient primary galaxies. We adopt $\Delta M_{\rm faint} = 0.5$, but Fig. 2.5d shows that, apart from the truncation of the satellite LF brighter than $\Delta M = \Delta M_{\rm faint}$, the results are, perhaps surprisingly, insensitive to changing to $\Delta M_{\rm faint} = 0.1$ or 1.0. To test further the effect of varying the isolation criteria we have cross matched our primary galaxy catalogue with the Yang et al. (2007) group catalogue. We find that within the DR4 footprint of the Yang et al catalogue only 467 of our $\sim 20\,000$ primary galaxies for our fiducial value of M_c and $\Delta M_{\rm faint} = 0.5$ match with groups of 2 or more galaxies. Excluding these group members from our list of primaries has essentially no effect on the estimated LF and so we conclude that our satellite LF has no significant contamination from group members.

The parameter $\alpha_{\rm p}$ helps us to distinguish genuine satellite galaxies from background galaxies by excluding galaxies that are at a significantly different redshift. If too small a value of $\alpha_{\rm p}$ is used then we will artificially exclude genuine satellite galaxies just because the random error in their photometric redshift happens to be greater than $\alpha_{\rm p}\sigma_{\rm p}$. If the quoted $\sigma_{\rm p}$ were accurate for all galaxies and the errors were Gaussian then $\alpha_{\rm p} > 2$ ought to be sufficient. However the dotted blue and dashed red lines in Fig. 2.5e show that with both $\alpha_{\rm p} = 2$ and 2.5

the satellite LF is systematically underestimated at the faint end. Further investigation has revealed that the cause of the sensitivity is that some galaxies with low values of $\sigma_{\rm p}$ in reality have larger redshift errors due either to non-Gaussian distributions or inaccuracies in $\sigma_{\rm p}$. Hence, for our default selection we have been more conservative and set a floor on the photometric redshift error by adopting $\sigma_{\rm p}^* = \max(\text{œ}_{\rm p}, 0.05)$. Fig. 2.5 shows that with this choice the satellite LF does not depend systematically on $\alpha_{\rm p}$. The photometric redshifts of SDSS galaxies we used is from a hybird method that combines the the template fitting approach of Csabai et al. (2003) and an empirical calibration using objects with both observed colors and spectroscopic redshifts.

Fig. 2.5g shows the dependence of the satellite LF on $\Delta z_{\rm s}$, the maximum allowed spectroscopic redshift difference between a satellite and its primary. This should be large enough so that satellites are not excluded due to the line-of-sight component of their orbital velocities. Our default choice is $\Delta z_{\rm s} = 0.002$, corresponding to a line-of-sight velocity difference of 600 km s^{-1} at $z = 0$. For primaries at different redshifts, the accurate values of $\Delta z_{\rm s}$ should depedent on the redshift of the primaries and satellites. We used $\Delta z_{\rm s} = 0.002$ for all galaxies just for simplicity. The results are actually very insensitive to this value, mainly as only a small fraction of potential satellites and background galaxies in the outer annulus from the photometric catalogue have spectroscopic redshifts.

The final three panels of Fig. 2.5 illustrate the sensitivity of our results to the apparent magnitude and surface brightness cuts that we impose on the photometric catalogue. Fig. 2.5h shows that the satellite LF is systematically suppressed at the faint end if all catalogued galaxies are used to a faint magnitude limit of $m_V = 21.5$, compared to our default of 20.5. Brighter cuts also cause some variation but in this case the samples are becoming smaller and noisier. Figs. 2.5i and j show the effect of applying cuts in surface brightness (mean surface brightness within the Petrosian R_{50} radius) for two different apparent magnitude limits. For a faint magnitude limit of $m_V = 21.5$ the faint end of the LF is very sensitive to the surface brightness cut. This occurs because the catalogue is not complete to $m_V = 21.5$ and preferentially misses low surface brightness

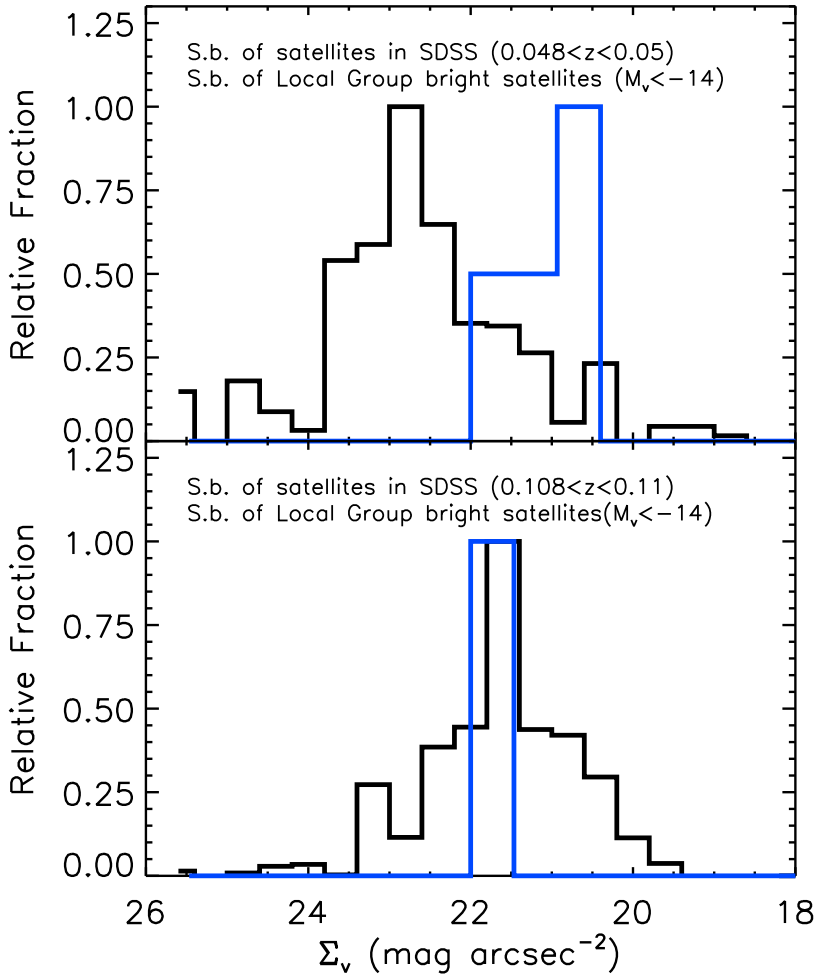

Figure 2.6: A test of surface brightness effects. The black histograms show the distribution of surface brightnesses, defined as the average surface brightness within the half light radius, for potential satellite galaxies around primaries at redshift $z \approx 0.05$ (upper panel) and $z \approx 0.1$ (lower panel). These are compared with the surface brightness distribution (blue histograms) of those bright Local Group satellites which would be brighter than our $m_V = 20.5$ apparent magnitude limit when placed at the redshift of the selected primaries. These equivalent surface brightnesses, computed from the data provided by Mateo (1998), have been k-corrected and redshift-dimmed to the redshift of the selected primaries.

galaxies. With the brighter default cut of $m_V = 20.5$ this effect is greatly reduced (Fig. 2.5j), indicating much higher completeness and little sensitivity to the surface brightness cut. For the r-band catalogue, we perform similar tests and find that cuts at similar values to those found for the V-band are appropriate.

Some of the known Local Group satellites have quite low surface brightnesses (Mateo, 1998) and it is important to check that their counterparts would not be missed in our analysis by falling below the SDSS detection limit. In Fig. 2.6 we plot the distribution of observed surface brightnesses of galaxies around primaries in two different redshift intervals. The turnover in these distributions at around $\Sigma_V \approx 23$ is to be expected given the intrinsic distribution of galaxy surface brightnesses (Driver et al., 2005). The distributions for the SDSS spectroscopic survey only become incomplete around $\Sigma_V \approx 24$ mag arcsec^{-2} (Strauss et al., 2002). The surface brightness distributions of the subset of Local Group satellites whose absolute magnitudes are sufficiently bright for them to be selected in our catalogue are shown by the blue histograms. These can be seen to have surface brightnesses that fall near the middle of the measured distribution.

If the 8 Local Group satellites considered for this study were gradually moved to higher redshifts, then only NGC205 would drop out of our sample by having a surface brightness below $\Sigma_V = 24$ mag arcsec^{-2} before it was lost beneath the flux limit. As our sample also includes the SDSS DR7 photometric subsample, we do actually detect satellites at surface brightnesses below that of NGC205, so a conservative estimate of the incompleteness due to low surface brightness is 1 in 8. M32 is such a centrally concentrated satellite that it would be classified as a star by SDSS, so there is also likely to be a comparably small incompleteness at high surface brightness in our analysis.

These combined results show that our method of estimating the satellite LF is quite robust to changes in the parameter values used in the estimation method. Therefore we will use $\{R_{\rm inner}, R_{\rm outer}, \Delta M_{\rm bin}, \Delta M_{\rm faint}, \Delta z_{\rm s}, \alpha_{\rm p}\}$= $\{0.3$ Mpc, 0.6 Mpc, 0.5, 0.5, 0.002, 2.5$\}$ in the rest of the Chapter.

2.3.1 Estimate of the population variance

Here we describe the method by which we estimate the intrinsic variance in the number of satellites per primary. As illustrated in Fig. 2.7 we are only able directly to count the total number of galaxies,

$$N_{\rm T} = N_{\rm s} + N_{\rm b0}, \tag{2.3.4}$$

where $N_{\rm s}$ is the number of genuine satellites and $N_{\rm b0}$ is the number of contaminating background galaxies in the inner area. These two contributions cannot be measured separately, but we can estimate the mean number of satellites as,

$$\begin{aligned} \langle N_{\rm s} \rangle &= \langle N_{\rm T} \rangle - \langle N_{\rm b0} \rangle & (2.3.5) \\ &= \langle N_{\rm T} \rangle - f \langle N_{\rm out} \rangle, & (2.3.6) \end{aligned}$$

where $N_{\rm out} = N_{\rm b1} + N_{\rm b2} + N_{\rm b3}$ is the total number of background galaxies in the outer area and f is the ratio of the inner to outer areas ($N_{\rm b1}, N_{\rm b2}, N_{\rm b3}$ are the number of background galaxies in three area regions of the outer annulus as illustrated in Fig. 2.7). Below we will take $f = 1/3$ which is the case for our default choice of $R_{\rm outer} = 2R_{\rm inner}$.

Here we are interested in calculating the variance in the number of satellites, $\langle (N_{\rm s} - \langle N_{\rm s} \rangle)^2 \rangle$. Starting with equation (2.3.4) we can write the variance in the total number of galaxies as

$$\begin{aligned} \langle (N_{\rm T} - \langle N_{\rm T} \rangle)^2 \rangle &= \langle (N_{\rm s} + N_{\rm b0} - \langle (N_{\rm s} + N_{\rm b0}) \rangle)^2 \rangle \\ &= \langle (N_{\rm s} - \langle N_{\rm s} \rangle)^2 \rangle + \langle (N_{\rm b0} - \langle N_{\rm b0} \rangle)^2 \rangle \\ &\quad + 2 \langle (N_{\rm s} - \langle N_{\rm s} \rangle)(N_{\rm b0} - \langle N_{\rm b0} \rangle) \rangle. \end{aligned} \tag{2.3.7}$$

If we assume that the number of actual satellites, $N_{\rm s}$, around each primary is uncorrelated with the number of background galaxies, $N_{\rm b0}$, the final cross term vanishes to leave

$$\langle (N_{\rm s} - \langle N_{\rm s} \rangle)^2 \rangle = \langle (N_{\rm T} - \langle N_{\rm T} \rangle)^2 \rangle - \langle (N_{\rm b0} - \langle N_{\rm b0} \rangle)^2 \rangle. \tag{2.3.8}$$

The term, $\langle (N_{\rm b0} - \langle N_{\rm b0} \rangle)^2 \rangle$ cannot be directly measured, but, to a good approximation, we would expect it to equal the variances, $\langle (N_{{\rm b}i} - \langle N_{{\rm b}i} \rangle)^2 \rangle$, of each of

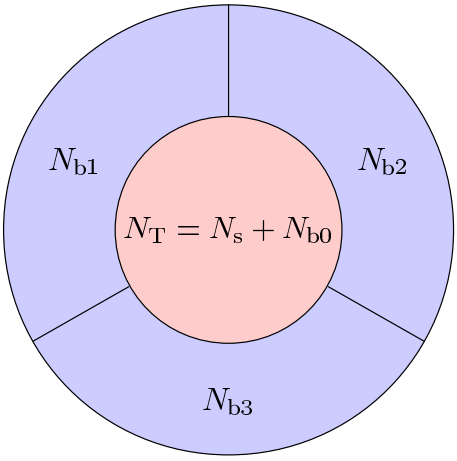

Figure 2.7: Schematic of the definition of quantities used in the estimation of the population variance. The number of genuine satellites is $N_{\rm s}$ and the number of contaminating background galaxies in the inner area is $N_{\rm b0}$; the number of background galaxies in three equal area regions of the outer annulus are $\langle N_{{\rm b}i} \rangle$, with $i = 1, 2$ or 3.

the equal area portions of the outer annulus. Hence, our final estimate of the variance in the number of genuine satellites per primary can be written as

$$\langle (N_{\rm s} - \langle N_{\rm s} \rangle)^2 \rangle = \langle (N_{\rm T} - \langle N_{\rm T} \rangle)^2 \rangle - \frac{1}{3} \sum_{i=1}^{3} \langle (N_{{\rm b}i} - \langle N_{{\rm b}i} \rangle)^2 \rangle. \tag{2.3.9}$$

For a given selection of primaries and choice of satellite absolute magnitude, these terms will depend on the redshift of the primary. We find a smooth variation with redshift bin and weight the variances according to the contribution each redshift makes to the overall estimate of the satellite luminosity function to estimate the overall variance on the luminosity function. The result is shown in Fig. 2.9.

2.4 Results

We now explore the dependence of the satellite LF on the properties of the primary galaxies. Estimates of the V and r-band satellite LF for primaries of magnitude $M_{\rm c} = -21, -22$ and -23 are shown in Fig. 2.8. As the luminosity of the primary increases the number of satellites increases at all values of ΔM,

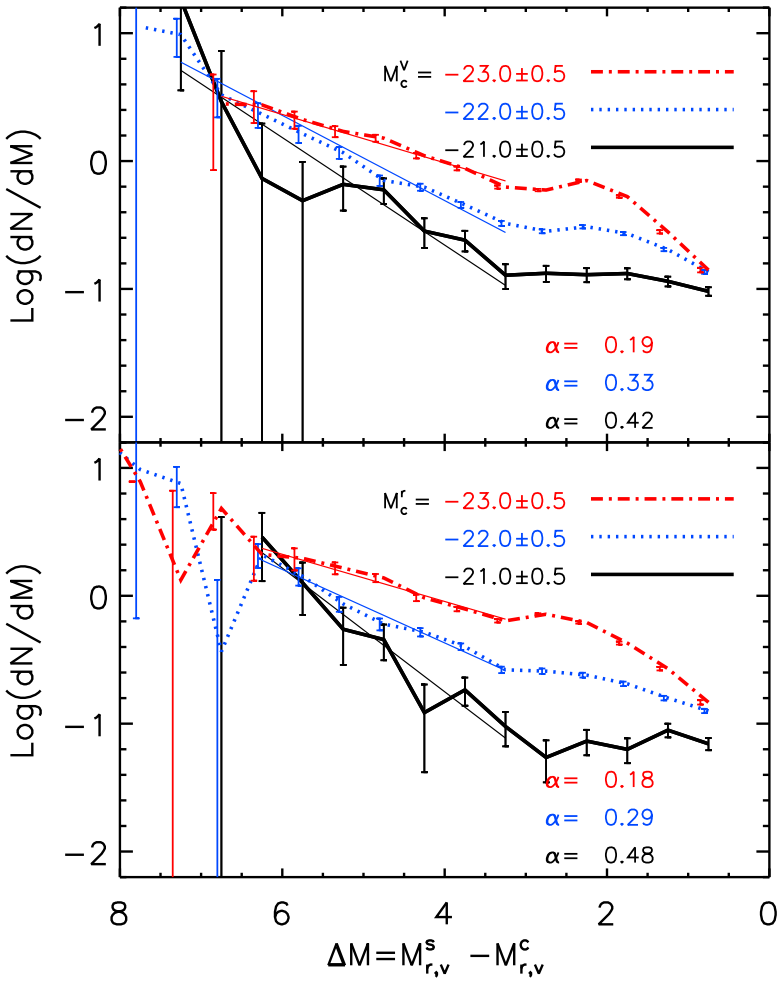

Figure 2.8: The estimated satellite LFs for different bins of primary magnitude as indicated in the legend. The top panel is for the V-band and the bottom panel for the r-band. The straight lines show power-law fits to the faint ends of the luminosity functions. Their slopes, α, are given in the legend. Here, the selection parameters, $\{R_{\rm inner}, R_{\rm outer}, \Delta M_{\rm bin}, \Delta M_{\rm faint}, \Delta z_{\rm s}, \alpha_{\rm p}\}$, are set to the default values { 0.3 Mpc, 0.6 Mpc, 0.5, 0.5, 0.002, 2.5}

.

and, in addition, the shape of the LF changes. None of the luminosity functions are well fit by Schechter functions, i.e. they are not well described by power laws with exponential cutoffs at the bright end. Instead, there is a tendency for the LFs to become flatter at the bright end and the satellite LFs of the brightest primaries even have a local maximum at $\Delta M = 2$. Only at the faint end are the luminosity functions accurately represented by power laws. We show such fits and list their slopes in Fig. 2.8 . The variety of features in the LFs suggests they will place interesting constraints on galaxy formation models.

In Fig. 2.9, we carry out a comparison of the satellite LF of primaries of similar luminosity to the MW and M31 with data for these two galaxies. The average satellite LF of the MW and M31 has often been compared to theoretical models (e.g. Benson et al., 2002; Somerville, 2002) and used to constrain properties of the model such as the redshift of reionization and the strength of supernova feedback. In so doing one implicitly assumes that the satellite LF per primary galaxy of the combined MW+M31 system is typical of isolated galaxies of similar luminosity. The data allow a direct test of this assumption at the bright end, $M_{\rm V} < -14$, of the LF. For this comparison, we assume that the V-band magnitudes of both the MW and M31 lie in the range -21.25 ± 0.5 (Flynn et al., 2006; Gil de Paz et al., 2007) and compare directly with the average of their V-band LFs by plotting on the x-axis the V-band $\Delta M + M_{\rm c}$. Over the range $-14 > M_{\rm V} > -19$ our mean LF has a very similar slope to that of the average of the MW and M31, but with almost a factor two fewer satellites at all luminosities. Fainter than $M_{\rm V} = -14$ our estimate becomes noisy due to a lack of nearby primaries. The random errors on our estimate of the mean luminosity density are small at bright magnitudes, yielding a well-defined estimate of the luminosity function that provides a very strong constraint on models all the way to magnitudes as bright as $M_{\rm V} = -20$. Comparison with the theoretical models of Benson et al. (2002) and Somerville (2002) highlights the range of predictions. Tuning the models to match our new data rather than just the MW or M31 may lead to a different assessment of the strength of feedback effects in suppressing the formation of satellite galaxies. This is particularly apparent when one con-

siders the system-to-system variation in the satellite LF. We have estimated the intrinsic rms scatter about the mean LF using the method detailed in the Section 2.3.1. We indicate this range with the blue error bars on the cumulative LF in the lower panel of Fig. 2.9 and the mean plus the rms of the differential LF by the blue dashed line in the upper panel. Since even in the cumulative LF, the mean number of satellites per primary is low it is inevitable that the width of the distribution includes zero satellites. The wide scatter illustrates the danger of just using the MW+M31 to constrain models.

It is also interesting to see how the satellite luminosity function depends on the colour and morphology of the primary galaxy. Fig. 2.10 shows the resulting satellite LFs when primaries of V-band magnitude -21.25 ± 0.5 are split by colour and by concentration. In the upper panel we divide the primary galaxies into "red" and "blue" subsamples according to the well-known colour bimodality in the colour-magnitude plane (e.g. Strateva et al., 2001; Baldry et al., 2004; Zehavi et al., 2005). Following Zehavi et al. (2005), we use an equivalent colour criterion of ${}^{0.0}(g-r)_{\rm cut} = 0.19 - 0.24M_r$ (not identical to Zehavi et al. as our magnitudes are K-corrected to $z = 0.0$ rather than $z = 0.1$). We see that in this bright satellite regime, the LF around blue primaries is lower than the LF around red primaries. This difference might simply reflect the relative mass of the halos. Assuming stellar mass to correlate with halo mass we would expect that at a fixed V-band magnitude blue star forming galaxies would be less massive than their red counterparts.

The lower panel splits the sample into early and late type where the early type is defined as having a concentration index $c \geq 2.6$. This division roughly separates early-type (E/S0) galaxies from late-type (Sa/b/c, Irr) galaxies (Shimasaku et al., 2001). We see that the satellite LF of late types is suppressed with respect to that of the early types. Given the well known correlation between colour and morphology this result is consistent with the division by colour.

We can also use the colour information available in SDSS to probe the properties of the satellites. For two bins of V-band primary magnitude, Fig. 2.11 shows their satellite luminosity functions split into red and blue subsamples us-

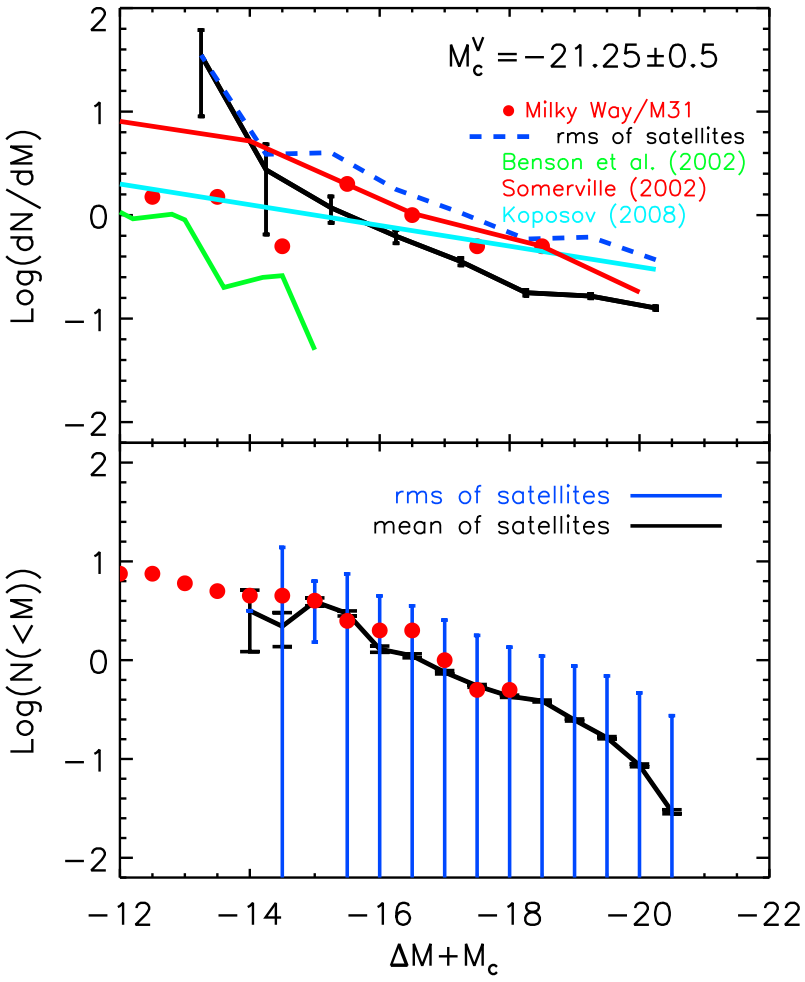

Figure 2.9: A comparison of the average satellite LF in our sample with the satellite LF of the Milky Way and M31. The upper panel shows the differential satellite LF of MW-like galaxies. The solid line with error bars shows the estimated V-band satellite LF of primaries with similar magnitudes to the Milky-Way and M31 ($M_c = -21.25 \pm 0.5$ in the V-band). This is compared to the mean LF of the MW and M31 (per central galaxy) in unit magnitude bins shown by the red points. (Continued on the following page.)

Figure 2.9: (continued) The best fit power law, $dN/dM_v = 10 \times 10^{0.1(M_v+5)}$, of Koposov et al. (2008) is shown as the cyan line. The theoretical predictions of Benson et al. (2002) and Somerville (2002) for $z_{\rm reion} = 10$ are shown by the green and red lines respectively. The blue dashed line labelled "rms of satellites" shows the mean value plus the rms of the LF among different primaries. The lower panel shows the same results and the observational data in cumulative form. Here, the black error bars give the error on the mean cumulative LF while the much broader blue error bars indicate the intrinsic rms scatter about this mean.

ing the same cut in the colour magnitude plane as before. We see that at all but the brightest magnitudes the satellites are predominately blue and star forming. This is in stark contrast with the satellites in groups and clusters where the brightest tend to be red and dead while the faintest are blue (Skibba & Sheth, 2009). We also note that the LF of the red satellites is far from a power law. It has a distinct dip in the range from $3.0 < \Delta M < 5.0$ and, for the brighter primaries, the peak $\Delta M \approx 2.0$ that we noted earlier in the total LFs is clearly present in the red subsample (and also in the blue subsample).

2.5 Discussion

We have constructed a large sample of isolated primary galaxies and their fainter neighbours using both the SDSS DR7 spectroscopic and photometric galaxy catalogues. The samples are sufficiently large that we are able to stack the systems and accurately subtract the local background to estimate the mean satellite luminosity function (LF) and its dependence on the luminosity, colour and morphology (optical concentration) of the primary. Our main conclusions are:

1. The satellite LF is well determined over a range extending to approximately 8 magnitudes fainter than the primary, for primaries with V magnitudes in the range -20 to -23.

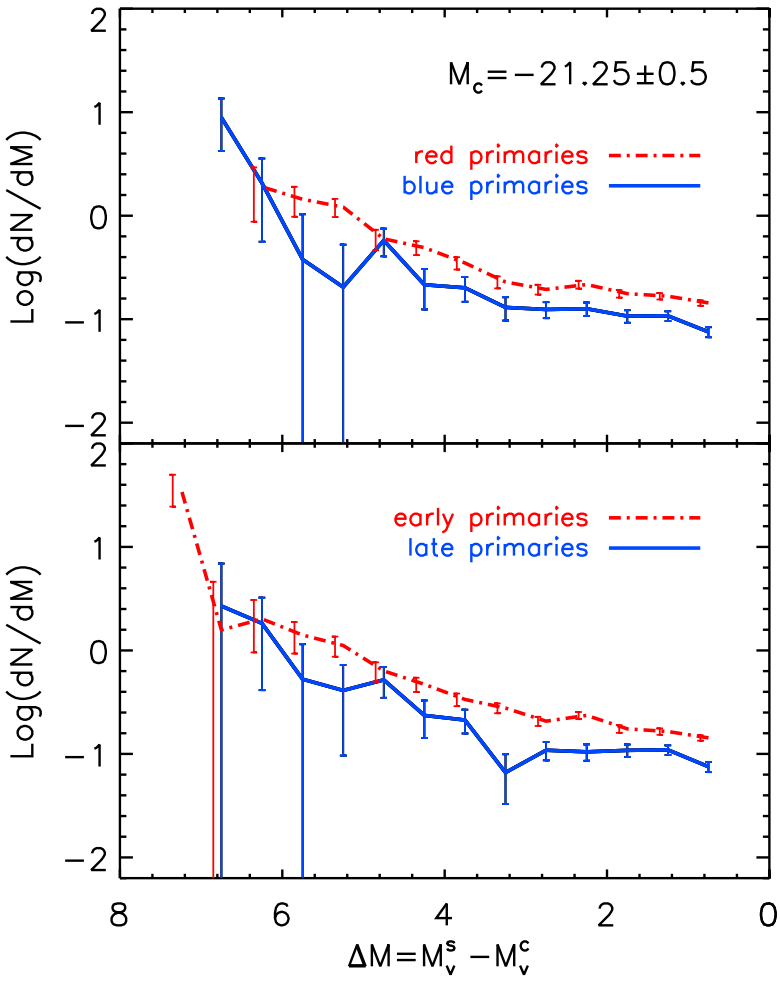

Figure 2.10: The mean satellite LF of different colours (top panel) and types (bottom panel) of primary galaxy. The satellite LF of early-type or red primary galaxies is shown as a red (dot-dashed) line and that of late-type or blue is plotted as a blue (solid) line.

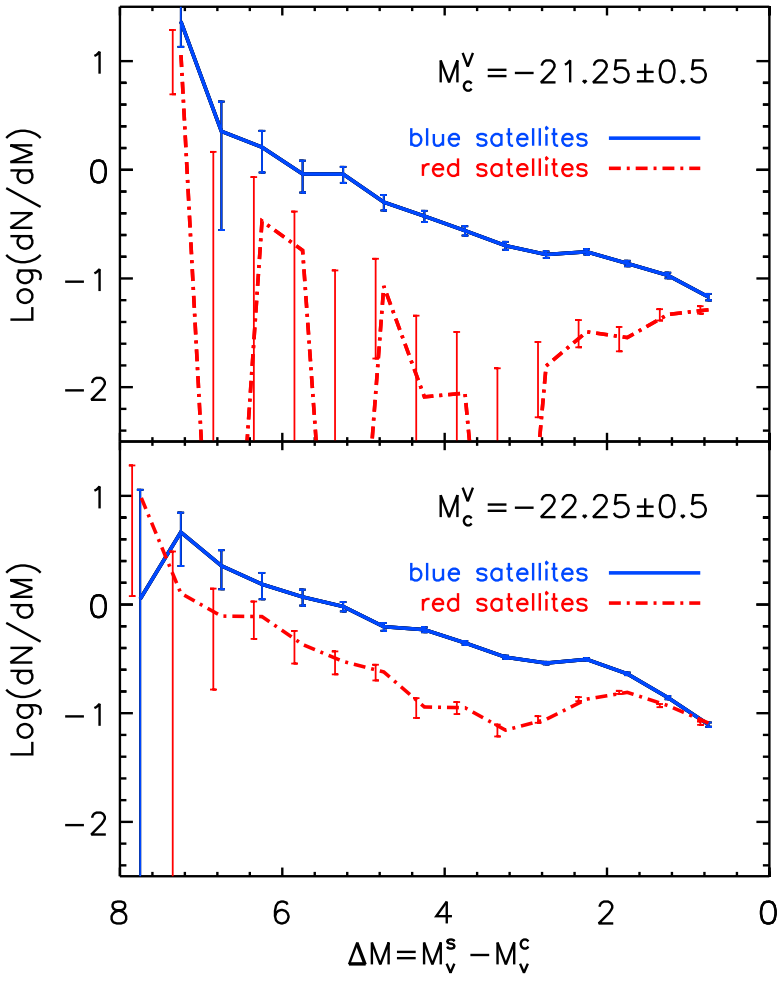

Figure 2.11: The satellite LF split into contributions from "blue" and "red" satellites. The top and bottom panels show the results for primaries of V-band magnitude $M_c = -21.25$ and -22.25 respectively. The "blue" and "red" satellite LFs are plotted as blue (solid) and red (dot-dashed) lines respectively.

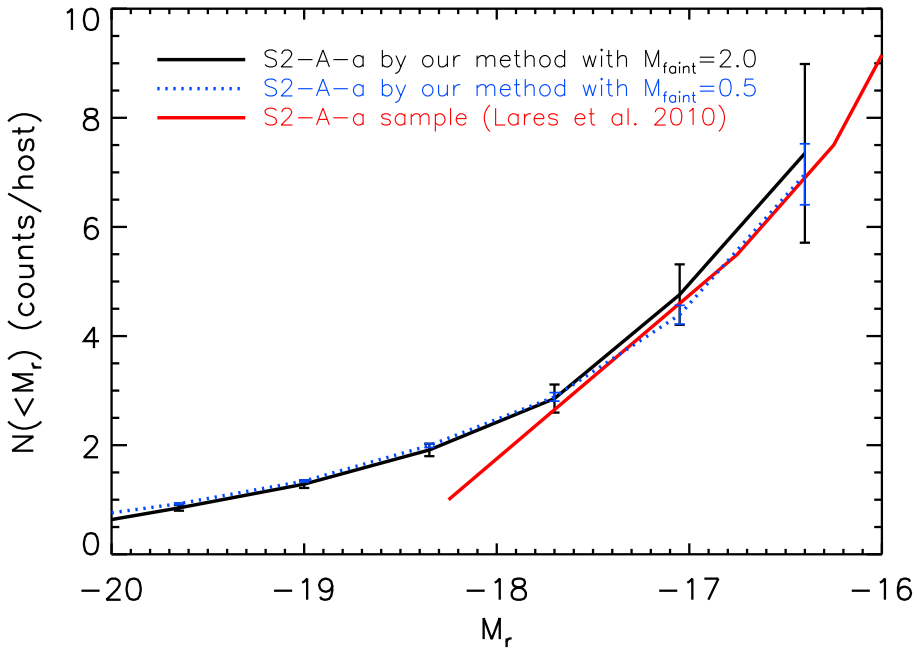

Figure 2.12: The red line shows the satellite LF estimated by (Lares et al., 2011) for their S0-A-a subsample. The solid black and dotted blue lines show our result for a similar sample primary galaxies, those brighter than -21.5 in r-band and in the redshift range $0.03 < z < 0.1$, using $\Delta M_{\rm faint} = 2.0$ and 0.5 respectively.

2. The satellite LF does not have a Schechter form. After a steep decline at the faintest magnitudes, the LF roughly follows a fairly flat power law but there is a bump at relative magnitude $\Delta M \simeq 2$ which is particularly significant for brighter primaries (see Fig. 2.8).

3. Over the range $-14 > M_V > -19$, the mean satellite LF around primaries of $M_V = -21.25$ has a similar slope, but about a factor of two lower amplitude than the average of the combined MW and M31 LFs (see Fig. 2.9).

4. The amplitude of the satellite LF increases with the luminosity of the primary. Over most of the range sampled, the increase is approximately a factor of 2 per primary V magnitude, but there are significant variations in the shape of the function for primaries of different luminosity (see Fig. 2.8).

5. The amplitude of the satellite LF also varies with the colour and the morphological type of the primary. Red primaries have more satellites than blue primaries and early-type primaries have more satellites that late-type primaries (see Fig. 2.10).

6. Except for the brightest objects, satellite galaxies are predominantly blue and star-forming (see Fig. 2.11).

As we were completing this work two related studies were published, both using the SDSS DR7. Liu et al. (2011) used similar selection criteria to ours to construct a sample of Milky Way-like primaries and deconvolved for the variation of the background to determine the frequency at which these Milky-Way like systems host satellites as bright as the SMC and LMC. They find that 11.6% host one such satellite and only 3.5% host two. And they find a mean of 0.29 satellites per primary. This is in excellent agreement with the mean of 0.30 that we find for satellites between 2 and 4 magnitudes (the range used by Liu et al.) fainter than primaries with the magnitude, $M_V = -20.9$, adopted by Liu et al. For the fiducial "Milky Way" luminosity we have adopted here, $M_V = -21.25 \pm 0.5$, we find a slighly larger mean of 0.47 Magellanic cloud type satellites per primary.

In a separate study, Lares et al. (2011) estimated cumulative satellite luminosity functions and radial density profiles of satellite systems around primaries brighter than $M_r = -20.5$. When we reproduce the selection criteria of one of their samples using our catalogue, we find excellent agreement for satellite magnitudes fainter than $M_r = -18.5$, but at brighter magnitudes we find a significant excess compared to their estimate (see Fig. 2.12). This excess is robust to changes in the value of the isolation parameter, $\Delta M_{\rm faint}$, that we have used.

The satellite LF probes the smallest scales visible today in the hierarchy of galaxy formation. This statistic provides a strong test of the ΛCDM cosmological model, which robustly predicts the number of subhalos that could host satellite galaxies, and a test of galaxy formation theory, which determines which of these subhalos are populated by visible satellites. The results so far are encouraging. For example, the original ΛCDM galaxy formation model of Benson et al. (2002) (which predicted the population of ultrafaint satellites subsequently discovered in the SDSS), as well as the more recent model of Guo et al. (2011) predict that bright satellites like the LMC and the SMC should be rare. This feature appeared to be a shortcoming of the model when data were available only for the MW (Koposov et al., 2008). The new results for large samples of MW-like galaxies by Liu et al. (2011) and ourselves now suggest that the MW is unusual in having such bright satellites.

According to standard theory, the satellite LF is established by processes that regulate star formation in small halos, namely photoionization of the gas at high redshift and supernova feedback, acting on a population of dark matter subhalos, itself the result of dynamical evolution from a spectrum of primoridal ΛCDM density perturbations. Our analysis and those by Liu et al. (2011) and Lares et al. (2011) reveal features in the satellite LF and systematic trends with the properties of the central galaxies. These properties encode information about galaxy formation processes that will help develop increasingly refined theoretical models.

3

PROJECTED NUMBER DENSITY PROFILES FOR PRIMARIES IN SDSS

In this chapter, we study the spatial distribution of satellite galaxies around isolated primaries using the Sloan Digital Sky Survey (SDSS) spectroscopic and photometric galaxy catalogues. We select isolated primaries from the spectroscopic sample and search for potential satellites in the much deeper photometric sample. For specific luminosity primaries we obtain robust statistical results by stacking as many as $\sim 50,000$ galaxy systems. We find no evidence for any anisotropy in the satellite galaxy distribution relative to the major axes of the primaries. We derive accurate projected number density profiles of satellites down to 4 magnitudes fainter than their primaries. We find the normalized satellite profiles generally have a universal form and can be well fitted by projected NFW profiles. The NFW concentration parameter increases with decreasing satellite luminosity while being independent of the luminosity of the primary except for very bright primaries. The profiles of the faintest satellites show deviations from the NFW form with an excess at small galactocentric projected distances. In addition, we quantify how the radial distribution of satellites depends on the colour of the satellites and on the colour and concentration of their primaries.

3.1 Introduction

In this Chapter, for the same primary and satellite samples we explored in Chapter 2, we are now interested in the average spatial profile of the distribution of

these satellites around their primaries. These density profiles are an important tracer of the distribution of substructures in the primary halo and can provide us with useful information to test current models of the formation and evolution of dark matter haloes. In addition, we are not only interested in the projected number density profile of satellites around isolated primary galaxies binned by luminosity, colour and morphology, but also on the dependence of the profiles on the properties of the satellites themselves. To this end, we select our primary samples from the SDSS DR8 spectroscopic sample ($\sim$ 660 000 galaxies) and satellite candidates from the photometric samples ($\sim$ 96 000 000 galaxies) with the same criteria as in Chapter 2 to build significantly large samples. We restrict the photometric sample to galaxies brighter than $m_r = 20.5$ as in Chapter 2 (Section 4) to ensure completeness. Based on these large samples, we explore the dependence of the density profiles on the properties of primaries and satellites.

The remainder of this chapter is organised as follows. In Section 3.2.1, we briefly describe the selection of primary galaxies and their satellites; in Section 3.2.2, we develop a method for estimating the projected satellite number density profile; in Section 3.3, we present our estimate of the projected satellite number density for different primary samples. We conclude, in Section 3.4, with a summary and discussion of our results. Throughout the Chapter we assume a fiducial ΛCDM cosmological model with $\Omega_M = 0.3$, $\Omega_\Lambda = 0.7$ and $H_0 = 70$ km s^{-1} Mpc^{-1}.

3.2 Sample and Method

3.2.1 Data and sample selection

We have built two separate catalogues similar to those in Chapter 2. The smaller one is of galaxies from the main SDSS spectroscopic catalogue from which we select our primary galaxies (hereafter the spectroscopic catalogue). The larger one is of galaxies with photometric redshifts and magnitudes from which we select the neighbouring galaxies (hereafter the photometric catalogue). The spec-

troscopic catalogue is constructed from the SDSS DR8 spectroscopic subsample (north galactic cap) including all objects with high quality redshifts (zconf > 0.7 and specClass $= 2$) and a Petrosian magnitude $r \leq 17.77$. The photometric galaxy catalogue is from the SDSS DR8 photometric subsample (north galactic cap) and includes only objects that have photometric redshifts, none of the flags BRIGHT, SATURATED, or SATUR_CENTER [1] set and model magnitudes $r \leq 22.0$. We select only objects with corresponding entries in the SDSS database PhotoZ table, which naturally selects galaxies and excludes stars[2]. As galaxies with $r \leq 17.77$ are included in both SDSS catalogues, a small fraction of the photometric catalogue galaxies also have spectroscopic redshifts. We use dereddened model *ugriz* magnitudes and *k*-correct all galaxies to $z = 0$ with the IDL code of Blanton & Roweis (2007). We estimate V-band magnitudes from g and r-band magnitudes assuming $V = g - 0.55(g - r) - 0.03$ (Smith et al., 2002) and all our sample selection and magnitude cuts are performed using this V-band magnitude.

Our sample of isolated primary galaxies is chosen using the same criteria as in Chapter 2, illustrated in Fig. 3.1. We select primary galaxy candidates of absolute magnitude, $M_{\rm p}$, in the range $M_{\rm C} - \Delta M_{\rm bin} < M_{\rm p} \leq M_{\rm C} + \Delta M_{\rm bin}$. We then filter these primary candidates, using a series of criteria summarised in figure 2.1 of Chapter 2, to guarantee that a) there are no luminous neighbouring galaxies projected within $2R_{\rm inner}$ of the primary, unless these luminous neighbours are sufficiently separated in redshift from the primary and appear here due to a chance projection; b) the satellite search areas (projected distance $R_{\rm inner}$ from the primary) around each primary do not overlap with each other. Further details of the generation of the two samples are may be found in Chap-

[1]When applying our isolation criteria to reject primaries with bright neighbours we use a source catalogue that also includes objects for which SATURATED and/or SATUR_CENTER flags are set. These objects are mainly stars and we prefer to reject systems contaminated by bright stars as the presence of such unmasked stars could effect the efficiency with which background galaxies are detected.

[2]The photo-z were only applied to objects which are classified as galaxies

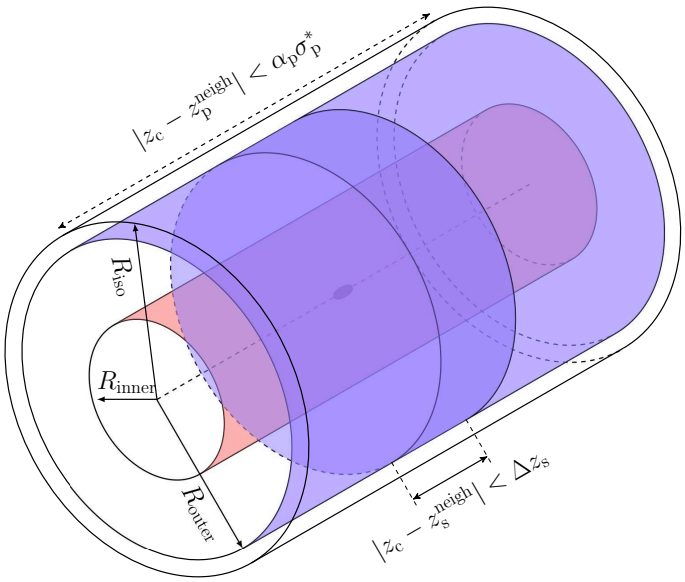

Figure 3.1: Schematic diagram of the sample selection procedure. For each acceptable primary, there should be no neighbouring, sufficiently bright, galaxies within a cylinder of radius $R_{\rm iso}$, centred on the primary, and nearby in redshift space. As defined in Fig. 1 in Chapter 2, nearby means either $|z_{\rm c} - z_{\rm s}^{\rm neigh}| < \Delta z_{\rm s}$, where $\Delta z_{\rm s}$ is the maximum allowed spectroscopic redshift difference between a primary (c) and another galaxy (s), or $|z_{\rm c} - z_{\rm p}^{\rm neigh}| < \alpha_{\rm p}\sigma_{\rm p}^*$, where $\sigma_{\rm p}$ is the measurement error of the photometric redshift and $\alpha_{\rm p}$ is the tolerance of the error, for galaxies that have no spectroscopic redshift. Satellites will lie nearby in redshift space and within the cylinder of radius $R_{\rm inner}$ (red), whereas the local background to be subtracted is determined from the volume between this inner cylinder and the outer one with radius $R_{\rm outer}$.

ter 2. The values of the selection parameters, $\{\Delta M_{\rm bin}, \Delta M_{\rm faint}, \Delta z_{\rm s}, \alpha_{\rm p}, m_{\rm v}^{\rm lim}\} = \{0.5, 0.5, 0.002, 2.5, 20.5\}$, are the same as the default values in Chapter 2. Here $\Delta M_{\rm bin}$ is the half-width of the primary magnitude $M_{\rm c}$ bin, $\Delta M_{\rm faint}$ is the magnitude difference between the primaries and satellites used to isolate primaries, $\Delta z_{\rm s}$ and $\alpha_{\rm p}$ are the parameters used to exclude galaxies that are at a significantly different spectroscopic redshift and photometric redshift respectively. The meaning of these parameters is explained in Fig. 3.1 (see section 2 of Chapter 2 for more details). One small change relative to Chapter 2 is that $R_{\rm inner}$ is chosen to increase with increasing primary luminosity, in order to ensure that no satellites are missed for the most luminous primaries.

3.2.2 Estimating the projected satellite number density profile

Once our primary galaxies are defined, their potential satellites are found from the photometric galaxy catalogue as depicted in Fig. 3.2. The method we use is similar to that in Chapter 2, except that for each primary, the number of galaxies is counted and binned by their projected radial distances from the primary, $N(r_j^{\rm ann})$, as well as by their luminosity. That is, for the ith primary galaxy, the number of inner galaxies in each annulus, $N_i^{\rm inner}(r_j^{\rm ann})$, is found by counting all the neighbouring galaxies within the annulus of radius $r_j^{\rm ann}$ that satisfy the following conditions: at least $\Delta M_{\rm faint}$ fainter than the primary; if they have a spectroscopic redshift, $z_{\rm s}$, then they should satisfy $|z_{\rm c} - z_{\rm s}| < \Delta z_{\rm s}$; or if they only have a photometric redshift $z_{\rm p}$, then they should satisfy $|z_{\rm c} - z_{\rm p}| < \alpha_{\rm p}\sigma_{\rm p}^*$, where $\sigma_{\rm p}^*$ is the error in the photometric redshift as defined in Chapter 2. The number of outer galaxies, $N_i^{\rm outer}$, is determined by applying the same conditions to galaxies in the outer area between $R_{\rm inner}$ and $R_{\rm outer}$. Assuming, for now, that few genuine satellites will be projected beyond $R_{\rm inner}$ we can estimate the surface density of genuine satellites in each annulus as

$$\Sigma_i^{\rm sat}(r_j^{\rm ann}) = \frac{N_i^{\rm inner}(r_j^{\rm ann})}{A_i^{\rm inner}} - \frac{N_i^{\rm outer}}{A_i^{\rm outer}}, \tag{3.2.1}$$

where $A_i^{\rm inner}$ and $A_i^{\rm outer}$ are the areas of the inner annulus and outer region respectively. If necessary, we take account of the sky coverage of SDSS DR8 by

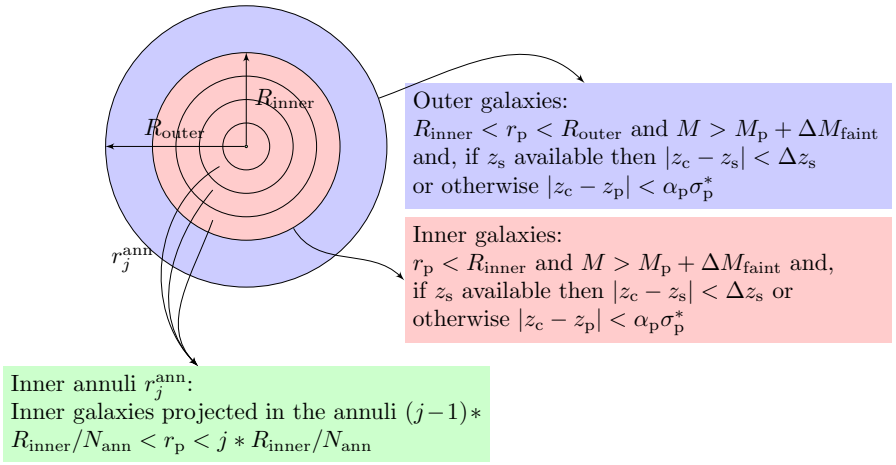

Figure 3.2: Schematic showing the selection of potential satellite galaxies in annuli of radii $r_j^{\rm ann}$ within $R_{\rm inner}$ and a reference sample bounded by the radii $R_{\rm inner} < r < R_{\rm outer}$, used to subtract the residual contaminating background. For both samples we apply the stated redshift cuts to reduce background contamination. We also apply the stated absolute magnitude cut to both samples (assuming the neighbouring galaxies are at the same redshift as the primary) though this cut is redundant unless $R_{\rm outer} > 2R_{\rm inner}$ as otherwise the existence of such bright neighbouring galaxies would automatically lead to the exclusion of the primary galaxy.

reducing the areas $A_i^{\rm inner}$ and $A_i^{\rm outer}$ by the amounts defined by the DR7 mask described in Norberg et al. (2011).

Because of the apparent magnitude limit of SDSS, which we take to be $m^{\rm lim} = 20.5$, we count the faintest satellites only at low redshift and are progressively limited to more and more luminous satellites with increasing redshift. To account for this and construct an unbiased estimate of the projected satellite number density profile over all primary galaxies, we accumulate the area contributed by the ith primary to the jth annulus for the detection of satellites brighter than $M_{\rm sat}^{\rm trun}$,

$$A_{ij}^{\rm p}(M_{\rm sat}^{\rm trun}) = \begin{cases} A_{ij} & M_{\rm sat}^{\rm trun} < M_i^{\rm lim} \\ 0 & M_{\rm sat}^{\rm trun} > M_i^{\rm lim} \, . \end{cases} \tag{3.2.2}$$

Here A_{ij} is the unmasked area of the jth annulus surrounding the ith primary and $M_i^{\rm lim}$ is the absolute magnitude that corresponds to the apparent magnitude limit, $m^{\rm lim}$, of the SDSS photometric catalogue at the redshift of the primary, $M_i^{\rm lim} = m^{\rm lim} - 5\log_{10}(D_i^L) - K(z_i)$, where D_i^L and $K(z_i)$ are the corresponding luminosity distance and k-correction. This contributing area is set to zero if any potential satellites within the magnitude bin are too faint to be included, in which case we exclude this primary and its satellites as its contribution to the mean projected satellite number density profile would be incomplete. We further define $N_{ij}^{\rm sat}(M_{\rm sat}^{\rm trun})$ to be the number of detected potential satellites brighter than $M_{\rm sat}^{\rm trun}$ in the jth annulus surrounding the ith primary and $N_i^{\rm bck}(M_{\rm sat}^{\rm trun})$ to be the corresponding number of detected galaxies in the outer annulus, $R_{\rm inner} < r < R_{\rm outer}$, whose unmasked area is $A_i^{\rm outer}$. Hence we can express the mean surface density of satellite galaxies brighter than $M_{\rm sat}^{\rm trun}$ in the jth annulus as

$$\widetilde{\Sigma}^{\rm sat}(r_j^{\rm ann}, M_{\rm sat}^{\rm trun}) = \frac{\sum_i N_{ij}^{\rm sat}(M_{\rm sat}^{\rm trun})}{\sum_i A_{ij}} - \frac{\sum_i N_i^{\rm bck}}{\sum_i A_i^{\rm outer}}. \tag{3.2.3}$$

In practice, we divide the projected radial distance from the primary into 20 bins ($j = 1, 2, \cdots, 20$). Because of a concern that the SDSS data reduction pipeline may occasionally misclassifies fragments of the spiral arms of bright galaxies as separate galaxies we exclude individual annuli that are within 1.5 times the Petrosian radius, R_{90}, of the primary galaxy. We set our magnitude

limit, $M_{\rm sat}^{\rm trun}$, either by absolute value, such as $-20, -19, -18$, or by magnitude relative to the corresponding primary, $M_{\rm sat}^{\rm trun} = M_{\rm p} + 1.0, 2.0, 3.0$. We present results using both thresholds so that we can determine whether the number density profiles depend on the absolute luminosity of satellites or on the relative luminosity between satellites and their primaries.

The process of estimating the projected satellite number density profiles is quite similar to estimating the satellite luminosity functions in Chapter 2. We divide our primaries into three luminosity bins centred on $M_{\rm c} = -21.25, -22.0, -23.0$. The choice of the parameters $R_{\rm inner}$ and $R_{\rm outer}$ is a balance between making them sufficiently large to avoid severely truncating the density profiles and making them too large such that our sample shrinks due to the selection process excluding overlapping systems. A sensible choice is to set $R_{\rm inner}$ to exceed the anticipated size of the satellite system, r_{200}[3], and $R_{\rm outer}$ to be roughly a factor of two larger so as to get a good, but still local, estimate of the background density. Here we have adopted the following values of $(R_{\rm inner}, R_{\rm outer})$, $(0.3, 0.6)$, $(0.4, 0.8)$ and $(0.55, 0.9)$ Mpc for primaries in magnitude bins, $M_{\rm c} = -21.25, -22.0$ and -23.0, respectively. The values of $R_{\rm inner}$ have been compared with the mean of the estimated r_{200} values for each galaxy in the chosen magnitude bin (see Section 3) and are found all to be larger, suggesting that the search radii for the different primary magnitude bins are sufficiently large to capture all satellites. Additional reassurance is provided by the tests in Section 3.2.4, which show that the profiles are insensitive to changes in the values of $R_{\rm inner}$ or $R_{\rm outer}$.

3.2.3 The Projected NFW Profile with background subtraction

The NFW density profile (Navarro et al., 1996, 1997) is

$$\rho(r) = \frac{\delta_{\rm c}\rho_{\rm c}}{(r/r_{\rm s})(1 + r/r_{\rm s})^2}, \tag{3.2.4}$$

where $\rho_{\rm c}$ is the critical density, $\delta_{\rm c}$ is the characteristic overdensity of the halo and $r_{\rm s}$ is a characteristic scale length. Conventionally, the scale length is specified in

[3]Here r_{200} depicts the radius at which the mean interior density is 200 times the cosmological critical density.

terms of a concentration defined as $c = r_{200}/r_{\rm s}$, where the r_{200} radius is defined as the radius at which the mean interior density is $200\rho_{\rm c}$. With these definitions it follows that

$$\delta_c = \frac{200}{3}\frac{c^3}{\ln(1+c) - c/(1+c)}. \tag{3.2.5}$$

We can integrate along a line of sight to obtain the projected surface mass density

$$\Sigma(R) = 2\delta_{\rm c}\rho_{\rm c} r_{\rm s} \int_R^\infty \frac{1}{\sqrt{r^2 - R^2}\,(r/r_{\rm s})\,(1 + r/r_{\rm s})^2}{\rm d}r, \tag{3.2.6}$$

where R is the projected distance from the centre of the halo. This integral can be solved analytically (Bartelmann, 1996) and expressed as

$$\Sigma(x) = \begin{cases} \dfrac{2\delta_{\rm c}\rho_{\rm c} r_{\rm s}}{(x^2-1)}\left[1 - \dfrac{2}{\sqrt{(1-x^2)}}\operatorname{arctanh}\sqrt{\dfrac{1-x}{1+x}}\right] & \\ & x < 1, \\ \dfrac{2\delta_{\rm c}\rho_{\rm c} r_{\rm s}}{3} & x = 1, \\ \dfrac{2\delta_{\rm c}\rho_{\rm c} r_{\rm s}}{(1-x^2)}\left[1 - \dfrac{2}{\sqrt{(x^2-1)}}\arctan\sqrt{\dfrac{x-1}{1+x}}\right] & \\ & x > 1, \end{cases} \tag{3.2.7}$$

where $x = R/r_s$. In our profile measurements, we remove the contamination of interlopers by subtracting the mean density of galaxies in an outer annulus. This outer annulus will also contain genuine satellites that are in the outer annulus of the density profile. Hence, to compare fairly with the measured profiles, we should apply the same background subtraction process to the projected NFW profile. We denote the resulting background-subtracted projected NFW profile as

$$\hat{\Sigma}(x) = \Sigma(x) - \frac{2r_s^2}{3r_{200}^2}\int_{x_{200}}^{2x_{200}} \Sigma(x)\, x\, {\rm d}x. \tag{3.2.8}$$

These background-subtracted profiles are compared to their unsubtracted counterparts in Fig. 3.3. The subtracted profiles tend to zero at projected $R/r_{200} \sim 1.4$.

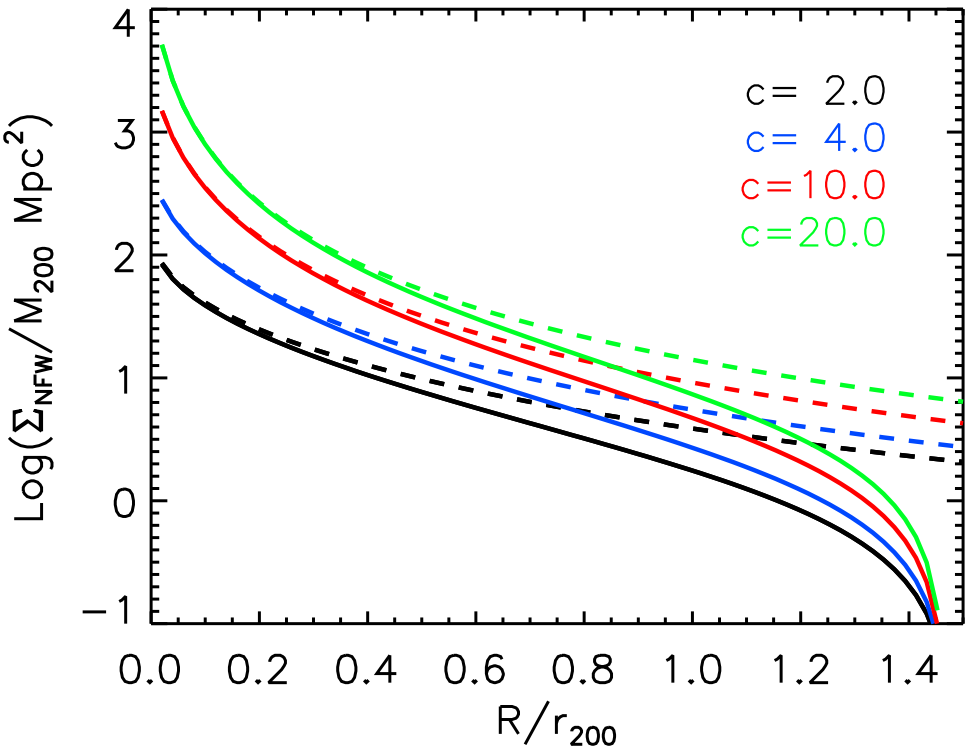

Figure 3.3: A comparison of projected NFW profiles (dashed lines) and background-subtracted projected NFW profiles (solid lines) for different values of the concentration, c. The projected radius, R, is expressed in units of the r_{200} radius, r_{200}.

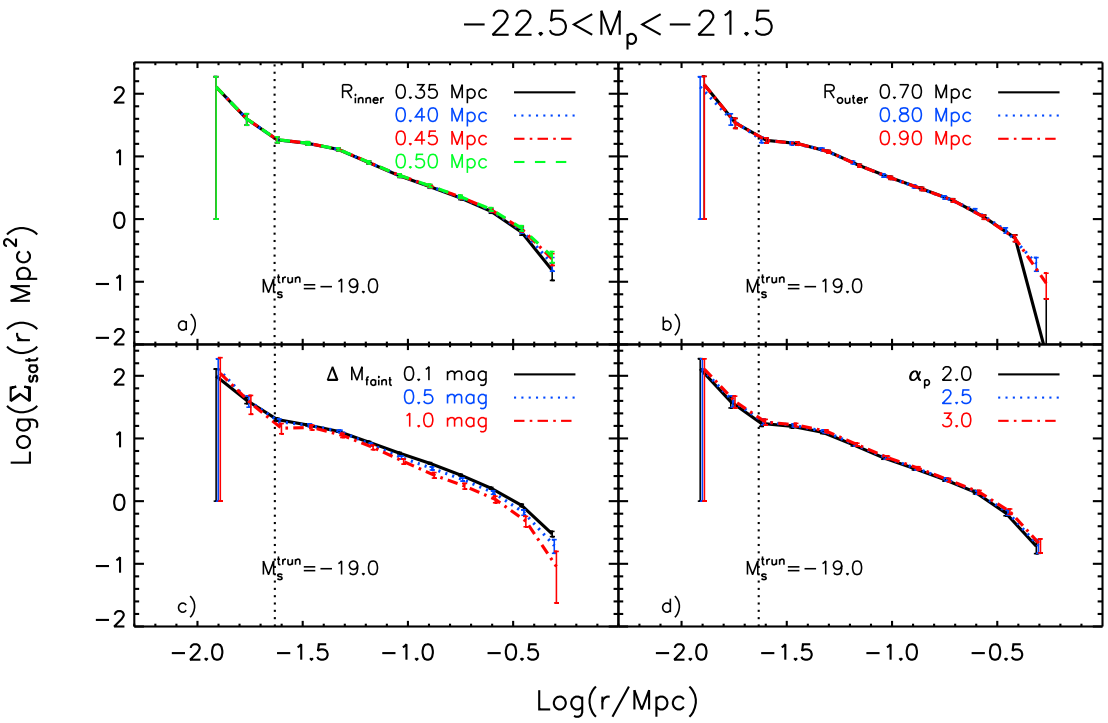

Figure 3.4: The effect on the estimated number density profiles of varying the parameters $\{R_{\rm inner}, R_{\rm outer}, \Delta M_{\rm faint}, \alpha_{\rm p}\}$ from their default values, {0.3 Mpc,0.6 Mpc,0.5,2.5}, as indicated in the legends. Some error bars for different datasets have been slightly shifted for clarity. The vertical dotted lines are the mean of 1.5 times the Petrosian R_{90} of primary galaxies.

3.2.4 Validation of the satellite search parameters

In Fig. 3.4, we show the effect on the estimated number density profiles of varying various satellite search parameters. Panel (a) demonstrates that varying $R_{\rm inner}$ between 0.35 and 0.50 Mpc does not change the profiles significantly, because $R_{\rm inner} = 0.35$ Mpc is already large enough to enclose the whole satellite system for primaries satisfying $-22.5 < M_{\rm p} < -21.5$. The satellite number density profile is similarly robust to changes in $R_{\rm outer}$, which is the outer radius for the background region, as shown in panel (b). The next panel shows the effect of varying $\Delta M_{\rm faint}$, the parameter used to determine if a primary is isolated. There is a very weak variation of the profile shown in panel (c), with primaries allowed to have neighbours with a magnitude difference as small as $\Delta M_{\rm faint} = 0.1$ having slightly more satellites than those with larger magnitude differences to their neighbours, more in keeping with the term isolated. Besides the physically motivated parameters, we also test the parameters of the estimation method. The parameter $\alpha_{\rm p}$ helps us to distinguish genuine satellite galaxies from background galaxies by excluding galaxies that are at a significantly different redshift. Panel (d) shows that our results are insensitive to reasonable changes in the value of $\alpha_{\rm p}$.

3.2.5 Exploring the angular distribution of satellites

The projected radial satellite number density profile, $\Sigma^{\rm sat}(r)$, which is the focus of this Chapter, is the azimuthal average of the 2D surface density, $\Sigma^{\rm sat}(r, \theta)$, where θ can be taken as the position angle between the major axis of the primary and the line connecting the primary and satellite (see Fig 3.5). The angular dependence of this distribution may also carry information on the formation and evolution of the satellites around their primaries. For example, if we assume that the satellite galaxies inhabit an unbiased set of dark matter subhalos, then we would expect satellites to cluster preferentially along the major axis of the halo (Libeskind et al., 2005). Moreover, it is known that the host halos of satellite systems are accreted from filaments, which can cause the angular distribution

of satellites around primaries to be anisotropic (Hartwick, 2000). In fact, numerous such anisotropies have been observed. For example, the famous "Holmberg Effect" (Holmberg, 1969), suggests satellites of isolated, large, and inclined spiral galaxies are preferentially located along the minor axes of their primaries, a result supported by Zaritsky et al. (1997a). However Yang et al. (2006), Azzaro et al. (2007), Brainerd (2005) and Ágústsson & Brainerd (2011) found the opposite effect that satellites prefer alignment with the major axis, especially for the satellites of red primaries. Since the direct observation of satellite systems is not easy, the sample of external satellite systems is limited in both volume and quality. These contradictory results may suggest that the mean amplitude of the anisotropy could be very weak, or the form of the anisotropy could be dependent on the selection of the primaries or even the satellites themselves.

It is therefore interesting to attempt to quantify the mean anisotropy of our large sample of satellite galaxies. We characterise the angular distribution using the position angle θ described in Fig. 3.5. The assumed elliptical symmetry of the primary implies that θ ranges from 0° to 90° with these extremes indicating that the satellites are located along the major or minor axis respectively. The anisotropy of the angular distribution is then quantified by the probability distribution of the angle θ. In practice, accurate measurement of θ requires a robust measurement of the position angle $\phi_{\rm p}$ defining the orientation of the primaries. To achieve this, we adopt the same selection criteria as Siverd et al. (2009). We only select primaries and their satellites that satisfy the condition, $q_{\rm iso} < 0.9$ and $q_{\rm mom} < 0.9$, where $q_{\rm iso}$ is the isophotal axis ratio defined as $q_{\rm iso} = a_{\rm iso}/b_{\rm iso}$ and $q_{\rm mom}$ is the adaptive moments axis ratio, $q_{\rm mom} = ((1-e)/(1+e))^{1/2}$ where $e = (e_+^2 + e_\times^2)^{1/2}$ (Ryden, 2004)[4]. We also exclude the primaries together with their satellites if there is a discrepancy of more than 15 degrees between the measured isophotal and de Vaucouleurs position angles, $\Delta\theta_{\rm p}^{\rm iso-mod} > 15^\circ$.

For our sample of selected satellite systems, the number of satellites located

[4] e_+ and $e_\times$ are second-order parameters from SDSS, where $\tau = M_{xx} + M_{yy}, e_+ = (M_{xx} - M_{yy})/\tau$, $e_\times = 2M_{xy}/\tau$ and M_{XX} here are the second-order adaptive moments.

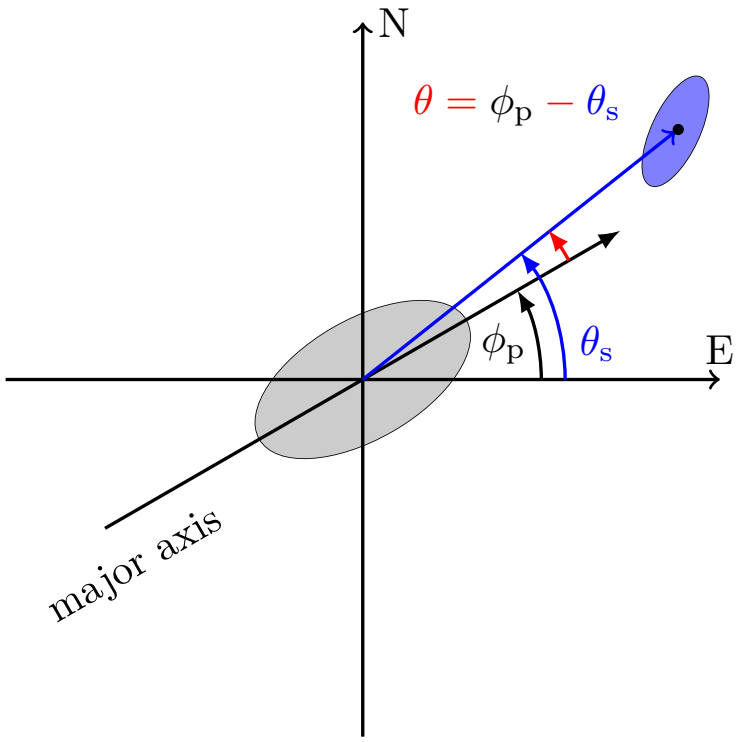

Figure 3.5: Schematic showing the definition of the position angle θ which characterises the angular position of the satellite relative to the direction of the primary galaxy's major axis. The grey and blue ellipses are the primary and satellite galaxy, respectively. The angle $\phi_{\rm p}$ is the position angle of the primary.

at angle θ_j around the ith primary, can be estimated as

$$N_i^{\rm sat}(\theta_j) = N_i^{\rm inner}(\theta_j) - \frac{A_i^{\rm inner}}{A_i^{\rm outer}} \left\langle N_i^{\rm outer}(\theta_j) \right\rangle , \tag{3.2.9}$$

where $\left\langle N_i^{\rm outer}(\theta_j) \right\rangle$ represents the azimuthal average as we assume the background galaxies are, on average, isotropically distributed. Note that to avoid biasing the angular distribution we exclude systems that are incomplete due to the survey mask. We can then define an unbiased estimator of the average distribution of the satellite position angle θ for all selected primaries as

$$\widetilde{N}(\theta_j, M_{\rm sat}^{\rm trun}) = \frac{\sum_i N^{\rm sat}(\theta_j, M_{\rm sat}^{\rm trun})}{N_j^{\rm prim}(M_{\rm sat}^{\rm trun})}. \tag{3.2.10}$$

The normalized probability distribution of θ for primaries in the magnitude bin $M_{\rm c} = -22.0$ is shown in Fig. 3.6. The blue, red and black solid lines in the top panel are the probability distributions of θ for inner galaxies, $P^{\rm inner}(\theta)$, outer galaxies, $P^{\rm outer}(\theta)$, and that inferred for satellite galaxies, $\widetilde{P}(\theta)$, respectively. In the bottom panel of Fig. 3.6, we show the probability distribution of θ for two satellite subsamples split by rest frame colour of their primary galaxies. These samples are divided according to the well-known colour bimodality in the colour-magnitude plane (e.g. Strateva et al., 2001; Baldry et al., 2004; Zehavi et al., 2005). Following Zehavi et al. (2005), we use an equivalent colour criterion of ${}^{0.0}(g-r)_{\rm cut} = 0.19 - 0.24 M_r$ (not identical to Zehavi et al. as our magnitudes are k-corrected to $z = 0.0$ rather than $z = 0.1$). The probability distributions of θ in Fig. 3.6 are all consistent with isotropic distributions. This is confirmed by a two-sample Kolmogorov-Smirnov (KS) test that compares the distributions of inner and outer galaxies for the whole primary sample and also the subsamples of red and blue primaries. The two-sample KS probabilities from the whole sample, blue and red primary subsamples are $0.64, 0.37, 0.87$ respectively, which implies that the pairs of distributions have no statistically significant differences. The same tests for primaries in other magnitude bins show similar results.

Therefore, with our satellite system sample, we find that there is no statistically significant evidence that the distribution of satellites around primaries is anisotropic. This could signify that the anisotropy of the distribution of satellites

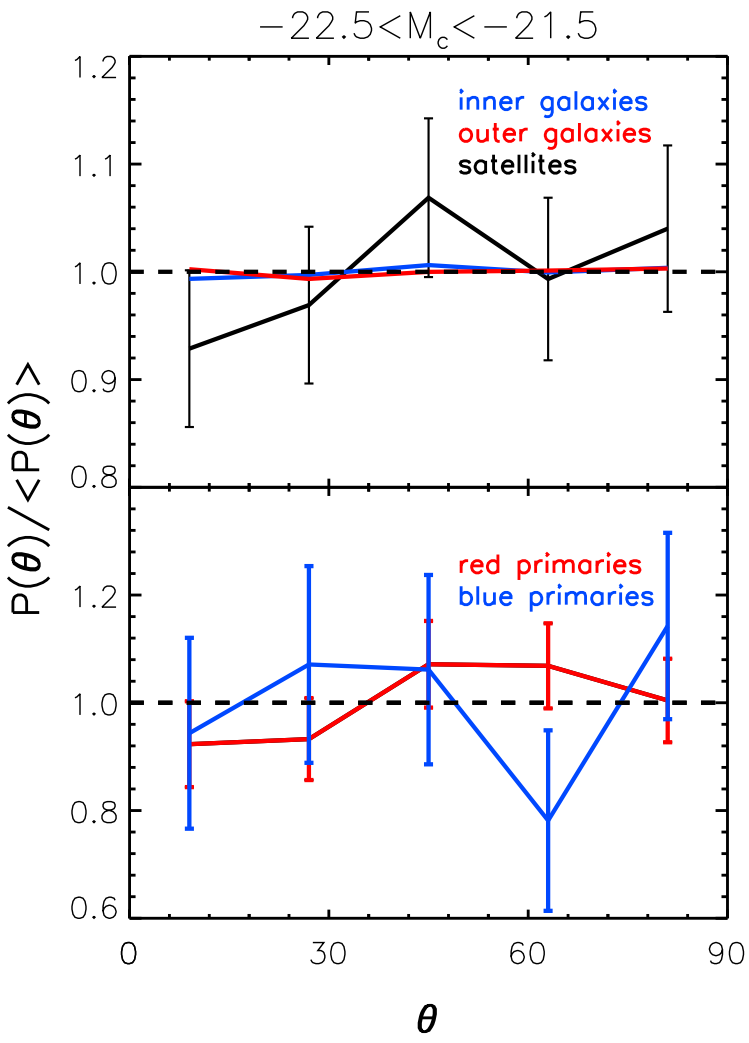

Figure 3.6: The probability distribution, $P(\theta)$, of the position angle θ of satellite galaxies. In the top panel the blue and red lines show the distributions, $P^{\rm inner}(\theta)$, of inner galaxies, and $P^{\rm outer}(\theta)$, of outer galaxies, respectively. The inferred distribution for true satellite galaxies, $\widetilde{P}^{\rm sat}(\theta)$, is shown by the black line. The lower panel shows the distributions for red and blue primary subsamples, as the red and blue solid lines respectively. The error bars are calculated from 1000 bootstrap resamplings. The expectation for a uniform distribution is shown by the dashed lines in the two panels.

around isolated primaries is intrinsically insignificant. However, one also has to keep in mind that our inner sample includes contamination from interlopers, because these are only rejected using inaccurate photometric redshifts, and this could dilute any intrinsic anisotropy signal.

3.3 Results

We now return to the azimuthally averaged density profiles. Density profiles for satellites brighter than $M_{\rm sat}^{\rm trun}$ around primaries of magnitude $M_{\rm c}$ are shown in Fig. 3.7 for a variety of primary magnitude bins and satellite magnitude cuts. Panels 3.7a and 3.7b show that the number of satellites increases with increasing primary luminosity and extends to larger radii. To investigate the variation in profile shape between different subsamples of satellites and primaries, it is helpful to use scaled variables. To this end, we recast the profiles in terms of $x = r/r_{200}$ and divide the number densities by the total number of satellites within r_{200}.

The values of r_{200} used to scale the radii can be determined from the stellar masses, themselves inferred from the measured galaxy luminosities and colours, and the abundance matching technique of Guo et al. (2010), which gives

$$\frac{M_*}{M_{\rm halo}} = c\left[\left(\frac{M_{\rm halo}}{M_0}\right)^{-\alpha} + \left(\frac{M_{\rm halo}}{M_0}\right)^{\beta}\right]^{-\gamma}, \tag{3.3.11}$$

where $c = 0.129$, $M_0 = 10^{11.4}$ $\mathrm{M}_\odot$, $\alpha = 0.926$, $\beta = 0.261$ and $\gamma = 2.440$ are fitted constants. The halo mass can be related to a radius through

$$M_{\rm halo} = \frac{4\pi}{3} 200 \rho_{\rm crit} r_{200}^3. \tag{3.3.12}$$

For the primary galaxies there is a significant uncertainty in the stellar mass that is inferred from the measured luminosities and colours. Thus, rather than using the individual r_{200} values to normalise satellite number density profiles for each primary before stacking them together, the mean r_{200} for all primaries in the luminosity bin of interest is determined and a single rescaling is performed on the unscaled, stacked profile. Using r_{200} values determined in this way, the

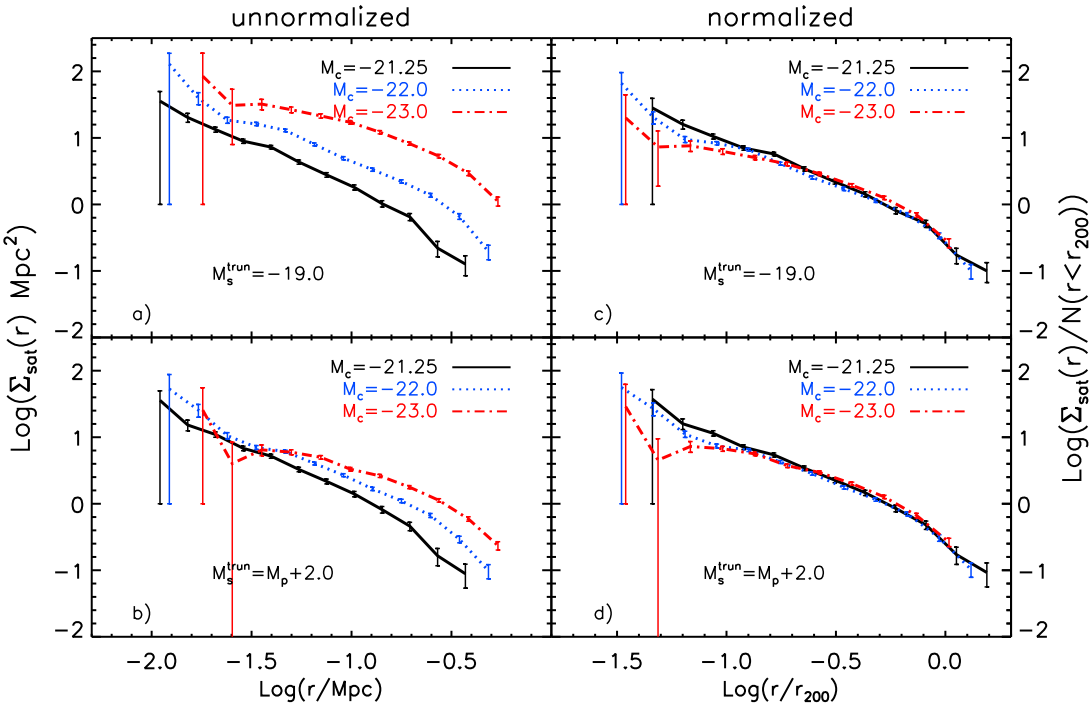

Figure 3.7: The mean projected number density profiles of satellites around primaries for various selections of primaries and satellites. The left hand panels (a and b) show the mean number densities and the right hand panels (c and d) show the same profiles but now normalized by the total number of satellites within the r_{200} radius (see right-hand axis) and with the radius expressed in units of the adopted mean r_{200} radius of the primaries. In each panel the different coloured lines correspond to primaries of differing luminosity as indicated in the legend. The profiles in the upper panels (a and c) are for satellite samples brighter than $M_{\rm sat}^{\rm trun} = -19$, while the lower panels (b and d) are for satellites that are less than 2.0 magnitudes fainter than their respective primaries. The error bars show the errors on the mean profiles estimated by bootstrap resampling.

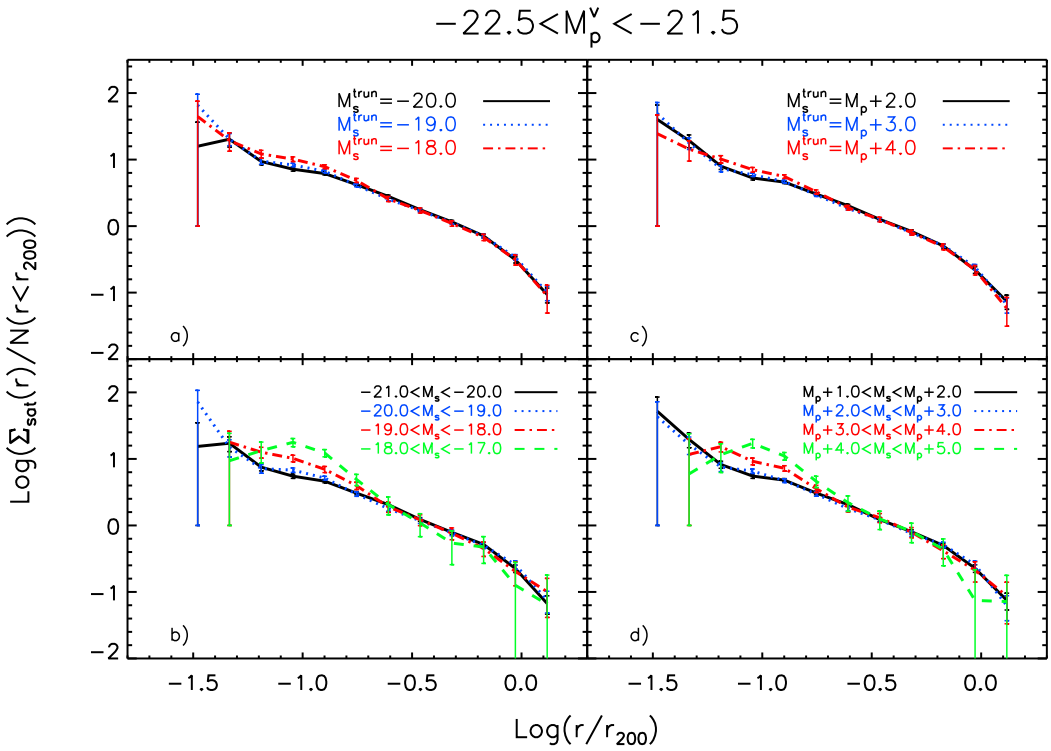

Figure 3.8: The dependence of the scaled satellite density profiles on satellite luminosity for primaries in the magnitude range $-22.5 < M_p < -21.5$. The different panels show different satellite selections. The upper panels, which are very similar, show profiles for satellites brighter than a threshold that is either a fixed value (panel a) or specified as a magnitude difference with respect to the corresponding primary (panel c; see legend). The lower two panels show profiles for satellites in bands of magnitude again either specified between fixed values (panel b) or between values relative to the corresponding primary (panel d).

$M_c = -21.25$ and -22.0 samples line up very well, as shown in panels 3.7c and 3.7d. However, the $M_c = -23.0$ results using r_{200} determined by the same way are slightly offset and are not shown in Fig. 3.7. The actual results that are shown in the Fig. 3.7 are scaled by the empirically chosen r_{200}, 0.52 Mpc. For these, the most luminous primaries, the relation between stellar mass and halo mass becomes very flat and there is a large spread in the halo mass corresponding to a given stellar mass. This makes the assignment of a value of r_{200} to these primaries extremely uncertain. The directly inferred virial radius is 0.73 Mpc but we find that a smaller value of 0.52 Mpc results in better scalings. Given the large uncertainty in this assignment, it is not unreasonable to adopt this smaller value. We shall do this in what follows but this uncertainty must be borne in mind when interpreting the results for the brightest primary bin. The final values of r_{200} for the three primary magnitude bins are $0.24, 0.37, 0.52$ Mpc, the first two of which come directly from equation (3.3.12). By adopting these mean r_{200} values, we have a mass-to-light ratio increasing with luminosity as $M/L_V \propto L_V^{0.42}$. This is similar to the relation found by Prada et al. (2003), albeit for the B-band, from a set of spectroscopically selected satellites from SDSS. For M_V =-22, we find that M/L_V=140.

First, we explore the dependence of the normalized profiles on the luminosity of the satellites. In Fig. 3.8, we show normalized profiles for primaries of fixed luminosity ($-22.5 < M_{\rm p} < -21.5$) with a variety of different satellite selections. In all cases we find the outer shapes of the density profiles to be very similar. The only variation is on small scales (roughly $r/r_{200} < 0.1$) where the density profile is steeper and higher for the faintest satellites.

We examine the shape of these density profiles more systematically in Fig. 3.9 where we fit the unnormalized density profiles using an analytic model. We have chosen to fit our satellite profiles using NFW profiles as they are known to be good fits to both dark matter haloes (Navarro et al., 1996, 1997) and to the distribution of substructures within them (Diemand et al., 2004; Springel et al., 2008a; Ludlow et al., 2009). To perform these fits we first project the NFW profile and subtract from it the mean density in an outer "background" annulus

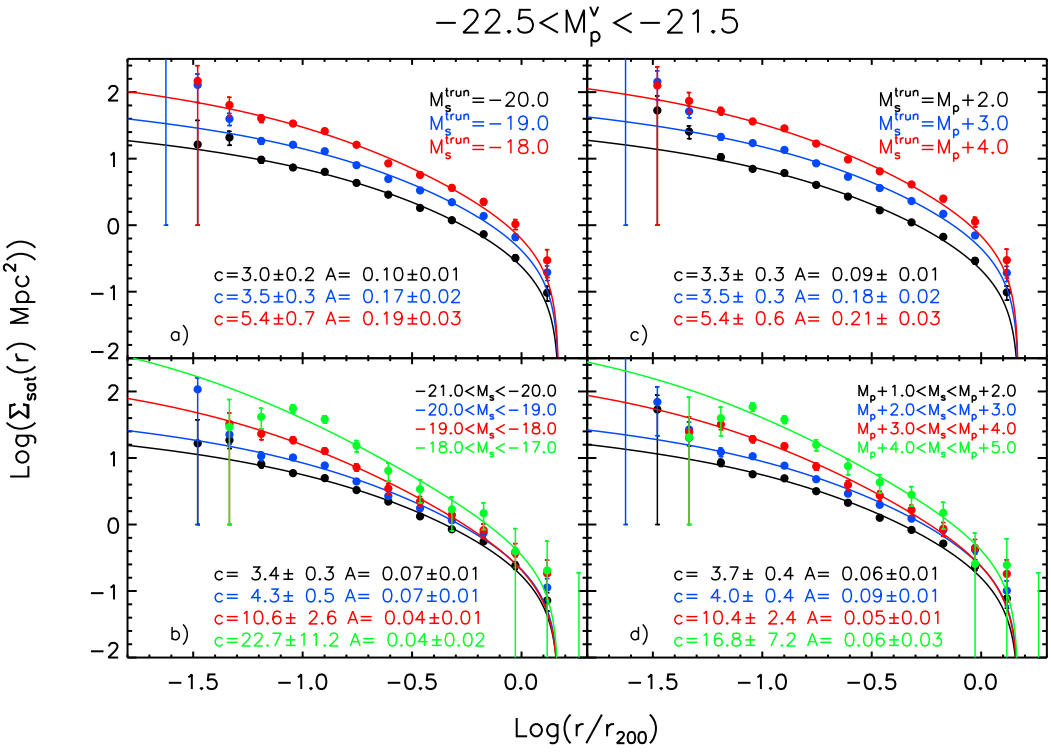

Figure 3.9: b

ackground-subtracted NFW profiles. Fits to the satellite density profiles of primaries of magnitude $-22.5 < M_p < -21.5$ using projected, background-subtracted NFW profiles. The various panels show different selections of satellites as in Fig. 3.8, except that here we have not normalized the profiles, but instead allowed the amplitude, A, of the fitted profiles to float. The measured profiles are shown by the data points and the best fitting NFW profiles are plotted as solid lines. The best fitting amplitudes and concentrations are listed in the legends in each panel.

as described in Section 3.2.3, so as to match the background subtraction process that we have applied to our observational data. We then perform a fit using $\Sigma^{\rm sat}(r) = A\hat{\Sigma}(r, c, r_{200})/M_{200}$, where A is a scale factor, c is the concentration, and $\hat{\Sigma}(r, c, r_{200})$ is the projected NFW profile with background subtracted as given in Eqn. 3.2.8. The r_{200} radius is fixed to the respective values that we have adopted for each of our bins of primary magnitude.

Fig. 3.9 shows the resulting fits. The bright satellites, such as satellites with magnitudes $-21.0 < M_s < -20.0$ or $M_{\rm p} + 1.0 < M_s < M_{\rm p} + 2.0$ are very well fitted by the projected and background subtracted NFW profiles. The NFW fits also remain good descriptions of the data for the cumulative samples of satellites defined by a faint magnitude threshold. For these samples, shown in the upper panels of Fig. 3.9, the concentration increases steadily with decreasing luminosity. In the lower panels of Fig. 3.9, which show density profiles for satellites in differential bands of luminosity, we see both a stronger dependence of concentration on luminosity and small deviations from the NFW form for the faintest satellite samples.

We now turn to the dependence of the satellite profiles on the magnitude of the primaries. In Fig. 3.10 we show fits of the projected and background-subtracted NFW profiles to satellite profiles of primaries in each of our three magnitude bins. Each of the panels corresponds to a different selection of satellites. We see that NFW fits are good descriptions of the satellite distribution regardless of the luminosity of the primary. The right hand panels of Fig. 3.10 show the density profiles and fits for sets of satellites defined by fixed offsets in magnitude from the magnitude of their respective primary. If the combined primary and satellite systems scaled in a self-similar way we would expect the three density profiles in each of these panels to lie on top of each other. In contrast, in each panel, we see systematic variations in the shape and amplitude of the profiles with the primary luminosity. If instead we look at the left hand panels, which show satellites selected in different fixed magnitude bands, then we see that the concentration decreases steeply with increasing satellite luminosity, but is less dependent on the luminosity of the primary. With the exception

of the brightest primary magnitude bin ($M_c = -23.0$), the satellites of a given luminosity are more or less distributed in the same way about primaries of different luminosity. Only the normalization of the profile, as parameterized by A, increases with increasing primary luminosity. This depends quite strongly on luminosity going roughly as the luminosity to the power of 2.5. If we normalized each of these satellite profiles as we did in Fig. 3.8, then their shapes would show very little variation with primary luminosity.

For the case of primaries in the $M_c = -23.0$ bin, the measured concentrations for the satellite distributions are systematically lower than those of similar luminosity satellites around less luminous primaries. The reason for this is not clear. It may be that this result reflects the actual satellite distribution around bright primaries. However, it could be an artefact of the estimation procedure. One possibility is that the non-linearity of the halo mass-stellar mass relation (Guo et al., 2010) means that the range of actual halo mass increases in the brightest primary bin. Thus, stacking all primaries using a single r_{200} value may be introducing errors that would smear out the resulting profile. Another potential source of systematic error comes from the tendency for faint satellites to be missed around bright primaries because of inaccuracies in the sky-subtraction (Mandelbaum et al., 2005). Even with the updated sky-subtraction algorithm employed for DR8 there may still be some residual loss of faint satellites around the brightest primary galaxies (Aihara et al., 2011).

3.3.1 Colour and type dependence

Our large sample of satellite systems enables us to divide our samples by the colour or the type of the primaries. Fig. 3.11 shows the resulting profiles when primaries of V-band magnitude -22.0 ± 0.5 are split by colour and by concentration. Panels a) and c) of Fig. 3.11 show that the normalized profile of satellites around blue primaries is more concentrated than that around red primaries. Panels b) and d) split the sample into early and late types, where early type is defined as having a concentration index $\mathcal{C} \equiv petroR_{90}/petroR_{50} \geq 2.6$, with $petroR_{90}$ and $petroR_{50}$ being the SDSS Petrosian 90% and 50% light radii respec-

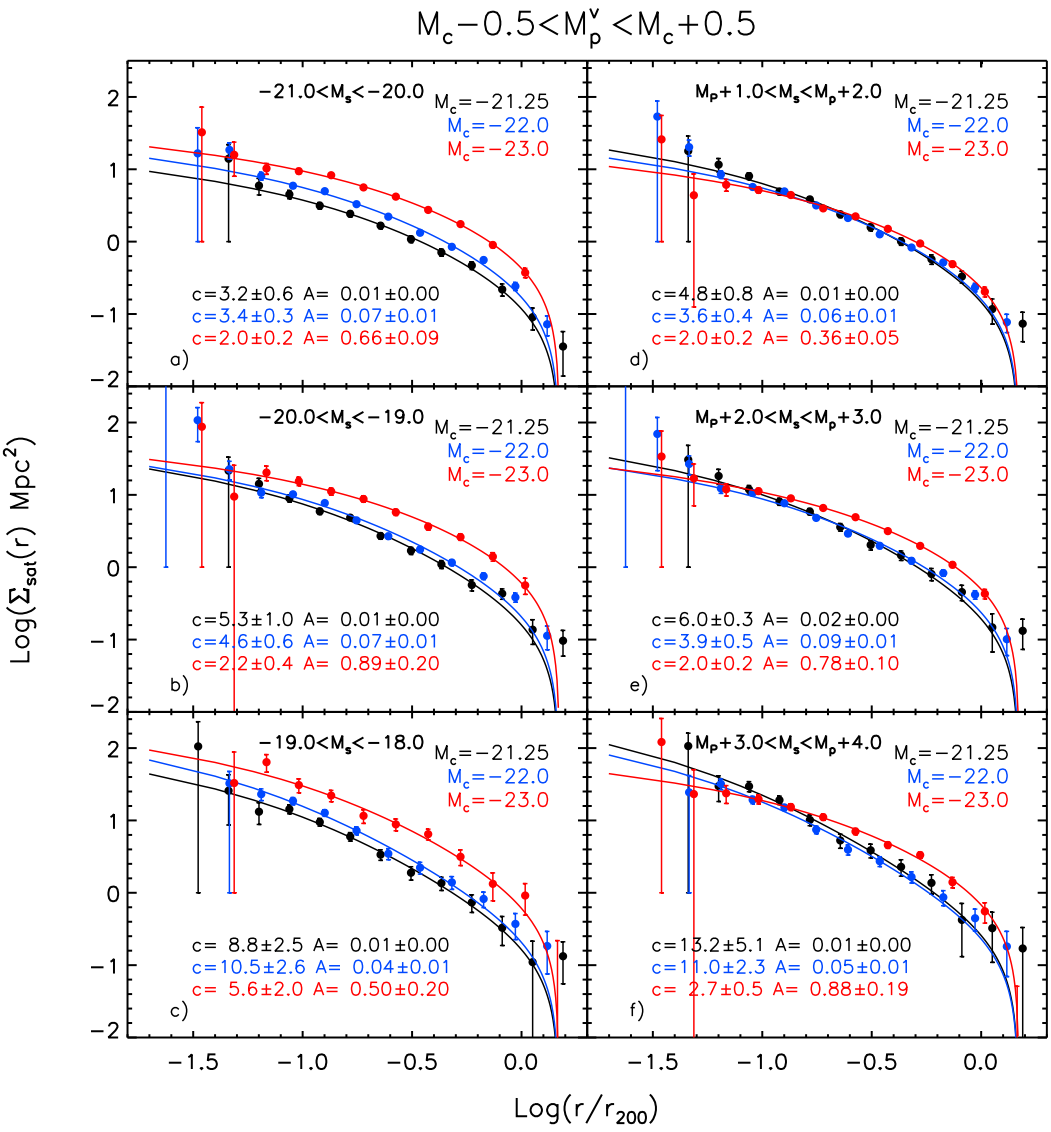

Figure 3.10: NFW fits to the density profiles of satellites around primaries of different luminosity. Each panel shows fits for the three different bins of primary luminosity indicated in the legends. The different panels correspond to different selections of satellites. The panels on the left, a), b) and c), are for successively fainter bands of satellite luminosity as indicated on the legend, with the range of satellite magnitudes being the same for each primary. In contrast the panels on the right, d), e) and f), are for bins of satellite magnitude that are specified as an offset relative to the magnitude of their respective primary.

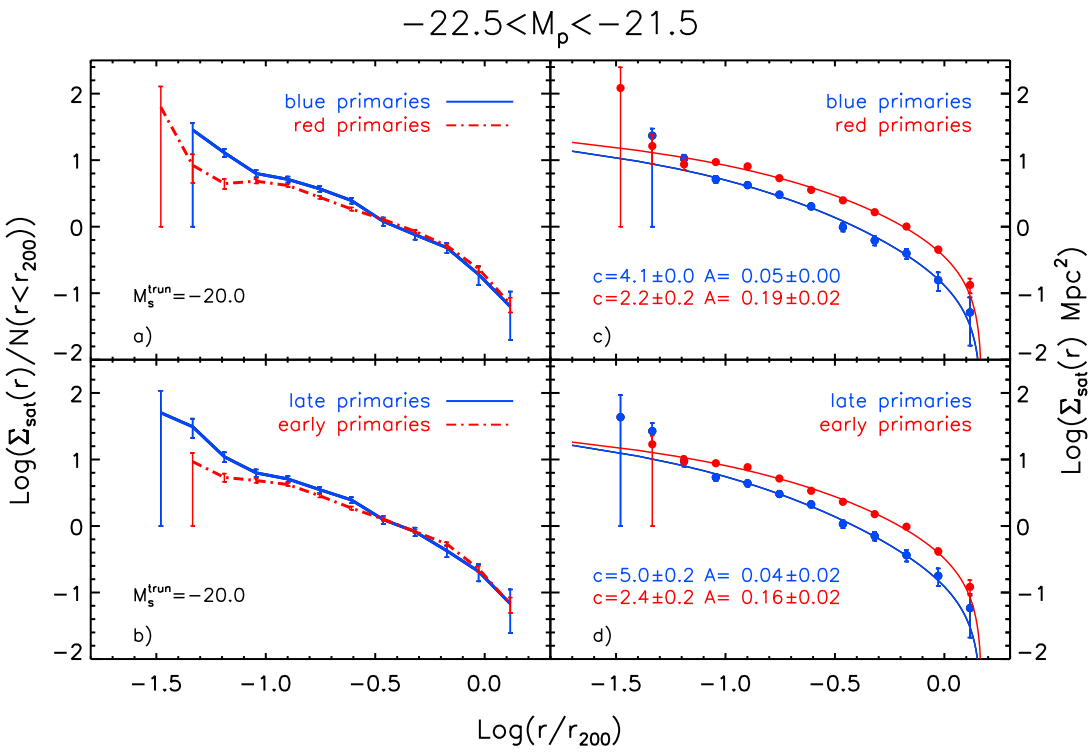

Figure 3.11: The satellite profiles for primary galaxies of magnitude $-22.5 < M_p < -21.5$ split by the type (concentration) and colour of the primary. Panels a) and b) show the normalized profiles while panels c) and d) show NFW fits to the unnormalized profiles (see right hand axis). In the upper panels the blue lines refer to blue primaries and red lines to red primaries, while in the lower panels blue refers to late-type primaries and red to early types.

tively. This division roughly separates early type (E/S0) from late-type (Sa/b/c, Irr) galaxies (Shimasaku et al., 2001). We also see the amplitude of the profiles of late types is suppressed with respect to that of the early types. However, the concentration indices, c, from the fits similarly show that the concentration of satellites around late types is higher than that of early types.

We can also use the colour information available in SDSS to probe the properties of the satellites. Firstly, for the bin of primary magnitude, $M_c = -22.0$, we divide the satellites into two luminosity bins, $-21.0 < M_s < -20.0$ and $-20.0 < M_s < -19$ and into red and blue subsamples using the same cut as before. Fig. 3.12a,b,d and e show the measured profiles of these blue and red

satellites and NFW fits. We first note from Fig. 3.12d and e that for these relatively bright satellite samples the abundance of blue satellites is greater than that of red satellites at all radii, with this difference increasing for the fainter sample. The profiles of the brighter satellites have a similar shape for red and blue satellites, while the fainter red satellites have an excess at $\sim 0.1 r_{200}$ relative to the fainter blue satellites. To investigate whether these differences are driven by the colours of the associated primary galaxies we further split the satellites brighter than $M_{\rm s}^{\rm trun} < -20$ by the colour of their primary. The results are shown in Fig. 3.12c and f. Both red and blue primaries have more blue than red satellites. The concentrations of red and blue satellites around blue primaries are similar. Red primaries have lower concentrations for both their red and blue satellites, with the blue satellites having a particularly low concentration. The colour of the primary appears to be more important than that of the satellite in determining the concentration of the satellites. As shown in Fig. 3.10, the satellite luminosity also has a strong effect.

3.3.2 Comparison of results from DR8 with DR7

We have performed our measurement of satellite number density profiles for both the SDSS DR8 and DR7. This helps to quantify the impact on the number density profiles of the different sky-subtraction algorithms used to define these galaxy catalogues. Looking at images of some of our primary galaxies in DR7, there were occasions when close-in satellite galaxies existed that were not present in DR8. The suggestion is that these are spurious fragments of the primary galaxy itself, following inexact subtraction of the background sky level. One would expect such a problem to be worse for lower luminosity satellites and also if the inner radius cut to be considered is reduced beyond our default 1.5 times the Petrosian R_{90}. Fig. 3.13 shows some illustrative results where satellites down to 0.5 times the Petrosian R_{90} have been included in the profiles around $M_{\rm c} = -23.0$ primaries. There is a tendency for DR7 to have extra low luminosity satellites near to the primary, which is not shared by DR8. This is particularly evident in the lower panel. Furthermore, while the DR8 profile is robust to

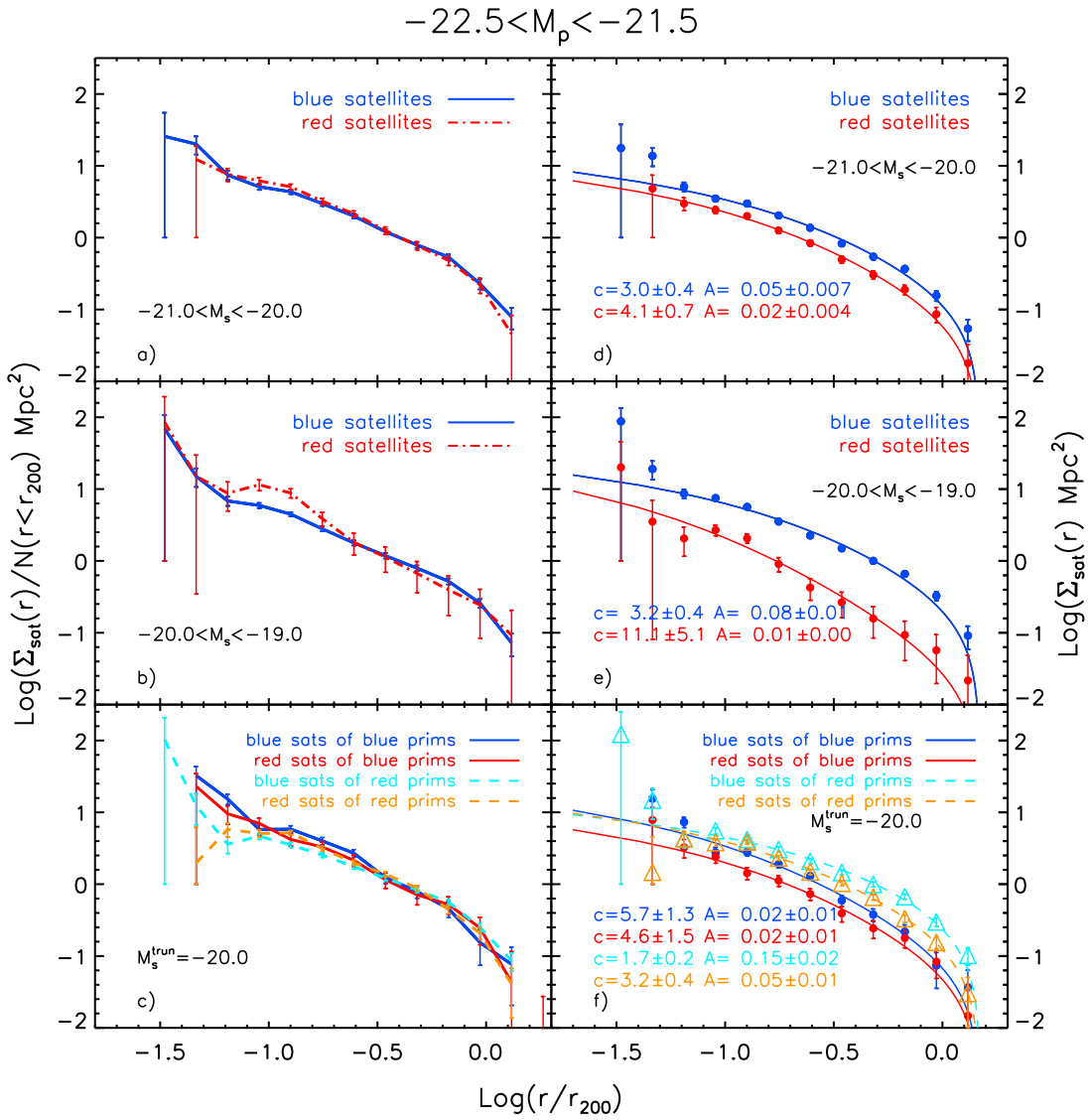

Figure 3.12: Satellite density profiles split by the colour and luminosity of the satellites. Panels a) and b) compare the profiles of blue (blue solid line) and red (red dot-dashed line) satellites for two different bins of satellite luminosity (see legend). Panels d) and e) show the corresponding unscaled profiles as red and blue symbols together with curves depicting NFW fits. The best fitting amplitudes and concentrations are (Continued on the following page.)

Figure 3.12: (continued) given in the legends. For satellites brighter than -20.0, panels c) and f) compare the profiles of red and blue satellites around red and blue primaries. The profiles for blue primaries are shown with solid lines and those for red primaries with dashed lines. The blue and cyan lines are for blue satellites and red and orange lines for red satellites as detailed in the legends. In panel f) the smooth curves show the NFW fits to the corresponding unscaled profiles and again the best fit parameters are listed in the legend.

changing the inner radius cut, the result for the low luminosity satellite profile around bright primaries from DR7 changes significantly. We conclude that DR7 contains more spurious fragmentation of bright primary galaxies, and that DR8 is preferable for our study, both in terms of the reliability of the faint galaxies and their improved photometry.

3.4 Discussion

Using a stacking analysis we have estimated the mean projected density profiles of satellite galaxies around a large sample of isolated primary galaxies selected from the SDSS DR8 spectroscopic galaxy catalogue and we have quantified how they depend on the properties of the satellites and primaries. The selection of primaries and the local background subtraction technique, which makes use of photometric redshifts, is the same as in Chapter 2 or Paper I (Guo et al., 2011) where we estimated the mean satellite luminosity functions of these systems. Our main conclusions are:

(i) We find no evidence for any anisotropy in the satellite galaxy distribution relative to the major axes of the primaries.

(ii) The projected number density profiles of satellites brighter than a V-band magnitude of -17 are well determined for three separate bins of primary magnitude, $-21.25, -22, 0, -23.0$.

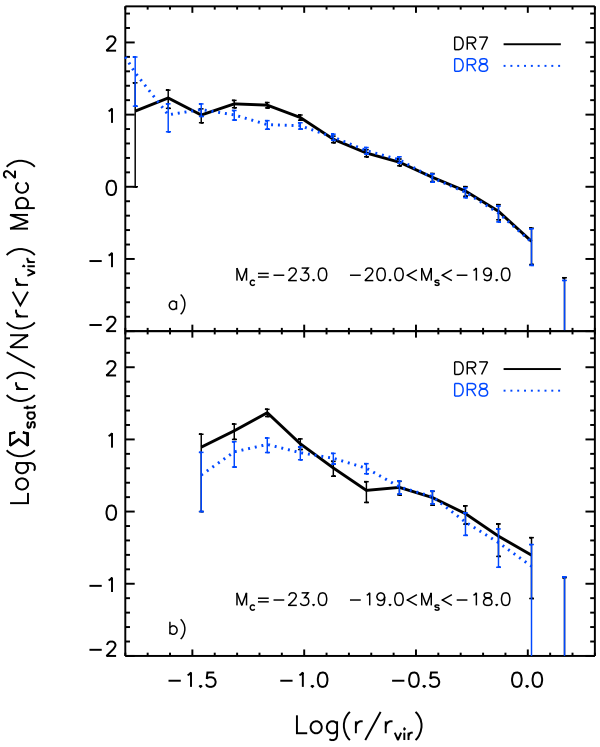

Figure 3.13: A comparison of profiles based on SDSS DR8 and DR7 for a) more luminous satellites, and b) less luminous satellites. The black (solid) lines are the profiles from DR7. The blue (dotted) lines are the profiles from DR8. A cut at 0.5 times the Petrosian R_{90} radius is used to highlight the difference.

(iii) Apart from the faintest satellites, for which there is a slight excess at small galactocentric projected distance, all other density profiles are well fitted by projected NFW profiles that have been background subtracted to match the procedure that has been applied to the data.

(iv) The concentration of the NFW fits decreases systematically with increasing satellite luminosity and is almost independent of the luminosity of the primaries (see Fig. 3.10). Thus, bright satellites have more extended distributions and fainter satellites are more centrally concentrated.

(v) The radial distribution of satellites is dependent on the colour and morphology of their primaries. Satellites are more numerous around red/early primaries and have more extended, lower concentration, distributions (see Fig. 3.11).

(vi) The radial distribution of satellites also depends on the colour of the satellites. Blue satellites are more numerous than red satellites at all radii (for the luminosity range we probe) and faint red satellites are more centrally concentrated (higher NFW concentration) than faint blue satellites. Further sub-divided samples show that the concentration of the blue or red satellite profile depends more on the colour of the primaries than it does on the colour of the satellites.

As a check of potential systematic effects in our results, we have also performed the same analysis using the SDSS DR7 dataset. Generally, the results based on DR7 are consistent with those from DR8, although we do observe some differences in the distribution of faint satellites. This is most likely due to less accurate photometric reduction and sky-background subtraction for DR7 (see Section 3.3.2 for more details).

With the advantage of our large and carefully selected samples, we have discovered a variety of interesting information about the projected number density profiles, which it has not been possible to quantify clearly in previous work. However, even with a very limited sample, a pioneering study by Lorrimer et al. (1994) found that the distribution of satellites is dependent on the morphology of primaries. They found that the number of satellites around early-type primaries is greater than that about late-type primaries and that the concentration of the satellite distribution is higher around early type primaries. We confirm

the greater abundance of satellites around early-type primaries, but contrary to Lorrimer et al. (1994) we find higher concentrations for satellite systems around late-type primaries. More recently, van den Bosch et al. (2005), Sales & Lambas (2005) and Chen et al. (2006) studied the projected number density profiles of satellites of isolated galaxies using larger samples from the Two Degree Field Galaxy Redshift Survey (2dFGRS) and SDSS. Although van den Bosch et al. (2005) cautioned that the profiles from 2dFGRS were incomplete because of incompleteness in close galaxy pairs, their study revealed that satellites followed NFW profiles. Sales & Lambas (2005) found that the profiles of satellites depart from a power law at small galactocentric projected distance, and that they are dependent on the colour of the primaries, which is similar to our conclusions (iv) and (v). They also found the distribution of satellites to depend on their colour, but argued that this may be caused by the correlation between satellites and primaries. In our study, conclusion (vi) shows that the distribution of satellites not only depends on the properties of satellites, but also depends on the colour of primaries. Chen et al. (2006) and Tollerud et al. (2011) selected samples only from the SDSS spectroscopic catalogue in their studies. Tollerud et al. (2011) found the 3D number density profiles of satellites can be fitted by a power-law with a slope $\rho \propto r^{-1.8}$. After projecting, the slope of this density profile will be close to ours. With a careful treatment of interlopers, they fitted the profiles with a power-law form and found them to be independent of the luminosity of the primaries. These conclusions are consistent with ours. Very recently, Lares et al. (2011) estimated the radial density profiles of satellites around primary samples brighter than -20.5 and -21.5. They also found the amplitudes of the profiles depend on the luminosity of the primaries, and the shapes on their colour.

The physics of the projected number density profiles of satellites involves both the physics of the hierarchical assembly of dark matter halos and the physics of the galaxy formation that occurs in these assembling halos. Hence quantifying these profiles will help constrain both galaxy formation models and the nature of the dark matter. We expect that our profile results and those of others will be an important input into refining theoretical models and the next

incarnation of full N-body/gasdynamic simulation that can resolve the physics of the formation of satellite galaxies.

4

COMPARISON OF BACKGROUND SUBTRACTION METHODS

In this chapter, we explore the dependence of satellite luminosity functions on the background galaxy subtraction method. In Chapter 2, Section 2.3, for each acceptable primary galaxy, the potential satellites were selected from the inner area, and the galaxies from the outer annulus are used to estimate the background. The number of true satellites was estimated by counting the difference between the number density of galaxies within $R_{\rm inner}$ and in the local reference annulus (hereafter the local background). The number density of background galaxies for each primary is determined around the primary itself. Therefore, the method of counting true satellites based on subtracting a local background is called the local background method hereafter. Meanwhile, Wang & White (2012) have also estimated satellite galaxy luminosity functions by a method in which inner galaxies are selected in a similar way. However, the background they use is estimated globally. In this method, the background of each primary is estimated by using all galaxies within the whole survey area. Therefore, it is called the global background method.

4.1 The Differences Between The Two Methods

We detect satellite galaxies when the number density of galaxies within $R_{\rm inner}$ is slightly larger than the number density of background galaxies. Both the local background method and global background method are based on this same

idea. However, the two methods reflect two slightly different definitions of the satellite galaxy system. In this chapter, we intend to explore the differences between these two methods. Here we have developed a version of the global method of estimation of satellite LFs, in which the inner galaxies are selected according to the local method, while the backgrounds are estimated globally by using the mean number density of all galaxies in the catalogue. We are going to explore how these two methods are affected by different observational factors, by comparing the differences of the resulting satellite LFs.

However, one should note that the global method we used here is not exactly the same as the one in Wang & White (2012). Firstly, the catalogues that we and Wang & White (2012) used are different. We selected primaries and satellites from both the SDSS DR8 spectroscopic catalogue and the photometric catalogue and adopt SDSS model magnitudes. While Wang & White (2012) selected primaries from the SDSS DR7 spectroscopic catalogue using Petrosian magnitudes and selected satellites from the SDSS DR7 photometric catalogue using model magnitudes. Secondly, the isolation criteria for primaries also differ. Thirdly, the satellite counting methods are different. In Wang & White (2012), their satellite counting method is more complicated. The number of inner satellites they count is not only dependent on $R_{\rm inner}$, but also dependent on the $g-r$ colour. Therefore, in their method, the total number of inner galaxies is the sum of the number of galaxies in the colour bins which are not too red to observe satellite galaxies at certain redshift. The colour bins are too red will be excluded, because the galaxies in these bins are too red to be the real satellites which can be observed at the redshift of the primaries. Excluding these colour bins could reduce the noise. The outer galaxies are counted in the same way. However, in our global method, we simply count the total number of inner galaxies and outer galaxies regardless of their colour. We will explore the effect of excluding the very red galaxies later.

Fig 4.1 shows that satellite luminosity functions estimated by the local background method and the global background method for the primaries in the same primary magnitude bin, $M_c = -21.0$, are quite different. One possible reason is

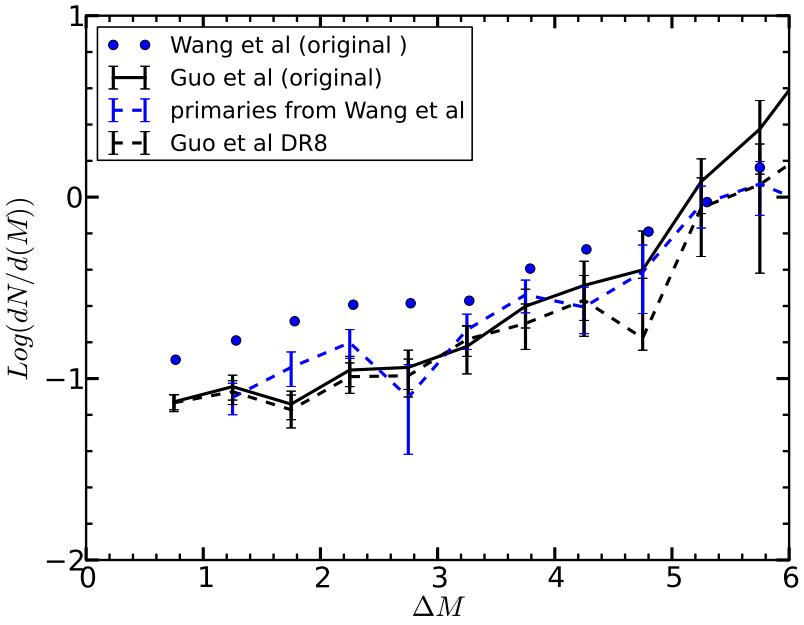

Figure 4.1: Satellite LFs for different selections of primaries. The black solid and dashed lines are the satellite LFs estimated using the local background method from SDSS DR7 and SDSS DR8 respectively. The blue points are the satellite LF estimated using the global method in Wang & White (2012), while the blue dashed line is the satellite LF for the same primaries, but estimated using the local background method.

that in Chapter 2, Section 2.3, our primaries and satellites are selected from the SDSS DR7 catalogues, while Wang & White (2012) select primaries from SDSS DR7 NYU Value-Added Galaxy Catalog catalogue (Blanton et al., 2005) and select satellites from SDSS DR8 catalogue. We already know that the SDSS DR8 catalogue is different to the SDSS DR7 due to the photometric pipeline having been improved. However, in Fig 4.1 the black solid line and black dashed line are the satellite LFs estimated with the local background method from SDSS DR7 and DR8 catalogues respectively, which do not show any significant difference. The other possible reason is that the definition of isolated primaries in Wang & White (2012) is different to the definition in this thesis. We estimated the satellite LF, using the local background method, for the primaries that were selected by Wang & White (2012) (blue dashed line). This is closer to the other satellite LFs estimated with the local background method. The results are quite different to those from the global background method in Wang & White (2012), shown by the points in Fig 4.1.

4.2 Observational Factors

The difference between the satellite LFs estimated using different methods cannot be explained by the simple reasons we previously mentioned. Therefore, we explore how observational factors affect the estimated satellite LFs. We change the same observational factors for the two methods at the same time. As the way of counting inner galaxies is the same in these two methods, the difference between the resulting satellite LFs can only be caused by the different methods of estimating the background.

4.2.1 Apparent magnitude cuts for primaries

Here, the magnitude limit of primaries $m^{\rm lim}$ is defined such that the acceptable primaries satisfy $m_{\rm p} < m^{\rm lim}$. In Fig 4.2, we show the satellite LFs for the primaries with a different magnitude limit ($m^{\rm lim} = 16.5, 17.2, \infty$). The ∞ means the primaries only have the spectroscopic sample magnitude limit cut 17.7. The

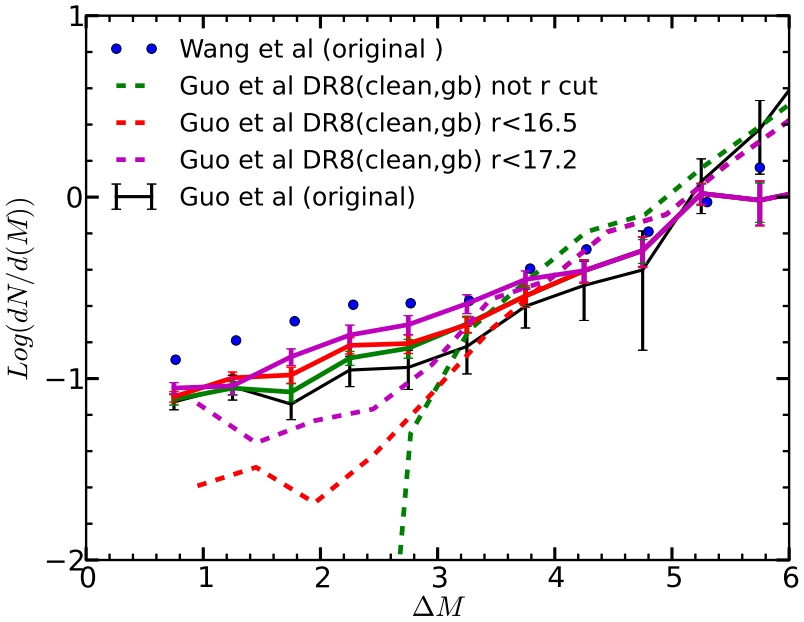

Figure 4.2: Satellite LFs for primaries with different apparent magnitude cuts. The blue points are the satellite LF estimated using the global method in Wang & White (2012). The coloured solid lines are the satellite LFs estimated by the local background method for primaries with different magnitude cuts. The coloured dashed lines are the corresponding satellite LFs estimated with the global background method.

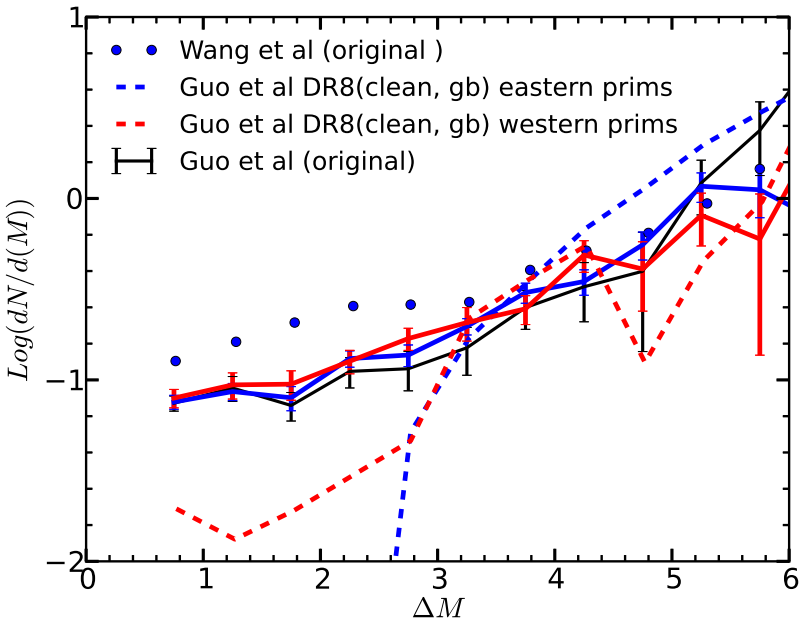

Figure 4.3: Satellite LFs for primaries in the "east" and "west". The blue points and the solid black line are the satellite LFs as in previous plots. The coloured solid lines are the satellite LFs estimated using the local background method for primaries within east and west subsamples. The coloured dashed lines are the corresponding satellite LFs estimated by the global background method.

satellite LFs for primaries with different magnitudes, estimated using the local background are much more stable than those estimated via the global background method.

4.2.2 The large-scale homogeneity of the survey footprint

Secondly, we tried to split primaries into "east" and "west" samples, according to their celestial positions. Primaries that are within the area RA $< 210^{\circ}$ are labelled as "east", and primaries otherwise are labelled as "west". From Fig 4.3, we can see that the satellite LFs estimated are obviously different, which suggests that global backgrounds estimated from east and west regions are different. It could be caused by unknown systematics on large scales. However, the

results estimated by the local background method are seen to be less affected by the celestial positions of the primaries. Therefore, the local method will be very likely to be insensitive to any factors affecting large scales.

4.2.3 K-corrections

Thirdly, in Wang & White (2012), primaries are k-corrected to redshift $z = 0.1$, whilst in this thesis primaries are k-corrected to redshift $z = 0.0$. Different k-corrections result in the same bins of primary magnitude, actually being centered at slightly different luminosity. Fig 4.4 shows the satellite LFs for the primaries with different k-corrections estimated using the different background methods. The satellite LFs estimated with the global method for primaries with k-corrections to redshift $z = 0.0$ and k-corrections to redshift $z = 0.1$ are significantly different in the range $\Delta M < 3$, which cannot be explained by the slight luminosity difference between the primary samples selected with different k-corrections. In contrast, the satellite LFs estimated with the local method again show a relatively small difference that could be caused by the luminosity difference between the two primary samples.

4.2.4 Very red galaxies

Finally, in Wang & White (2012), the authors exclude all satellites redder than $(g-r)^{0.1} = 0.032 \log M_* + 0.73$, a fit to the upper envelope of the distribution of rest-frame colour against stellar mass for galaxies of measured redshift, because these neighbouring galaxies are too red to be at the redshift of the primary. We also tried to explore the effect on the satellite LFs of including galaxies filtered by different colour cuts. The results are shown in Fig 4.5, which also indicates that the estimate using a global background is quite sensitive to this factor.

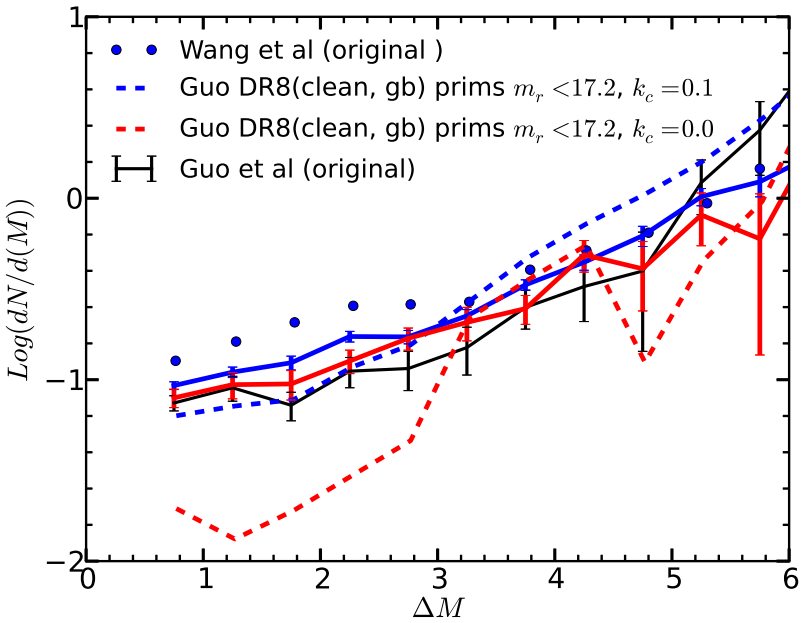

Figure 4.4: Satellite LFs for primaries with different k-corrections. The blue points and the solid black line are the satellite LFs as in the previous plots. The coloured solid lines are the satellite LFs estimated using the local background method for primaries with different k-corrections. The coloured dashed lines are the corresponding satellite LFs estimated with the global background method. $k_c = 0.0$ and $_c = 0.0$ means the primaries k-corrected to z=0.0 and z=0.1 respectively.

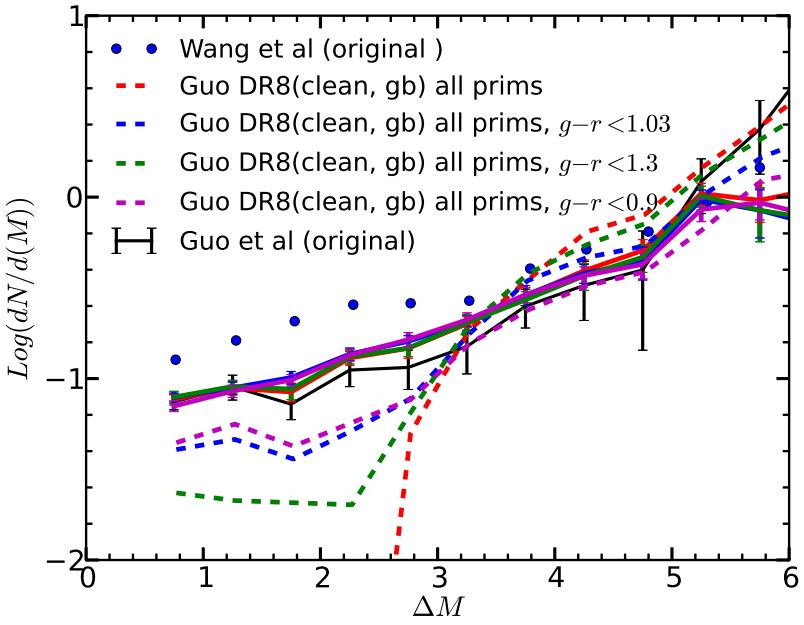

Figure 4.5: Satellite LFs with different colour cuts. The blue points and the solid black line are the satellite LFs as in previous plots. The coloured solid lines are the satellite LFs estimated using local backgrounds method in which only galaxies not redder than 0.9, 1.03, 1.3 and ∞ respectively. The coloured dashed lines are the corresponding satellite LFs estimated with the global background method.

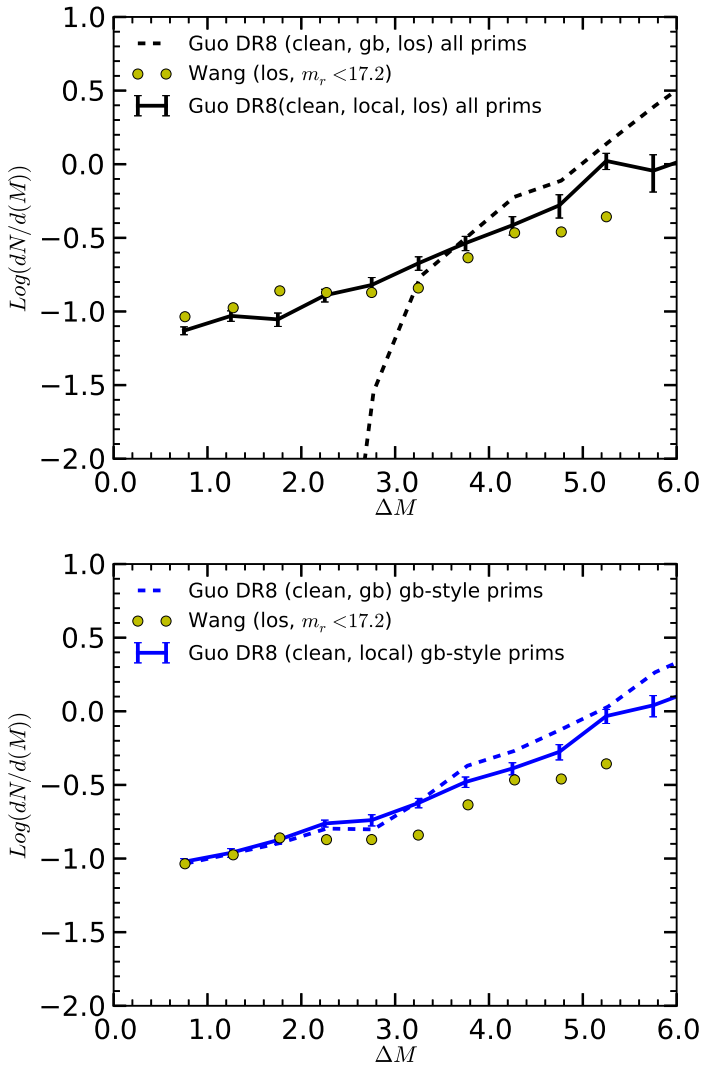

Figure 4.6: Satellite LFs for different selections of primaries. In the top panel, the primaries are selected via the default way in this thesis. The black solid line is the satellite LF for such a primary sample estimated using the local method, and the black dashed line is the corresponding result estimated with the global method. While in the bottom panel, the primaries are selected in a way more similar to Wang & White (2012), in which the primaries have $m_p^{\rm lim} = 17.2$ and are k-corrected to $z = 0.1$. The primaries selected in this way are called "gb-style" primaries. (Continued on the following page.)

Figure 4.6: (continued) The solid blue line is the satellite LF estimated using the local method for the so-called "gb-style" primaries. The blue dashed line is the corresponding result estimated by the global method. The green points are the satellite LF estimated using the global method in Wang & White (2012) for primaries selected in a very similar way.

4.3 Discussion and Conclusion

In the previous section, we explored several observational factors that may affect the estimation of backgrounds. The results suggest that the estimation of a global background is quite sensitive to these factors. Considering these observational factors, it is possible that our version of the global method to estimate satellite LFs produces similar results to those in Wang & White (2012). For example, in Fig 4.6, we show that the different way of selecting primaries can dramatically change the satellite LF estimated by the global method, (from the black dashed line to the blue dashed), whilst the results estimated by the local method remain stable (from the black solid line to the blue solid line). Our version of the global method can also produce a result that is similar to that of the global method in Wang & White (2012).

By definition, the global background is uniform everywhere. However we have shown that, the results estimated with the global method vary significantly, which suggests that the global method might not be a reliable method for estimation of satellite LFs from the SDSS DR8 catalogues. A possible reason could be that the SDSS survey covers a very large area and some unknown systematics may not be clearly removed. Therefore, the estimation of global backgrounds are probably biased. However, the local method avoids this issue, because these unknown systematics are cancelled out due to the inner areas and outer annulus in the local method being very close on the celestial sphere. And we want to estimate the background from a Mpc to several tens of Kpc near to the primaries. The galaxy correlation function tells us that this is likely to above a

global average. Therefore, the local background could be a better approach.

5

SPATIAL AND LUMINOSITY DISTRIBUTIONS OF MODEL GALACTIC GALAXIES

In this Chapter, we investigate the luminosity functions (LFs) and projected number density profiles of galactic satellites around isolated primaries of different luminosities. We measure these quantities for model satellites placed into the Millennium and Millennium II dark matter simulations by the GALFORM semi-analytic galaxy formation model for different bins of primary galaxy magnitude and we investigate their dependence on satellite luminosity. We compare our model predictions to estimates from the SDSS made in Chapter 2,3. First, we use a mock light-cone catalogue to verify that the method we used to count satellites in the SDSS DR8 is unbiased. We find that the radial distributions of model satellites are similar to those around comparable primary galaxies in the SDSS DR8, with only slight differences at low luminosities and small projected radii. However, when splitting the satellites by colour, the model and SDSS satellite systems no longer resemble one another, with many red model satellites, in contrast to the dominant blue fraction at similar luminosity in SDSS. The few model blue satellites are also significantly less centrally concentrated in the halo of their stacked primary than their SDSS counterparts. The implications of this result for the GALFORM model are discussed.

5.1 Introduction

While the standard Λ Cold Dark Matter (ΛCDM) model has been shown to be in good agreement with observations of large scale structure, the verification of this model at small, galactic scales remains less certain. One reason for this is the increased importance of astrophysical processes relative to gravity in this strongly non-linear regime. The study of the properties and distribution of galactic satellite galaxies provides an opportunity to test ΛCDM on small scales while also constraining different aspects of galaxy formation models related to the rates at which satellites form stars, become disrupted and merge with the central galaxy.

The construction of large galaxy redshift surveys, such as the Two Degree Field Galaxy Redshift Survey (2dFGRS, Colless et al., 2001), the SDSS (York et al., 2000), the Galaxy and Mass Assembly (GAMA, Driver et al., 2009, 2011) Survey and the Deep Extragalactic Evolutionary Probe 2 (DEEP2, Davis et al., 2003) Survey, has led to the accumulation of external galaxy samples covering large volumes. Many studies of the luminosity function (LF), spatial distribution and kinematics of bright satellites have been carried out using these and even earlier data sets (e.g. Zaritsky et al., 1993, 1997b; van den Bosch et al., 2004; Conroy et al., 2005; van den Bosch et al., 2005; Chen et al., 2006; Koposov et al., 2009b; Busha et al., 2010b; Prescott et al., 2011). The inclusion of a statistical background subtraction in the satellite system estimators has allowed fainter satellites to be studied using deeper photometric galaxy catalogues (e.g Lorrimer et al., 1994; Liu et al., 2008, 2011; Lares et al., 2011; Nierenberg et al., 2011; Tal & van Dokkum, 2011; Jiang et al., 2012; Strigari & Wechsler, 2012; Tal et al., 2012; Wang & White, 2012). By extending the regime over which the satellite distributions have been quantified, a more stringent test of the models can be performed.

In this Chapter, we will test the ΛCDMmodel and the semi-analytic galaxy formation model GALFORM (Bower et al., 2006), by comparing the properties of model galactic satellite systems with those measured from the SDSS DR8 spectroscopic and photometric galaxy catalogues. We will introduce a new series

of GALFORM model galaxy catalogues based on MS-II that will allow us to extend the predictions from the MS to less luminous galaxies.

In Section 2 we describe the SDSS and model galaxy catalogue data that we use, and compare these two data sets. Section 3 contains summaries of the methods we use to select primaries and determine the satellite luminosity function and the projected number density profile. These two satellite galaxy distributions, upon which we will focus in this Chapter, were calculated for the SDSS samples in Chapter 2 and Chapter 3. A verification that our estimators are unbiased is performed using the model galaxy samples. The results of the comparison between model satellite systems and those around similarly isolated SDSS primaries is presented in Section 4. Implications for the model drawn from these comparisons are discussed in Section 5; we conclude in Section 6. Throughout the Chapter we assume a fiducial ΛCDM cosmological model with $\Omega_M = 0.3$, $\Omega_\Lambda = 0.7$ and $H_0 = 70$ km s^{-1}Mpc^{-1} as in Paper I and II. [1]

5.2 Observed and model galaxies

In this section we briefly review the data being used from the SDSS, which were described in more detail in Chapter 2 and Chapter 3, before introducing the procedure to construct mock galaxy catalogues to compare with these data.

5.2.1 SDSS galaxies

Galaxies from both the spectroscopic and photometric samples in the SDSS DR8 are used for this study. Isolated primary galaxies, as defined in Chapter 2 and Chapter 3, are selected from the spectroscopic survey, whereas satellites can come from either the spectroscopic or photometric surveys. With the relatively poorly constrained distances provided by the photometric redshifts, a statistical background subtraction is performed to obtain an estimate of the satellite galaxy

[1] Note that the Millennium and Millennium II simulations have $\Omega_M = 0.25$ and $\Omega_\Lambda = 0.75$. We verified that this slight difference has no significant impact on our results.

population around each of the primaries, as described in Section 5.3 below.

5.2.2 Model galaxies

The model galaxy catalogues were created using a combination of large dark matter simulations to define the mass distribution and a semi-analytic model to place the galaxies within this density field. Either the Millennium Simulation (MS, Springel et al., 2005) or the Millennium-II Simulation (MS-II, Boylan-Kolchin et al., 2009) was used to provide the mass distribution. The former covers a large volume and hence contains many suitable isolated primaries, while the latter traces the mass distribution in a smaller volume, thus resolving structures containing lower luminosity galaxies. While the two simulations trace the same number of particles (10^{10}), the MS and MS-II simulation cubes are 714 Mpc and 143 Mpc long respectively. The corresponding particle masses are $\sim 1.23 \times 10^9$ $M_\odot$ and 9.9×10^6 $M_\odot$.

The model galaxies populate the dark matter structures according to the galaxy formation model GALFORM (Bower et al., 2006), which includes reionization at high redshift and energy injection from supernovae and stellar winds in order to prevent the overproduction of low luminosity galaxies. The luminosities of the most luminous galaxies are curbed by feedback from AGN. Parameters in the treatment of the galaxy formation processes have been chosen so as to produce as good a match as possible to the observed K band LF of local galaxies. Fig. 5.1 shows the luminosity functions of all galaxies in the MS and MS-II simulation cubes. They match quite well with both the observed r band luminosity function of GAMA galaxies (Loveday et al., 2012) shifted to $z = 0$ by applying the offset $r = {}^{0.1}r - 0.22$ (Blanton et al., 2005), and the LF from the SDSS (Blanton et al., 2005). The drop in the MS LF at low luminosities reflects the resolution limit, which corresponds roughly to $M_r = -16$. Galaxies placed into the MS-II should be complete significantly beyond this and thus suitable for studying faint satellites.

For the MS, in addition to having the GALFORM model galaxies populating the simulation cube, flux-limited light-cone mock catalogues, either with or

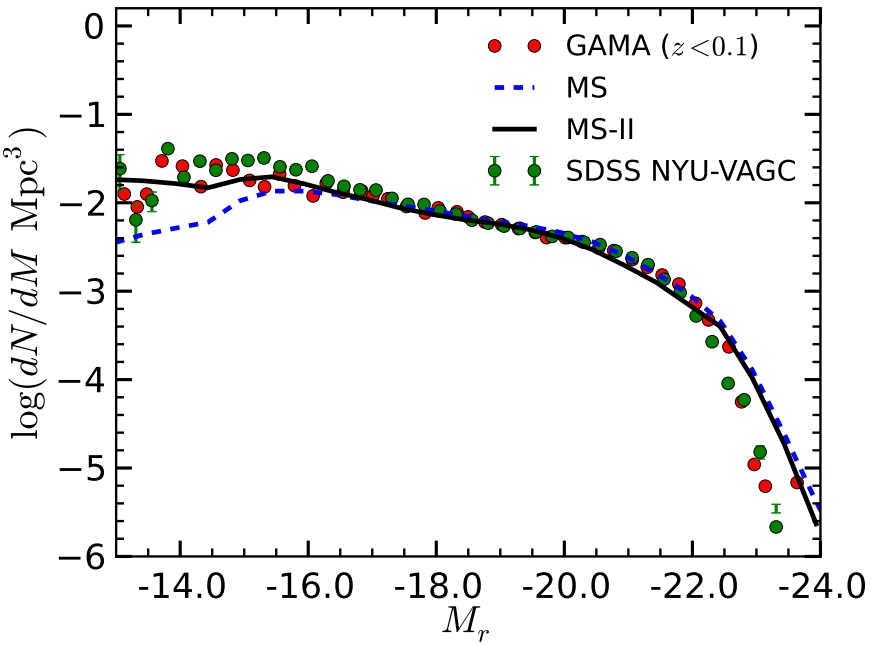

Figure 5.1: The luminosity functions of all galaxies in the MS (blue dashed line) and MS-II (black solid line) cubes compared with observed luminosity functions of galaxies in the GAMA survey (the $z < 0.1$ subset from Loveday et al. 2012, red points) and SDSS (Blanton et al. 2005, green points). The observed luminosity functions are k-corrected (SDSS) or shifted (GAMA) to $z = 0$.

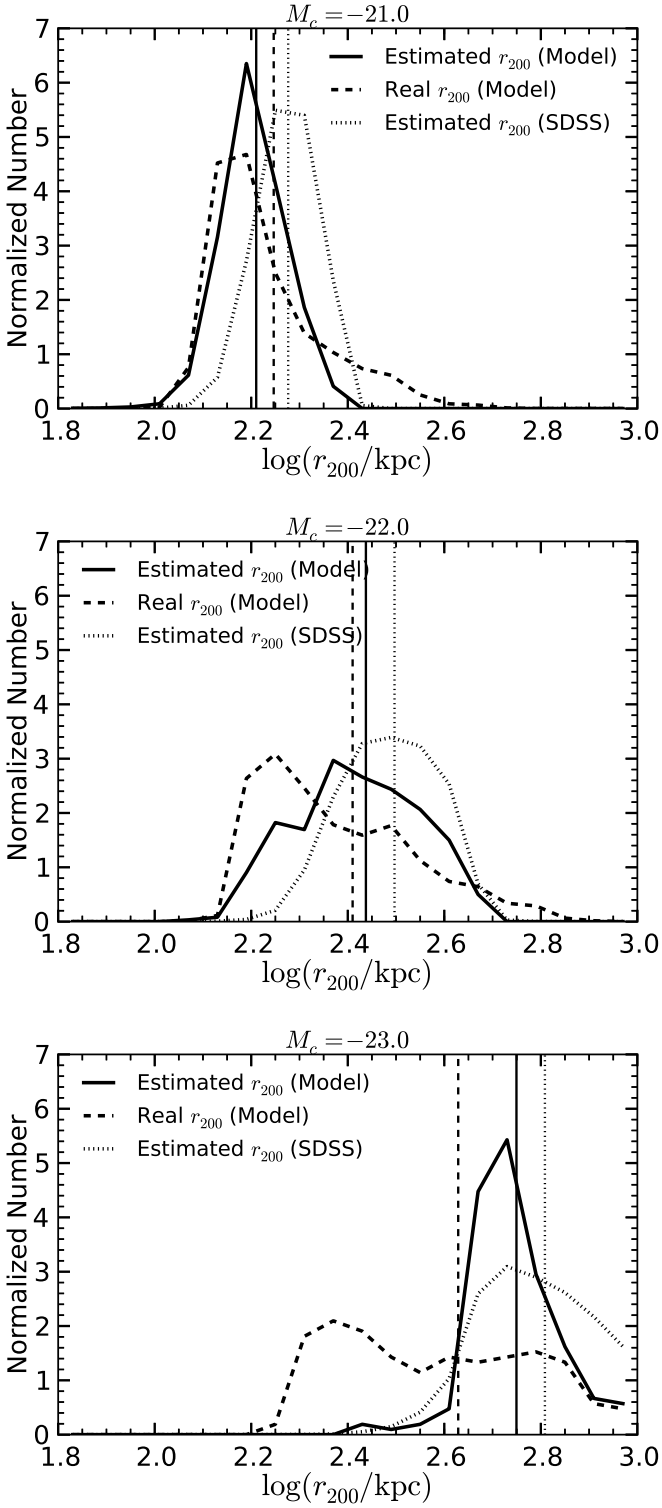

Figure 5.2: The distribution of estimated r_{200} values for model primary galaxies (solid lines), real r_{200} values for their associated parent haloes (dashed lines) and estimated r_{200} values for primaries selected from the SDSS (dotted lines). (Continued on the following page.)

Figure 5.2: (continued) From top to bottom, the panels show results for primary magnitude bins centred on $M_c = -21.0, -22.0$ and -23.0 respectively. The vertical lines are the means of the corresponding distributions.

without the peculiar velocity included in the line-of-sight 'redshift', have also been constructed (Merson et al., 2012). These galaxies cover the redshift range $z = 0.0 - 2.0$. To simulate the photometric redshifts and their uncertainties in the SDSS DR8 catalogue, we assign a photometric redshift with an uncertainty to every galaxy that is fainter than $m_r = 17.7$. The assigned photometric redshift is generated by adding a Gaussian-distributed random redshift error to the accurate redshift of the model galaxy. The width of the error distribution is a function of redshift, and is determined by fitting to SDSS galaxies that have both spectroscopic and photometric redshifts. Photometric redshift uncertainties are also drawn from a Gaussian random distribution with median and scatter determined empirically from the SDSS data. Including an empirically-determined colour dependence into the size of the photometric redshift errors did not significantly change our results.

Using both the MS and MS-II cubes of galaxies, we can test how robust our results are to the numerical resolution of the dark matter simulations. Comparison of the results obtained from the MS cube with those obtained from the light-cone mock catalogue, provides a test of the accuracy of our background removal and satellite distribution estimation procedures. Finally, the light-cone mock catalogue is intended to mimic the SDSS survey and provide a direct test of the model.

When calculating scaled satellite number density profiles, it is necessary to determine the value of r_{200} (defined as the radius enclosing a mean total overdensity of 200 times the critical cosmic value) associated with each primary galaxy. Following Chapter 3, r_{200} is estimated from the stellar mass, inferred from the luminosity and colour of the primary. This is converted to a halo mass, M_{200}, using the abundance matching technique of Guo et al. (2010), from which r_{200}

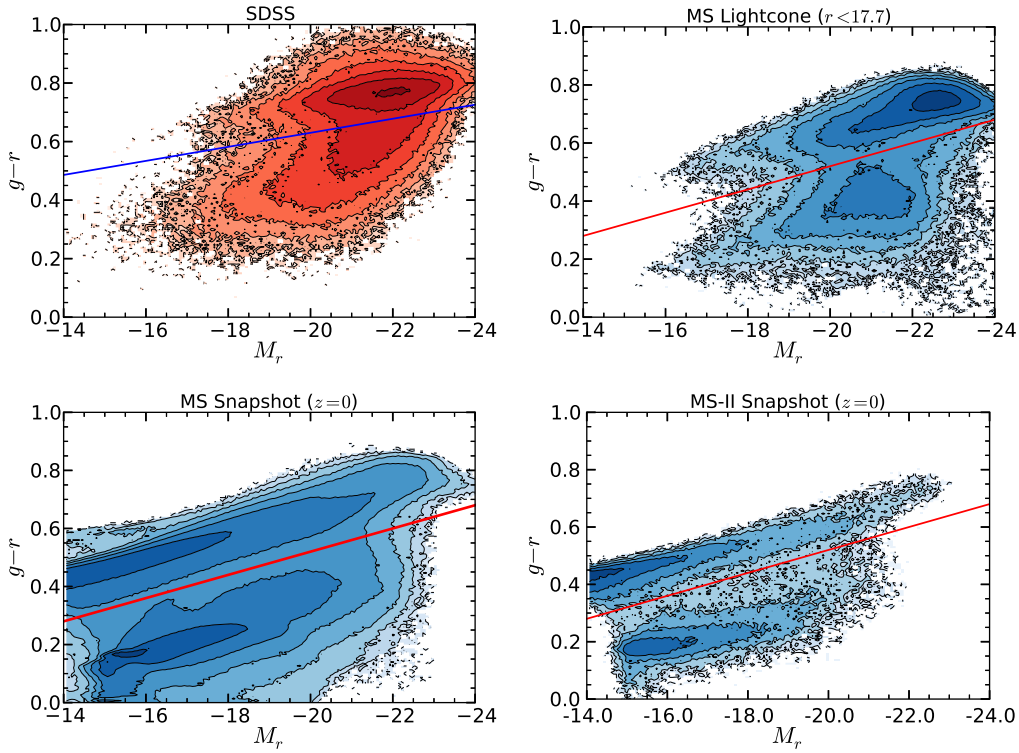

Figure 5.3: Colour-magnitude diagrams of spectroscopic galaxies in SDSS (top left) and of galaxies in the MS mock light-cone (top right) and the two different simulation cubes (MS, bottom left and MS-II, bottom right). Contours represent lines of constant galaxy number density and the straight lines indicate the colour cuts used to define red and blue primaries. The same cut is used for both the MS and MS-II.

follows. The solid and dotted lines in Fig. 5.2 trace the distributions of r_{200} estimated from the MS and SDSS primaries respectively, with the different panels showing results for different luminosity primaries. Vertical lines show the mean values of the distributions, which differ by no more than about 15 per cent in all cases. This similarity between estimated satellite system sizes in the mock and SDSS suggests that scaling the satellite number density profiles by the system size should not create any large systematic differences between the real and mock results.

The distributions of real r_{200} values, inferred from the dark matter distribution in the simulation cube, are shown with dashed lines in Fig. 5.2. For the lower luminosity primaries, the real and estimated r_{200} distributions are similar. However, in the bottom panel of Fig. 5.2 it is apparent that there is a significant population of physically small haloes surrounding primary galaxies whose stellar mass corresponds to a larger halo. As pointed out in Chapter 3, this is probably due to the fact that the stellar mass varies little with halo mass for these most luminous systems. Thus, any small scatter in stellar mass gives rise to a large change in the value of r_{200} inferred from abundance matching. This is an important source of potential bias when trying to measure concentrations of satellite distributions around the most luminous primaries. In this case, a concentration derived using the value of r_{200} estimated from stellar masses will not necessarily reflect the concentration as defined with respect to the halo mass.

Finally, as we will be investigating the colour dependence of the results, in Fig. 5.3 we compare the colour distributions of galaxies in the SDSS and model galaxy catalogues. The distribution of SDSS galaxies in the colour-magnitude diagram is shifted along the $g-r$ axis compared to that of the model galaxies (see also González et al., 2009). Recreating the model colour-magnitude without including dust extinction has little impact on this difference between model and SDSS colours. Thus, while we choose ${}^{0.0}(g-r)^{\rm SDSS}_{\rm cut} = 0.15 - 0.024M_r$ as the line dividing the red and blue populations in the SDSS this boundary is placed at ${}^{0.0}(g-r)^{\rm MS,MS-II}_{\rm cut} = -0.28 - 0.04M_r$ for the model galaxy populations. These cuts are shown in the 4 panels of Fig. 5.3, where the effect on the colour mag-

nitude distribution of including the survey flux limit can be seen for the MS. This removes the bulk of the low luminosity galaxies that are present in the $z = 0$ snapshot and makes the resulting light-cone galaxy population significantly more like that in the SDSS. The fraction of the $-21 < M_r < -19$ model light-cone galaxies that are defined as red is 0.51, the same as that for the SDSS. Had we adopted the SDSS colour cut, the model would only have had a red galaxy fraction of 0.28. For galaxies in the magnitude range $-20 < M_r < -19$, the red fractions are 0.46 and 0.38 for the model and SDSS respectively, when using the cuts shown in Fig. 5.3. Thus, apart from a magnitude-dependent shift in the colours of galaxies, which we can correct for with the different colour cuts, the global red galaxy fractions are quite similar between model and SDSS data sets at magnitudes that we will be considering for the satellite galaxies.

The MS and MS-II simulations, once populated with galaxies according to the semi-analytic model, contain very similar galaxy populations. Thus, it is appropriate to use them interchangeably depending upon which is more important: having a large volume containing many primaries, or being able to resolve low luminosity satellite galaxies. However, if we want to compare results from the MS-II cube of galaxies with those from the SDSS flux-limited survey, then we still need to demonstrate, using the MS, that our methods recover from the light-cone mock surveys the same satellite distributions as are present in the simulation cubes.

5.3 Method

In this section we briefly review the procedure used to determine the satellite LF and projected number density profile for SDSS, described more fully in Chapter 2 and Chapter 3, before detailing how these distributions are determined from the various different types of model galaxy catalogue. The quality of the recovery of these distributions is quantified by comparing those determined from the MS cube of galaxies with those from the flux-limited mock light-cone surveys.

Primary galaxies are selected to have spectroscopic redshifts in the SDSS and to have magnitudes, M_p, satisfying $M_c - \Delta M_{bin} < M_p < M_c + \Delta M_{bin}$. We choose $M_c = -21.0, -22.0, -23.0$ and $\Delta M_{bin} = 0.5$. Further, the primaries should be isolated in the sense that no other galaxy within $\Delta M_{faint} = 0.5$ magnitudes lies within a projected distance of $2R_{inner}$ and is sufficiently close in redshift. 'Sufficiently close' is defined as a difference in spectroscopic redshift of less than $\Delta z_s = 0.002$ or, for galaxies without a spectroscopic redshift, with a photometric redshift within $\alpha_p \sigma_p^*$, where $\alpha_p = 2.5$ and σ_p^* is the photometric redshift error defined in Chapter 3 II. R_{inner} represents the projected radius within which satellites may reside, and the variable R_{outer} defines the outer edge of an annulus within which the local background is estimated. We adopt the same values of (R_{inner}, R_{outer}) as in Chapter 3: $(0.3, 0.6), (0.4, 0.8)$ and $(0.55, 0.9)$ Mpc for primaries in magnitude bins $M_c = -21.0, -22.0$ and -23.0 respectively. Only galaxies brighter than $m_r^{lim} = 20.5$ are considered.

Only sufficiently close galaxies in redshift space are included when counting the potential satellites within the projected radius R_{inner} and making the local background estimate from the surrounding annulus out to R_{outer}. The background-subtracted satellite systems are stacked for primaries in each absolute magnitude bin to provide estimates for the mean satellite LFs and projected number density profiles of satellites more luminous than a particular absolute magnitude, as described more fully in Chapter 2 & 3.

The procedure described above is applied to the SDSS itself and also to the MS redshift space light-cone mock catalogue. However, different estimation procedures are used for the light-cone mock with real space (rather than redshift space) galaxy coordinates and the galaxy populations in the simulation cubes. With the real space positions, it is possible to define isolated primaries as having no bright neighbours within a sphere of radius $2R_{inner}$. The satellites within a sphere of radius R_{inner} can also be determined without any need for background subtraction. Using only the real space satellites, the estimation of the satellite luminosity function is straightforward. For the jth magnitude bin, the average satellite LF is estimated using

$$\overline{N}_j^{\text{real sat}} = \frac{\Sigma_i N_i^{\text{real sat}}(M_j)}{N_j^{\text{real prim}}}, \tag{5.3.1}$$

where $N_i^{\text{real sat}}$ is the number of satellites around primary i and $N_j^{\text{real prim}}$ is the number of primaries contributing to the jth bin of the LF.

While we need no correction for interlopers in real space, the process of estimating the mean projected number density of satellite galaxies is such that a fair comparison with light-cone data still requires the subtraction of a background estimated from an outer area. Hence, the projected number density profiles of satellites brighter than M^{trun} in real space are determined using all galaxies within a cylinder of projected radius R_{outer} and length $2R_{\text{outer}}$, centred on the primary. These galaxies are projected onto a plane and provide the sources for the potential satellites/background for projected radii less/greater than R_{inner}. The projected number density profile is determined using

$$\overline{\Sigma}_i(r_j^{\text{ann}}) = \frac{\sum_i N_{ij}(M^{\text{trun}})}{\sum_i A_{ij}^{\text{p}}} - \frac{\sum_i N_i^{\text{bck}}}{\sum_i A_i^{\text{outer}}}, \tag{5.3.2}$$

where N_{ij} is the number of galaxies brighter than M^{trun} within a projected distance R_{inner} of the ith primary and in the jth projected annulus, and N_i^{bck} is the corresponding number of galaxies in the projected outer annulus, $R_{\text{inner}} < r < R_{\text{outer}}$. A_{ij}^{p} is the area contributed by the ith primary to the jth annulus for the detection of satellites brighter than M^{trun},

$$A_{ij}^{\text{p}}(M^{\text{trun}}) = \begin{cases} A_{ij} & M^{\text{trun}} < M_i^{\text{lim}} \\ 0 & M^{\text{trun}} > M_i^{\text{lim}} \end{cases}, \tag{5.3.3}$$

where A_{ij} is the area of the jth annulus surrounding the ith primary and M_i^{lim} is the absolute magnitude that corresponds to the apparent magnitude limit of the mock catalogue. A_i^{outer} is the corresponding area in the outer annulus surrounding the ith primary.

The comparison of the projected number density profiles, before and after background subtraction, with that formed by simply projecting the galaxies within a sphere of radius R_{inner} of the primary galaxy is shown in Fig. 5.4. The results indicate that the projected profile after subtracting the background

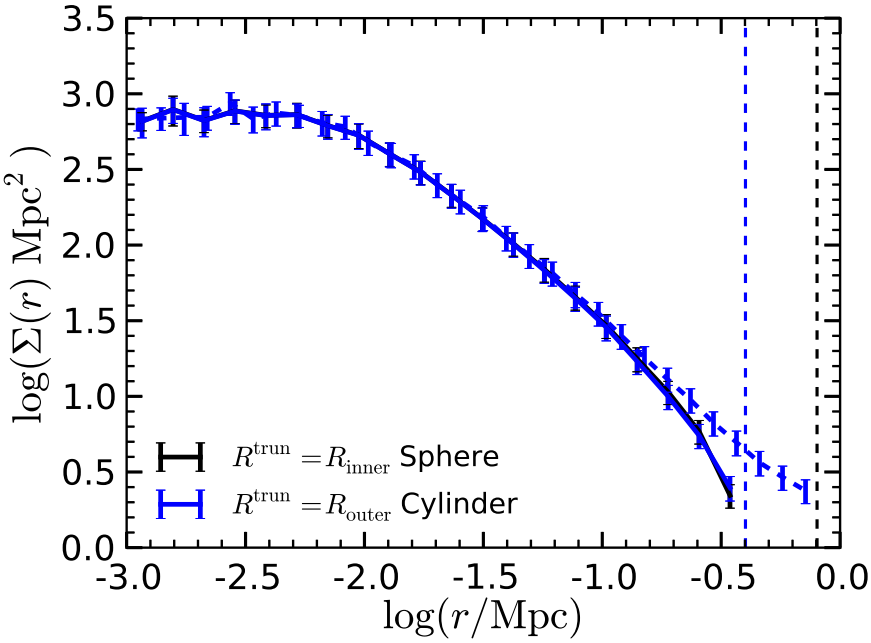

Figure 5.4: The comparison of real space projected number density profiles estimated by different methods. The black line is the profile estimated by projecting the satellites within spheres of radius R_{inner} around primaries. The dashed blue curve shows the projected number density profile of all galaxies within a line-of-sight distance R_{outer} of a primary. The solid blue curve is the background-subtracted case, where the background is estimated from the outer annulus with $R_{\mathrm{inner}} < r < R_{\mathrm{outer}}$. Vertical dashed lines show R_{inner} and R_{outer}.

very accurately recovers that estimated directly from the galaxies within the inner area ($r < R_{\mathrm{inner}}$). The impact of the background subtraction is small and limited to radii near to R_{inner}. This establishes that the method for calculating the background subtracted projected number density profile from a real space light-cone survey provides an unbiased estimate of that produced when only satellites within a 3D distance R_{inner} are used. We can now compare these real space profiles with those from redshift space light-cones.

Having described the three different types of model galaxy catalogues made using the MS and how the satellite distributions are determined from each of

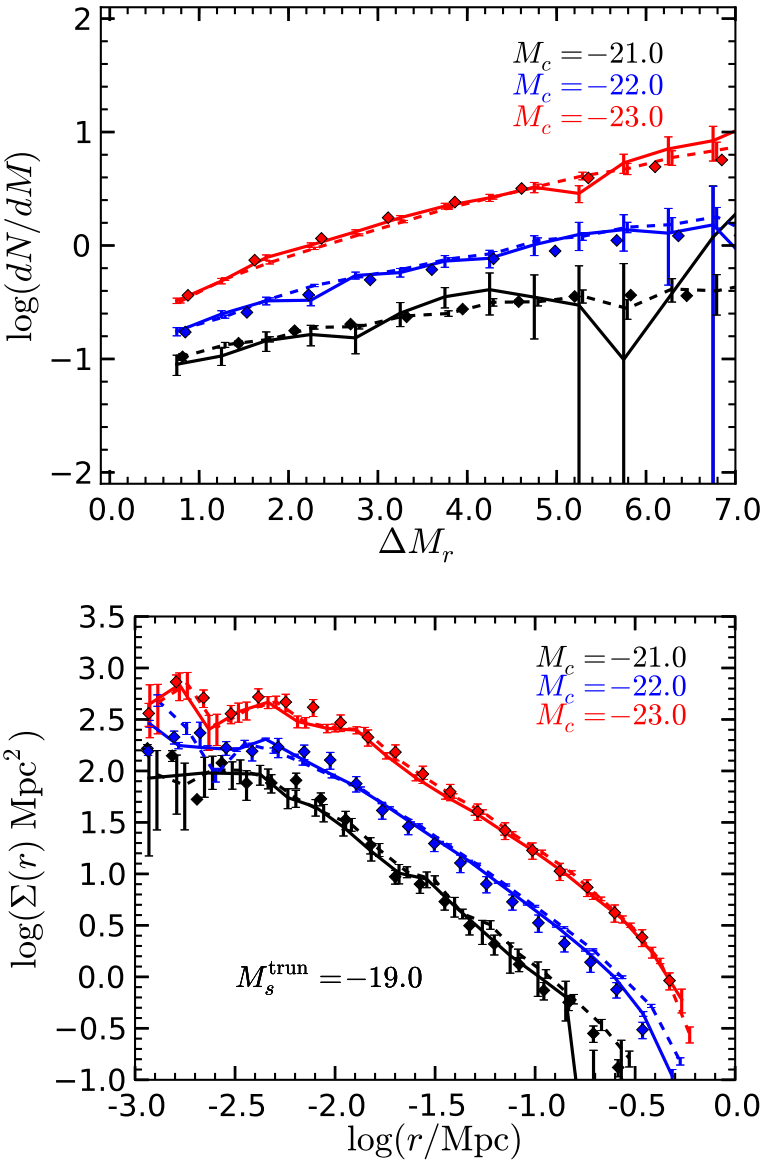

Figure 5.5: Satellite LFs (top) and number density profiles (bottom) estimated from light-cone mock catalogues and directly from the MS cube. The results for primary magnitude bins centred at $M_{\rm c} = -21.0, -22.0, -23.0$ are shown in black, blue and red respectively. Solid and dashed lines correspond to results from redshift and real space light-cones respectively, whereas the points show the results for the whole volume in the simulation cube.

them, we are now in a position to test the accuracy of our estimation procedure. Fig. 5.5 shows the satellite LF and projected number density profiles estimated from each of the model galaxy catalogues: simulation cube, real space light-cone and redshift space light-cone. The agreement between the two different satellite distributions measured from all three catalogues at $M_c = -21.0, -22.0$ and -23.0 provides strong support that our results are unbiased, and that our technique for background subtraction is appropriate. Given that the isolated primaries are a specially selected subset of the differentially clustered galaxy population, one would expect that a local, rather than global, background subtraction would be appropriate. The fact that the results from the MS light-cone mock match well with those from the MS cube of galaxies suggests that we can use results from the MS-II simulation cube at $z = 0$ when comparing with low luminosity galaxies in the SDSS DR8.

5.4 Results

Having verified that the model galaxies have similar distributions of luminosity and colour to those in the SDSS and that our local background subtraction procedure produces unbiased estimates of the satellite LF and projected number density profile, we now compare the model and observed satellite systems in more detail.

5.4.1 Dependence on primary and satellite luminosity

The top panel of Fig. 5.6 shows the satellite LFs for the primary magnitude bins $M_c = -21.0, -22.0, -23.0$ estimated from both the SDSS and MS-II mock data. For $\Delta M_r < 5$, the model and SDSS satellite luminosity functions generally agree well. However, there is a steepening of the LF for lower luminosity satellite galaxies in the SDSS that is not present in the model. The MS-II was used for this comparison, so a lack of numerical resolution should not be responsible for this deficit.

The middle panel of Fig. 5.6 shows the projected number density profiles of

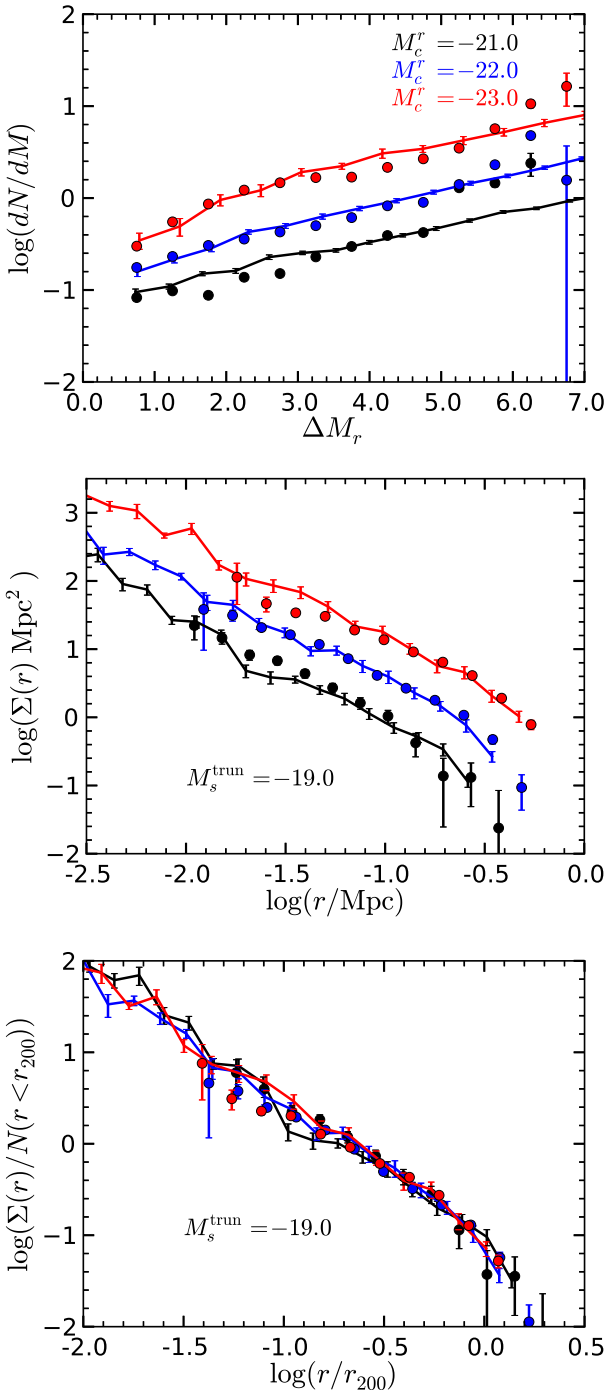

Figure 5.6: Model (MS-II, solid lines) and SDSS (points) satellite LFs (top), projected number density profiles (middle) and normalized profiles (bottom). The results for primary luminosity bins $M_{\rm c} = -21.0, -22.0, -23.0$ are shown in black, blue and red, respectively.

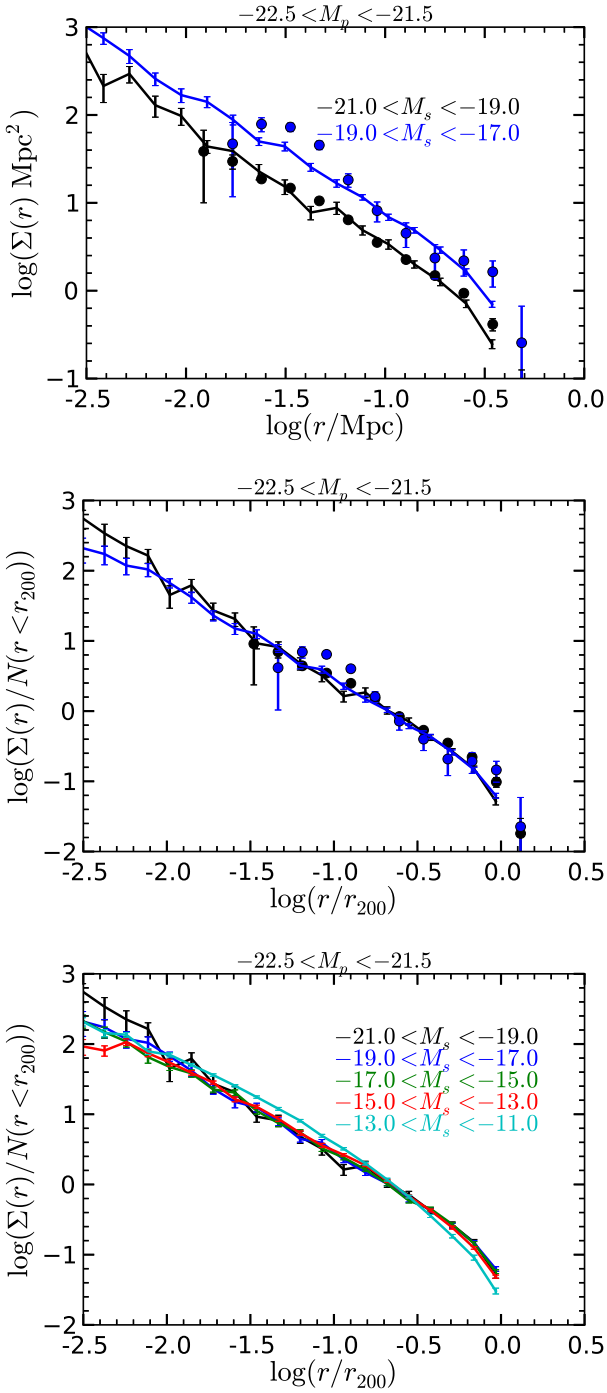

Figure 5.7: The dependence of the scaled and unscaled satellite density profiles on satellite luminosity for primaries in the range $-22.5 < M_\mathrm{p} < -21.5$. Unscaled (top) and scaled (middle) profiles of satellites are shown for two different luminosity bands: $-21.0 < M_s < -19.0$ (black) and $-19.0 < M_s < -17.0$ (blue). (Continued on the following page.)

Figure 5.7: (continued) The solid lines and points correspond to results from the model and SDSS respectively. The bottom panel shows scaled profiles for lower luminosity satellites in the model.

satellites brighter than $M_{\rm sat}^{\rm trun} = -19.0$ for the different primary samples. This limit is chosen, following Chapter 3, to ensure that the profiles for different luminosity bins are measured from a large enough sample. In all cases the profile approximately follows $\Sigma(r) \propto r^{-1.5}$, with the amplitude reflecting the fact that more luminous primaries host more satellites. For most radii, the model reproduces the amplitude observed in SDSS. In detail though, there is a factor 2 difference at ~ 30 kpc for both $M_{\rm c} = -21.0$ and -23.0. The model underproduces satellites at this radius for the least luminous primaries and overproduces them for the most luminous primaries.

Once rescaled in both radius and projected number density, as shown in the bottom panel of Fig. 5.6, the model and SDSS profiles line up well outside the region at $0.05 \lessapprox r/r_{200} \lessapprox 0.1$. As noted in Chapter 3, the slight deficit of satellite galaxies in the inner regions of the SDSS for $M_{\rm c} = -23.0$ primaries, relative to the model, may reflect difficulties identifying low luminosity satellites in regions where the background light subtraction is significant (Aihara et al., 2011). This had the effect of slightly decreasing the fitted concentration of satellites around the most luminous primaries relative to the low luminosity primary bins.

The dependence of the satellite projected number density profile on satellite luminosity for primaries with $-22.5 < M_p < -21.5$ is shown in Fig. 5.7. Satellites are split into two bands of luminosity: $-21.0 < M_s < -19.0$, representing the objects that contributed to the profile in Fig. 5.6, and $-19.0 < M_s < -17.0$, showing the behaviour of lower luminosity satellites. The top and middle panels show the satellite projected number density profiles before and after scaling respectively. While generally in good agreement, there is an excess of lower luminosity satellites in the SDSS relative to the model at ~ 30 kpc.

The 'bump' in the projected number density profile in the SDSS data is present only for the lower luminosity satellites. One is therefore tempted to ask

if it is present at any satellite luminosity in the mock catalogues. This question is answered in the bottom panel of Fig. 5.7, where no comparable deviations are seen for satellites with $M_s < -13$, which have indistinguishable profiles from those of brighter satellites. The profile for satellites with $-13 < M_s < -11$ shows a slight change in shape over a large range of scales relative to the other sets of satellites, but nothing as pronounced as is seen in the SDSS.

5.4.2 Dependence on primary and satellite colour

As a further test of the galaxy formation model, which has so far largely succeeded in reproducing the satellite LF and projected number density distributions, we now split the primaries and satellites by colour using the slightly different colour cuts described in Section 5.2.2 for the model and SDSS.

Fig. 5.8 shows how the satellite luminosity function and projected number density profile depend upon the colour of the primary around which they are being measured, and compares the results from the model and the SDSS for primaries with $-22.5 < M_p < -21.5$. For the adopted colour cuts, the vast majority of primaries are classified as red in both the model and SDSS. Given that when not split by colour the model produces a good match to these satellite distributions, it is no surprise that the satellite populations around red primaries agree well between model and observations. However, the blue primaries in the mock catalogues are deficient in satellites by a factor of $2-3$. The excess satellites around SDSS primaries span the range of luminosities and radii being considered here, with a slight tendency to be at lower luminosity and nearer to the primary than for the satellites present around the model primaries. The scaled profiles in the bottom panel of Fig. 5.8 show that satellites around blue SDSS primaries are slightly more concentrated than those around model primaries.

In the top two panels of Fig. 5.8 results for both the MS and MS-II are shown. Because of its limited resolution the LF in the MS becomes incomplete at $\Delta M \sim 5.5$, but the LF in the MS-II is well resolved down to $\Delta M \sim 7$. On the other hand, in the smaller volume of the MS-II, there is a relatively small number of primaries and, as a result, the projected number density profile of satellites

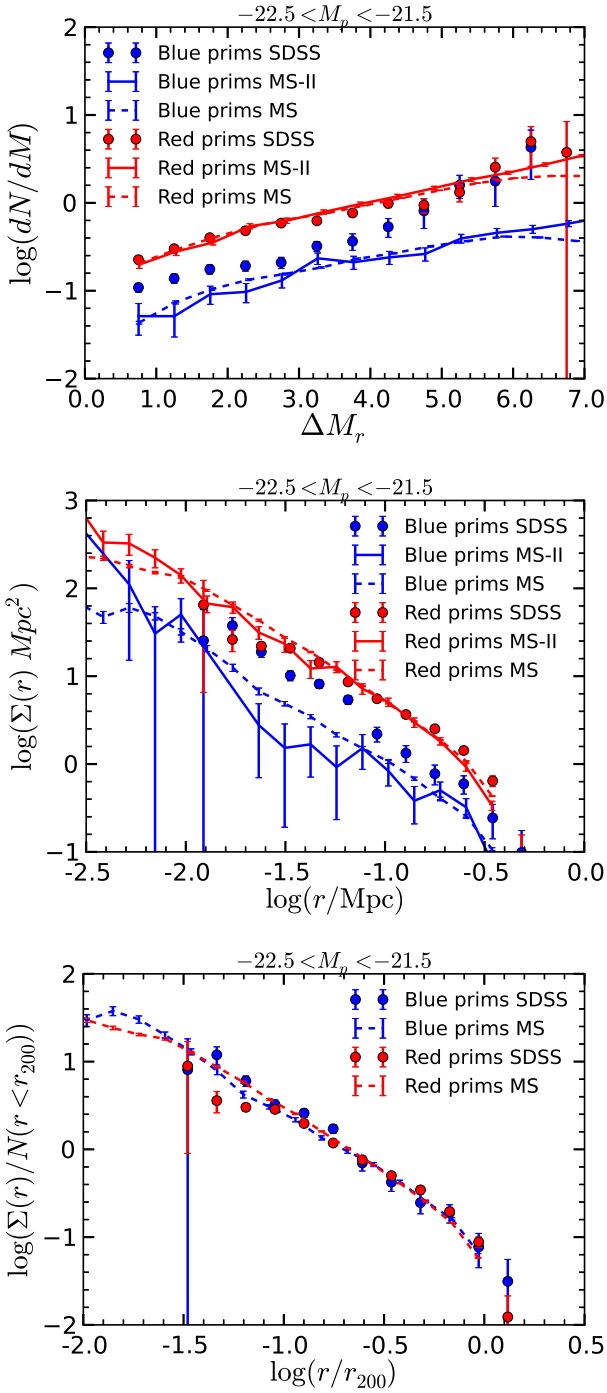

Figure 5.8: The dependence on primary galaxy colour of the satellite LF (top), unscaled (middle) and scaled (bottom) number density profiles for primary galaxies of magnitude $-22.5 < M_p < -21.5$. Solid and dashed lines show model results for primaries in the MS and MS-II respectively, whereas the points are for SDSS. All profiles are for satellites more luminous than $M_s = -19.0$.

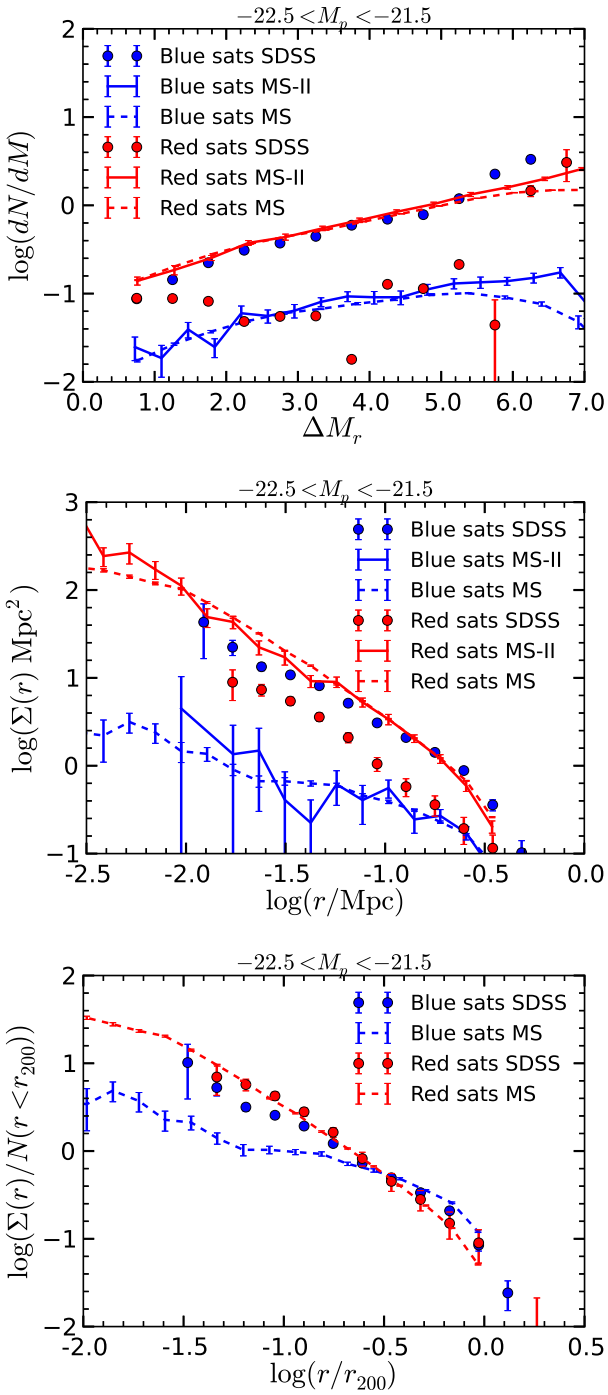

Figure 5.9: Dependence of satellite distributions on the colour of the satellite galaxy. Symbols and line types have the same meaning as in Fig. 5.8.

brighter than $M_s = -19$ is noisy (and it is therefore omitted in the lower panel of the figure). In the regions where both simulations are well resolved and sampled, their results are consistent.

The satellites themselves can be divided into red and blue subsets and their distributions around primaries with $-22.5 < M_p < -21.5$ are shown in Fig. 5.9. Once again both MS and MS-II results are shown in the top two panels, while the noisy MS-II results are not presented for the scaled projected number density profiles in the bottom panel. The fact that the colour cuts in the model and SDSS samples yield completely different red and blue fractions is immediately apparent in the satellite LFs, with the model satellite systems dominated by red satellites to a coincidentally similar extent as the blue satellites dominate around SDSS primaries. For the most luminous satellites, the SDSS blue and red fractions converge, whereas this does not happen for the model.

The shape of the projected density profiles of red satellites are very similar for the model and SDSS systems, once the difference in amplitude has been scaled away, as shown in the bottom panel of Fig. 5.9. However, this is not the case for the blue satellites, which have a much less concentrated distribution around model primaries. For real systems of blue satellites, the distribution is only slightly less concentrated than it is for the red satellites.

5.5 Discussion

The comparison of galactic satellite systems in the model with those in the SDSS shows that the dependence of the satellite distributions on primary and satellite luminosity is captured quite well by the GALFORM model. This is a non-trivial success of the model since its parameters were adjusted merely to match the global K-band LF of galaxies, with no direct reference to satellite systems. There is an excess of very low luminosity satellites around SDSS primaries relative to the model, and the projected number density profiles are up to a factor 2 discrepant within ~ 30 kpc, but the agreement is generally good.

Tal et al. (2012) also studied the radial distribution of satellite systems around bright primary galaxies using SDSS data. Their primaries were LRGs at $0.28 < z < 0.40$ with no isolation criteria applied and hence often in groups of bright galaxies, and thus are different to those studied here in a few respects that may well be important. They found the projected number density was well fitted by a combination of a projected NFW profile (Navarro et al., 1996, 1997) for large radii and a central steeper profile that follows the stacked light profile of the LRGs. This central bump is similar to that seen for the lower luminosity satellites around primary galaxies shown in Fig. 5.7, but is, in contrast, most apparent in the high luminosity satellites around the LRGs.

The differences between the model and SDSS satellite systems are greater when the colour of the satellites is considered. Even the distribution of galaxies in the colour-magnitude plane shows that the model has too high a fraction of low luminosity red galaxies relative to the SDSS. The model blue satellites are both significantly depleted and very much less concentrated relative to either blue or red SDSS satellites, which have a projected number density profile like that of the red model satellites. These pieces of evidence point to the model being too ready to convert low luminosity blue galaxies to red ones.

Weinmann et al. (2012) suggest that galaxy formation models have a generic problem with maintaining sufficient gas to form stars in lower mass galaxies at low redshift. The satellite galaxies we are considering are somewhat larger than those studied by Weinmann et al. (2012), and our choice of different colour cuts for defining red and blue galaxies in the model and SDSS samples reduces global systematic colour differences. For instance, the overall fraction of blue galaxies in the model, at the magnitudes of the satellites that we focus on, is very similar to that in the SDSS. Satellite galaxies in our study constitute only a small fraction of the total population of galaxies. Thus, a dramatic change in the satellite properties will leave very little imprint on the global LF.

Alternatively, it could be that semi-analytical galaxies turn red too rapidly after accretion into larger haloes. This idea was investigated by Font et al. (2008), who changed the GALFORM treatment of gas stripping from subhaloes as they

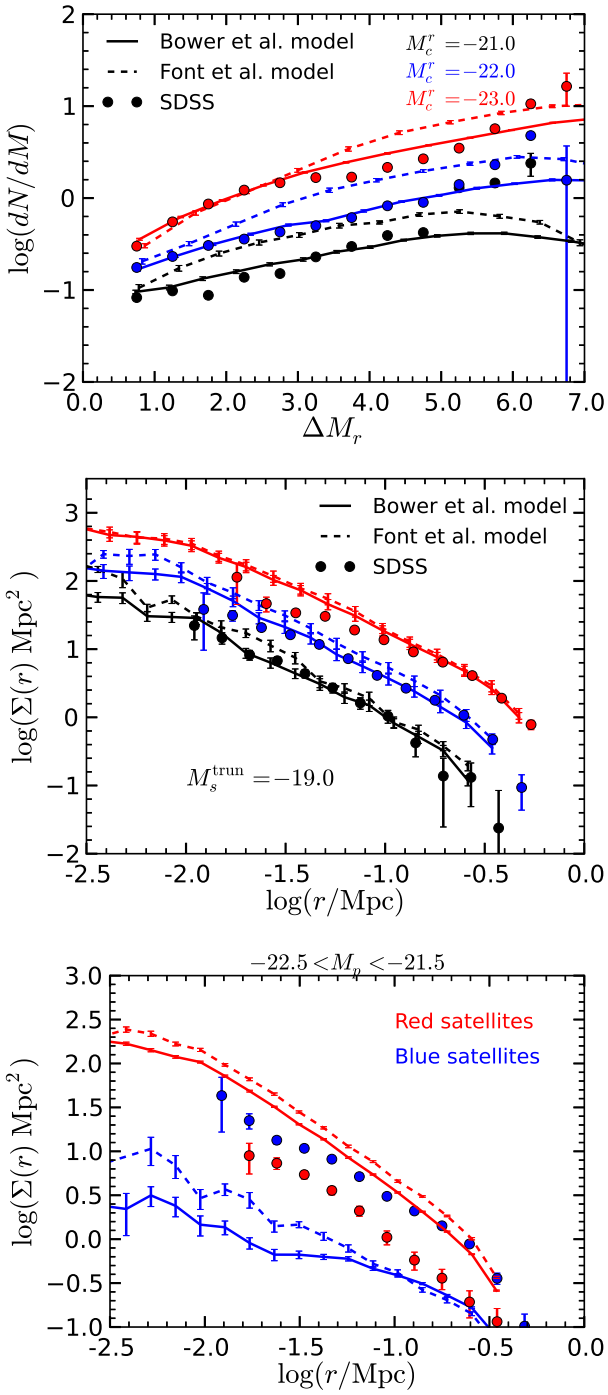

Figure 5.10: The effect on the model satellite LF (top) and number density profiles (lower two panels) of changing the treatment of hot gas stripping in GALFORM for primary galaxies of magnitude $-22.5 < M_p < -21.5$. (Continued on the following page.)

Figure 5.10: (continued) The points are the results measured from SDSS data, whereas solid and dashed lines are the results measured from catalogues constructed using the Bower et al. (2006) and Font et al. (2008) GALFORM models respectively. The middle panel shows the profiles of all satellites, whereas the lower panel shows them split by colour.

enter the virial radius of large primary galaxies. Rather than hot gas being stripped from subhaloes immediately as they enter the virial radius, a more gradual loss of gas is adopted in the Font et al. (2008) model. This allows a relatively extended period of star formation occurs and the possiblity of bluer satellites. We have performed our analysis on a model galaxy population constructed using this particular variant of the Bower et al. (2006) GALFORM model. While the typical colours of galaxies do become slightly bluer, the number of blue satellites per primary in the Font et al. (2008) model increases only slightly, as can be seen in Fig. 5.10. The shape of the blue satellite profile improves significantly, with the extra blue satellites being found preferentially at small radii. However, the abundance of red satellites is also increased by this modification to the GALFORM model, because satellites generally become more luminous as a result of the more extended period of star formation. As a result, the Font et al. (2008) model overproduces satellite abundances overall, as shown in the upper two panels of Fig. 5.10. The overproduction is most discrepant with the data at low luminosities.

Many important astrophysical processes combine to determine the distribution of low luminosity galaxies. Therefore the distributions of satellite galaxies will depend sensitively on aspects of the galaxy formation model. Given that the treatment of gas stripping can have the large impact shown in Fig. 5.10, one is drawn to conclude that the ability of the default Bower et al. (2006) model to match the total satellite LF and projected number density profile of the SDSS systems was far from inevitable.

5.6 Conclusions

Using model galaxy catalogues constructed using large dark matter simulations and a semi-analytic galaxy formation model, we have tested the accuracy of our procedures for measuring properties of the distribution of satellite galaxies around bright, isolated primary galaxies. We find that our local estimation of the abundance of background galaxies yields unbiased estimates of the satellite galaxy luminosity function and projected number density profile. The agreement between results in the MS and MS-II galaxy catalogues in their region of overlap shows that our results are numerically converged and allows us to extend the dynamic range of the model predictions.

Comparing the model predictions with those measured for satellite systems in the SDSS, we find that the dependence of the satellite LF is matched well for $M_c = -21.0, -22.0, -23.0$ and $\Delta M_r < 5$. Lower luminosity satellites are increasingly underpredicted by the model. The projected number density profile is also well reproduced at radii greater than ~ 30 kpc. At smaller radii, deviations in the abundance by a factor of two are apparent. These differences between model and SDSS are seen most strongly in the low luminosity satellites, which show an excess in the SDSS relative to the extrapolation of the power law from larger radii, which describes the inner regions of the model satellite systems.

Splitting the sample into red and blue galaxies produces more dramatic differences between the model and SDSS results. The model places a factor $2-3$ fewer satellites around blue primaries than are present around comparable SDSS primaries. However, the discrepancy between model and SDSS is even larger when considering the colours of the satellites. The model satellites are predominantly red, in contrast to the blue-dominated SDSS satellite galaxy population. Furthermore, what model blue satellites there are have a significantly more extended distribution around their primary galaxy than is seen for either the SDSS blue satellites or the red satellites in the model and SDSS.

The generally successful comparison of the GALFORM model with the SDSS data performed here provides a non-trivial validation of the assumptions and

framework of this kind of modelling. At the same time, the failure of the model to account for the observed colour dependence of the satellite properties demonstrates that the model is incomplete and that important physical processes, almost certainly related to the rapidity with which infalling satellite galaxies turn red, are not being faithfully modelled. Since a similar shortcoming is present in the independent model of Guo et al. (2011), this problem seems deep-rooted and is worthy of further investigation.

6 CONCLUSIONS

6.1 Summary

The main aim of this thesis is to study satellite galaxies, which can be used to test cosmological models and galaxy formation models. With more and more upcoming galaxy surveys, studies of galactic satellites will become increasingly important. We will be able to understand more details of galaxy formation, and possibly constrain the properties of dark matter. This thesis developed a method of selecting and stacking isolated satellite systems, which enable us measure the statistical properties of isolated satellite systems and compare them with predictions of galaxy formation models.

Chapter 1 gives a brief overview of how galaxies form, based on the ΛCDM model. Structures were seeded by quantum fluctuations at very early stages, then they grow due to gravity. Finally, they collapse and form bound objects, dark matter haloes, which cradle the observed galaxies. Galaxies falling into bigger structures can survive there as satellite galaxies.

In Chapter 2 and Chapter 3, we describe the method we developed to select isolated primaries and their satellites. Using this method, we selected a large sample of isolated primaries, then measured the mean luminosity function and radial density profile of the satellites. Firstly, we find the satellite LFs do not have a Schechter function form. The amplitude of the satellite LF increases with the luminosity of the primary. And the amplitude of the satellite LF varies with the colour and morphological type of the primary. In the range of $1.0 < \Delta M < 8.0$,

blue satellites around the isolated primaries are more abundant than the red satellites. Secondly, we find the radial number density profiles of satellites measured from the SDSS in general can be well fitted by projected NFW profiles, apart from the faintest satellites, for which there is a slight excess at small projected distance. We also show that the concentration of the NFW fits decrease systematically with increasing satellite luminosity and are almost independent of the luminosity of the primaries, The profiles are also dependent on the colour of their primaries and the colour of the satellites themselves. These results have been published in Guo et al. (2011, 2012).

In Chapter 4, we compare the two different methods that count satellites in isolated satellite systems. We show that for the SDSS data, the method based on local background subtraction is more robust than the global method for studying the luminosity and spatial distribution of satellites around isolated primaries.

Finally, In Chapter 5, we confront the predictions of the luminosity distribution and spatial distribution for model satellite galaxies with the measurements of real galaxies from the SDSS. The model galaxies are the outputs of semi-analytic models based on the MS and MS-II simulations. We have tested the accuracy of our procedures for measuring properties of the distribution of satellite galaxies around bright, isolated primary galaxies. We find that our local estimation of the abundance of background galaxies yields unbiased estimates of the satellite galaxy luminosity function and projected number density profile. We find, in general, the galaxy formation model, GALFORM can succeed in producing similar luminosity and spatial distribution as we have measured from the SDSS. However the model failed to produce similar fractions of blue satellites as in the real satellite systems from the SDSS, which is worthy of further investigation.

6.2 Further Work

So far, we have built the largest ever sample of satellite systems around isolated primaries using the SDSS DR8 galaxy catalogue. From these samples, we have

found many interesting properties of the satellite galaxies, which cannot be seen in the mock galaxy catalogues. As new galaxy surveys with lower flux limits, e.g. GAMA and Pan-STARRS, come out, we will apply our method to catalogues from these two surveys. And we could also work with catalogues from other deep photometric surveys, e.g., Advanced Large, Homogeneous Area Medium Band Redshift Astronomical (ALHAMBRA-Survey) and The Physics of the Accelerating Universe (PAU). We will be able to measure the properties of fainter satellite galaxies, which will put much tighter constraints on the nature of dark matter, and galaxy formation models. Comparison of measurements from new surveys with our current survey based on the SDSS DR8, will provide us with much needed opportunities to distinguish potential unknown systematics from true signals. In future, the GAMA and Pan-STARRS data will be publicly released. The first release of GAMA data already occurred on 25th June, 2010. These data can be used for other possible studies. For example, GAMA data will eventually incorporate VST and VISTA imaging, which will go significantly deeper than SDSS and UKIRT. The selection of isolated primaries can be improved by using near-IR selection or stellar mass selection. Further, our method itself can be developed and extended. For example, our method can be modified from working with catalogue samples to image data as in Tal & van Dokkum (2011). Their method uses SExtractor and sets a new lower detection threshold of 1σ above the background, which results in the detection of more real fainter galaxies together with a large number of spurious detections of noise peaks in the images. A large number of spurious detections of noise peaks can be cancelled out, in the mean, by subtracting the background, because the background area contains the same statistical rate of false detections. After eliminating the false detections, only the signals of fainter objects remains. Hence, we will be able to detect even fainter objects by working with the image data rather than catalogue samples.

Secondly, from a theoretical perspective, we have already shown that the semi-analytic models are not correct concerning the colour of satellites by comparing results from the models and the observations. With the results from the

SDSS data and possible future survey data, we will further constrain galaxy formation models, especially concerning the processes relating to the colour of faint satellite galaxies. We are also interested in exploring possible improvements to galaxy formation models.

Thirdly, because of the improving accuracy of photometric redshifts, the photometric redshift surveys now exist, e.g. SDSS, Combo-17, MUSYC and Cosmos. More planned surveys, such as DES, LSST, SNAP and Pan-Starrs will follow. One of advantages of many photometric redshift surveys is that they can usually go deeper in multicolour photometry than in spectroscopy. The cost of this is that photometric redshifts are less accurate than the spectroscopic redshifts. Therefore, statistically suppressing the relatively large intrinsic uncertainty becomes important; especially for studies focused on small scales. Our method based on the local background correction has been proven to be a successful way of incorporating the photometric redshift information. We believe that the same idea can be extended to other studies, for example, Tal et al. (2012) studied satellites around LRGs using a method with a similar background correction. Their results show that concentrations of satellites in groups are also dependent on the luminosity of satellites, similar to satellites around the isolated primaries. However in groups the concentrations increase with the increasing luminosity of satellites, while around isolated primaries the concentrations of satellites decrease with increasing satellite luminosity. In their paper the LRGs were taken as the centres of the groups, however that is not true for all groups. It is not easy to directly combine these two studies. Therefore, we hope to provide a unified framework to perform the analysis of the properties of satellite galaxies both in groups and isolated satellite systems. Extending our method to work with groups, while incorporating the photometric redshift information, could be a another way in approaching our objectives. If this proves successful, then the new method together with deeper catalogues from the photometric redshifts would let us analyse the properties of satellites in both groups and isolated systems within the same framework. We anticipate that the results from the new method will provide us with more opportunities and different approaches to

understand galaxy formation, and possibly, the nature of dark matter.

Initially, we will try to develop a new method, which can successfully find groups in spectroscopic redshift space, to find groups in the photometric redshift space (e.g. Botzler et al., 2004). In light of the errors in the photometric redshifts, the groups found in the photometric redshift will typically contain more contaminating galaxies leading to more false groups. To minimize these problems, we shall test and tune the new method on our current full-sky realistic flux-limited mock galaxy catalogues based on the GALFORM model and Millennium I simulation. No matter how the parameters are tuned it is not possible to completely eliminate the contamination caused by the uncertainty in the photometric redshifts. By appropriately choosing and stacking the samples, this method can statistically remove such contamination with small errors. We will carefully compare such a group finding method with traditional group finding methods. Then, under this framework, we will be able to choose and stack the samples from isolated satellite systems to large groups, from deeper photometric redshift catalogues. The studies of satellites within the different environments will definitely improve our understanding of galaxy formation, and even the cosmological models.

Overall, in this thesis, we measured the luminosity and spatial distributions of galactic satellites around isolated primaries from the SDSS. We also compare the model predictions with those measurements from the SDSS. The results show such comparisons can be a non-trivial validation of the assumptions and framework of this kind of modelling. However, for the GALFORM model, the colour dependence is one area where there exists room for improvement.

BIBLIOGRAPHY

Abazajian K. N. et al., 2009, ApJS, 182, 543

Agustsson I., Brainerd T. G., 2010, ApJ, 709, 1321

Ágústsson I., Brainerd T. G., 2011, ISRN Astronomy and Astrophysics, 2011

Aihara H. et al., 2011, ApJS, 193, 29

Albrecht A., Steinhardt P. J., 1982, Physical Review Letters, 48, 1220

Azzaro M., Patiri S. G., Prada F., Zentner A. R., 2007, MNRAS, 376, L43

Baldry I. K., Glazebrook K., Brinkmann J., Ivezić Ž., Lupton R. H., Nichol R. C., Szalay A. S., 2004, ApJ, 600, 681

Bartelmann M., 1996, A&A, 313, 697

Baugh C. M., 2006, Reports on Progress in Physics, 69, 3101

Baugh C. M., Lacey C. G., Frenk C. S., Granato G. L., Silva L., Bressan A., Benson A. J., Cole S., 2005, MNRAS, 356, 1191

Belokurov V. et al., 2008, ApJ, 686, L83

Belokurov V. et al., 2010, ApJ, 712, L103

Benson A. J., Frenk C. S., Lacey C. G., Baugh C. M., Cole S., 2002, MNRAS, 333, 177

Blanton M. R., Lupton R. H., Schlegel D. J., Strauss M. A., Brinkmann J., Fukugita M., Loveday J., 2005, ApJ, 631, 208

Blanton M. R., Roweis S., 2007, AJ, 133, 734

Blanton M. R. et al., 2005, AJ, 129, 2562

Bode P., Ostriker J. P., Turok N., 2001, ApJ, 556, 93

Botzler C. S., Snigula J., Bender R., Hopp U., 2004, MNRAS, 349, 425

Bower R. G., Benson A. J., Malbon R., Helly J. C., Frenk C. S., Baugh C. M., Cole S., Lacey C. G., 2006, MNRAS, 370, 645

Boylan-Kolchin M., Springel V., White S. D. M., Jenkins A., 2010, MNRAS, 406, 896

Boylan-Kolchin M., Springel V., White S. D. M., Jenkins A., Lemson G., 2009, MNRAS, 398, 1150

Brainerd T. G., 2005, ApJ, 628, L101

Bullock J. S., Kravtsov A. V., Weinberg D. H., 2000, ApJ, 539, 517

Busha M. T., Alvarez M. A., Wechsler R. H., Abel T., Strigari L. E., 2010a, ApJ, 710, 408

Busha M. T., Alvarez M. A., Wechsler R. H., Abel T., Strigari L. E., 2010b, ApJ, 710, 408

Busha M. T., Wechsler R. H., Behroozi P. S., Gerke B. F., Klypin A. A., Primack J. R., 2011, ApJ, 743, 117

Chen J., Kravtsov A. V., Prada F., Sheldon E. S., Klypin A. A., Blanton M. R., Brinkmann J., Thakar A. R., 2006, ApJ, 647, 86

Cole S., Aragon-Salamanca A., Frenk C. S., Navarro J. F., Zepf S. E., 1994, MNRAS, 271, 781

Cole S., Lacey C. G., Baugh C. M., Frenk C. S., 2000, MNRAS, 319, 168

Coles P., Lucchin F., 2002, Cosmology: The Origin and Evolution of Cosmic Structure, Second Edition

Colless M. et al., 2001, MNRAS, 328, 1039

Collins M. L. M. et al., 2010, MNRAS, 407, 2411

Conroy C. et al., 2005, ApJ, 635, 982

Cooper A. P. et al., 2010a, MNRAS, 406, 744

Cooper A. P. et al., 2010b, MNRAS, 406, 744

Couchman H. M. P., Thomas P. A., Pearce F. R., 1995, ApJ, 452, 797

Craig M. W., Davis M., 2001, New A, 6, 425

Croton D. J. et al., 2006, MNRAS, 365, 11

Csabai I. et al., 2003, AJ, 125, 580

Davis M. et al., 2003, in Guhathakurta P., ed., Society of Photo-Optical Instrumentation Engineers (SPIE) Conference Series Vol. 4834, Society of Photo-Optical Instrumentation Engineers (SPIE) Conference Series. pp 161–172

Diemand J., Kuhlen M., Madau P., 2007, ApJ, 657, 262

Diemand J., Moore B., Stadel J., 2004, MNRAS, 352, 535

Dodelson S., Efstathiou G., 2004, Physics Today, 57, 60

Driver S. P. et al., 2011, MNRAS, 413, 971

Driver S. P., Liske J., Cross N. J. G., De Propris R., Allen P. D., 2005, MNRAS, 360, 81

Driver S. P. et al., 2009, Astronomy and Geophysics, 50, 050000

Flynn C., Holmberg J., Portinari L., Fuchs B., Jahreiß H., 2006, MNRAS, 372, 1149

Font A. S. et al., 2011a, MNRAS, 417, 1260

Font A. S. et al., 2011b, MNRAS, 417, 1260

Font A. S. et al., 2008, MNRAS, 389, 1619

Freidmann A., 1922, Zeitschrift fr Physik A Hadrons and Nuclie, 10, 337

Gil de Paz A. et al., 2007, ApJS, 173, 185

González J. E., Lacey C. G., Baugh C. M., Frenk C. S., Benson A. J., 2009, MNRAS, 397, 1254

Granato G. L., De Zotti G., Silva L., Bressan A., Danese L., 2004, ApJ, 600, 580

Grebel E. K., 2000, in Favata F., Kaas A., Wilson A., eds, ESA Special Publication Vol. 445, Star Formation from the Small to the Large Scale. p. 87

Gunn J. E., Gott J. R. I., 1972, ApJ, 176, 1

Guo Q., Cole S., Eke V., Frenk C., 2011, MNRAS, 417, 370

Guo Q., Cole S., Eke V., Frenk C., 2012, ArXiv e-prints

Guo Q., Cole S., Eke V., Frenk C., 2013, MNRAS, 417, 370

Guo Q. et al., 2011, MNRAS, 413, 101

Guo Q., White S., Li C., Boylan-Kolchin M., 2010, MNRAS, 404, 1111

Guth A. H., 1981, Phys. Rev. D, 23, 347

Hartwick F. D. A., 2000, AJ, 119, 2248

Hinshaw G. et al., 2012, ArXiv e-prints

Holmberg E., 1969, Arkiv for Astronomi, 5, 305

Hwang H. S., Park C., 2010, ApJ, 720, 522

Irwin M. J. et al., 2007, ApJ, 656, L13

Jiang C., Jing Y., Li C., 2012, ArXiv e-prints

Kauffmann G., Colberg J. M., Diaferio A., White S. D. M., 1999, MNRAS, 303, 188

Kauffmann G., White S. D. M., Guiderdoni B., 1993, MNRAS, 264, 201

Kim E., Kim M., Hwang N., Lee M. G., Chun M.-Y., Ann H. B., 2011, MNRAS, 412, 1881

Klypin A., Kravtsov A. V., Valenzuela O., Prada F., 1999, ApJ, 522, 82

Klypin A., Prada F., 2009, ApJ, 690, 1488

Koposov S. et al., 2008, ApJ, 686, 279

Koposov S. E., Yoo J., Rix H.-W., Weinberg D. H., Macciò A. V., Escudé J. M., 2009a, ApJ, 696, 2179

Koposov S. E., Yoo J., Rix H.-W., Weinberg D. H., Macciò A. V., Escudé J. M., 2009b, ApJ, 696, 2179

Lacey C., Guiderdoni B., Rocca-Volmerange B., Silk J., 1993, ApJ, 402, 15

Lagos C. D. P., Baugh C. M., Lacey C. G., Benson A. J., Kim H.-S., Power C., 2011, MNRAS, 418, 1649

Lake G., Tremaine S., 1980, ApJ, 238, L13

Lares M., Lambas D. G., Domínguez M. J., 2011, AJ, 142, 13

Larson R. B., 1974, MNRAS, 169, 229

Li C., Jing Y. P., Kauffmann G., Börner G., Kang X., Wang L., 2007, MNRAS, 376, 984

Li Y.-S., De Lucia G., Helmi A., 2010, MNRAS, 401, 2036

Libeskind N. I., Cole S., Frenk C. S., Okamoto T., Jenkins A., 2007a, MNRAS, 374, 16

Libeskind N. I., Cole S., Frenk C. S., Okamoto T., Jenkins A., 2007b, MNRAS, 374, 16

Libeskind N. I., Frenk C. S., Cole S., Helly J. C., Jenkins A., Navarro J. F., Power C., 2005, MNRAS, 363, 146

Linde A., 2005, ArXiv High Energy Physics - Theory e-prints

Linde A. D., 1982, Physics Letters B, 108, 389

Liu C., Hu J., Newberg H., Zhao Y., 2008, A&A, 477, 139

Liu L., Gerke B. F., Wechsler R. H., Behroozi P. S., Busha M. T., 2011, ApJ, 733, 62

Lorrimer S. J., Frenk C. S., Smith R. M., White S. D. M., Zaritsky D., 1994, MNRAS, 269, 696

Loveday J. et al., 2012, MNRAS, 420, 1239

Lovell M. R. et al., 2012, MNRAS, 420, 2318

Ludlow A. D., Navarro J. F., Springel V., Jenkins A., Frenk C. S., Helmi A., 2009, ApJ, 692, 931

Macciò A. V., Kang X., Fontanot F., Somerville R. S., Koposov S., Monaco P., 2010, MNRAS, 402, 1995

Mandelbaum R. et al., 2005, MNRAS, 361, 1287

Martin N. F., de Jong J. T. A., Rix H.-W., 2008, ApJ, 684, 1075

Martin N. F., Ibata R. A., Irwin M. J., Chapman S., Lewis G. F., Ferguson A. M. N., Tanvir N., McConnachie A. W., 2006, MNRAS, 371, 1983

Mateo M. L., 1998, ARA&A, 36, 435

Mather J. C., Fixsen D. J., Shafer R. A., Mosier C., Wilkinson D. T., 1999, ApJ, 512, 511

McConnachie A. W., Irwin M. J., 2006, MNRAS, 365, 1263

Merson A. I. et al., 2012, ArXiv e-prints

Monaco P., Fontanot F., 2005, MNRAS, 359, 283

Monaghan J. J., 1992, ARA&A, 30, 543

Moore B., Gelato S., Jenkins A., Pearce F. R., Quilis V., 2000, ApJ, 535, L21

Moore B., Ghigna S., Governato F., Lake G., Quinn T., Stadel J., Tozzi P., 1999, ApJ, 524, L19

More S., van den Bosch F. C., Cacciato M., Mo H. J., Yang X., Li R., 2009, MNRAS, 392, 801

Muñoz J. A., Madau P., Loeb A., Diemand J., 2009a, MNRAS, 400, 1593

Muñoz J. A., Madau P., Loeb A., Diemand J., 2009b, MNRAS, 400, 1593

Navarro J. F., Frenk C. S., White S. D. M., 1996, ApJ, 462, 563

Navarro J. F., Frenk C. S., White S. D. M., 1997, ApJ, 490, 493

Nierenberg A. M., Auger M. W., Treu T., Marshall P. J., Fassnacht C. D., 2011, ApJ, 731, 44

Norberg P., Gaztañaga E., Baugh C. M., Croton D. J., 2011, MNRAS, 418, 2435

Nussbaumer H., Bieri L., 2011, The Observatory, 131, 394

Okamoto T., Frenk C. S., 2009a, MNRAS, 399, L174

Okamoto T., Frenk C. S., 2009b, MNRAS, 399, L174

Okamoto T., Frenk C. S., Jenkins A., Theuns T., 2010, MNRAS, 406, 208

Page L. et al., 2003, ApJS, 148, 233

Parry O. H., Eke V. R., Frenk C. S., Okamoto T., 2012, MNRAS, 419, 3304

Peacock J. A., 1999, Cosmological Physics

Peebles P. J. E., 1993, Principles of Physical Cosmology

Perlmutter S. et al., 1999, ApJ, 517, 565

Prada F. et al., 2003, ApJ, 598, 260

Prescott M. et al., 2011, MNRAS, 417, 1374

Riess A. G. et al., 1998, AJ, 116, 1009

Ryden B. S., 2004, ApJ, 601, 214

Sales L., Lambas D. G., 2004, MNRAS, 348, 1236

Sales L., Lambas D. G., 2005, MNRAS, 356, 1045

Sales L. V., Wang W., White S. D. M., Navarro J. F., 2012, MNRAS, p. 31

Schechter P., 1976, ApJ, 203, 297

Shimasaku K. et al., 2001, AJ, 122, 1238

Simon J. D., Geha M., 2007, ApJ, 670, 313

Siverd R. J., Ryden B. S., Gaudi B. S., 2009, ArXiv e-prints

Skibba R. A., Sheth R. K., 2009, MNRAS, 392, 1080

Smith J. A. et al., 2002, AJ, 123, 2121

Smith R. M., Martínez V. J., Graham M. J., 2004, ApJ, 617, 1017

Somerville R. S., 2002, ApJ, 572, L23

Somerville R. S., Primack J. R., 1999, MNRAS, 310, 1087

Spergel D. N., Steinhardt P. J., 2000, Physical Review Letters, 84, 3760

Spergel D. N. et al., 2003, ApJS, 148, 175

Springel V. et al., 2008a, MNRAS, 391, 1685

Springel V. et al., 2008b, MNRAS, 391, 1685

Springel V. et al., 2005, Nature, 435, 629

Strateva I. et al., 2001, AJ, 122, 1861

Strauss M. A. et al., 2002, AJ, 124, 1810

Strigari L. E., Wechsler R. H., 2012, ApJ, 749, 75

Tal T., van Dokkum P. G., 2011, ApJ, 731, 89

Tal T., Wake D. A., van Dokkum P. G., 2012, ApJ, 751, L5

Tollerud E. J., Boylan-Kolchin M., Barton E. J., Bullock J. S., Trinh C. Q., 2011, ApJ, 738, 102

Tollerud E. J., Bullock J. S., Strigari L. E., Willman B., 2008, ApJ, 688, 277

Vader J. P., Sandage A., 1991, ApJ, 379, L1

van den Bergh S., 2000, The Galaxies of the Local Group. Cambridge

van den Bosch F. C., Norberg P., Mo H. J., Yang X., 2004, MNRAS, 352, 1302

van den Bosch F. C., Yang X., Mo H. J., Norberg P., 2005, MNRAS, 356, 1233

Wadepuhl M., Springel V., 2011, MNRAS, 410, 1975

Wang J., Frenk C. S., Cooper A. P., 2012, ArXiv e-prints

Wang W., Jing Y. P., Li C., Okumura T., Han J., 2011, ApJ, 734, 88

Wang W., White S. D. M., 2012, MNRAS, 424, 2574

Watkins L. L. et al., 2009, MNRAS, 398, 1757

Watson D. F., Berlind A. A., McBride C. K., Hogg D. W., Jiang T., 2012, ApJ, 749, 83

Weinmann S. M., Pasquali A., Oppenheimer B. D., Finlator K., Mendel J. T., Crain R. A., Macciò A. V., 2012, MNRAS, 426, 2797

White S. D. M., Frenk C. S., 1991, ApJ, 379, 52

White S. D. M., Rees M. J., 1978, MNRAS, 183, 341

Yang X., Mo H. J., van den Bosch F. C., Pasquali A., Li C., Barden M., 2007, ApJ, 671, 153

Yang X., van den Bosch F. C., Mo H. J., Mao S., Kang X., Weinmann S. M., Guo Y., Jing Y. P., 2006, MNRAS, 369, 1293

York D. G. et al., 2000, AJ, 120, 1579

Yoshida N., Springel V., White S. D. M., Tormen G., 2000, ApJ, 544, L87

Zaritsky D., Smith R., Frenk C., White S. D. M., 1993, ApJ, 405, 464

Zaritsky D., Smith R., Frenk C., White S. D. M., 1997a, ApJ, 478, 39

Zaritsky D., Smith R., Frenk C. S., White S. D. M., 1997b, ApJ, 478, L53

Zehavi I. et al., 2005, ApJ, 630, 1

Zucker D. B. et al., 2006, ApJ, 643, L103

Zucker D. B. et al., 2004, ApJ, 612, L121

Zucker D. B. et al., 2007, ApJ, 659, L21